Repository Istituzionale dei Prodotti della Ricerca del Politecnico di Bari

Improvement of diesel engines efficiency driving the fuel pump with an electrical machine

(Article begins on next page)

19 April 2024

Department of Electrical and Information Engineering

ELECTRICAL AND INFORMATION ENGINEERING

Ph.D.Program

SSD: ING-IND/32 – CONVERTERS, ELECTRICAL MACHINES AND DRIVES

Final Dissertation
2018

Improvement of diesel engines efficiency driving the fuel pump with an electrical machine

---

by

Ing. Pasquale Caldori

Supervisors:

Prof. Francesco Cupertino

Ing. Antonio Arvizzigno

Coordinator of Ph.D Program:

Prof. Vittorio Passaro

Course n°30, 01/11/2014-31/10/2017

Department of Electrical and Information Engineering

ELECTRICAL AND INFORMATION ENGINEERING Ph.D.Program

SSD: ING-IND/32 – CONVERTERS, ELECTRICAL MACHINES AND DRIVES

Final Dissertation

2018

Improvement of diesel engines efficiency driving the fuel pump with an electrical machine

by

Ing. Pasquale Caldori

Referees:

Prof. Giacomo Scelba

Prof. Renato Rizzo

Supervisors:

Prof. Francesco Cupertino

Ing. Antonio Arvizzigno

Coordinator of Ph.D Program:

Prof. Vittorio Passaro

Course n°30, 01/11/2014-31/10/2017

SUMMARY

ACKNOWLEDGMENTS

INTRODUCTION

This work was developed in collaboration with CVIT-Bosch (Centro Studi Componenti per Veicoli), located in Modugno (BA). In particular, the Bosch headquarter in Bari is a center, where high pressure pumps for diesel injection systems are developed.

A common rail fuel injection system can be divided into two major parts:

➢ Low pressure side components: these components serve to safely and reliably deliver fuel from the tank to the fuel injection system. Low pressure side components include the fuel tank, the fuel supply pump and the fuel filter;

➢ High pressure side components: components that create high pressures, meter and deliver the fuel to the combustion chamber. They include the high pressure pump, the fuel injector and the fuel injection nozzles.

In this work, the low pressure pump is a gerotor (that is, a volumetric pump), where the pressure is increased due to the effect of the volume variation realised by a rotating part; in particular, the rotating part is composed of teeth, which create a vacuum and a compression, alternatively. When the vacuum occurs, a suction phase takes place; so, the fuel enters the low pressure pump; then, thanks to the compression phase, the fuel is sent to the high pressure pump. Currently, in truck applications, the pre-feed pump is mechanically coupled to the high-pressure pump and the high-pressure pump is driven by the Diesel engine via a gear drive. The speed of the pre-feed pump is therefore proportional to the engine speed and can't be set independently on it. As a consequence, the pre-feed delivery (that gets higher over the speed) can't be adjusted to the actual flow demand of the fuel injection equipment. There are operative conditions where no or negligible injection quantity is required because there is no torque demand to the engine (for example during a downhill driving with the engine pulled by the vehicle...). Under those conditions the pre-feed pump delivers quantity that get wasted (re-circulated) with a detrimental loss of energy. To overcome this disadvantage, it was thought to couple the volumetric pump to an electric motor. In this way, the volumetric pump can be controlled in real time so to be adapted to the actual flowrate needed by the engine, with clear benefits on the overall efficiency.

When this work started, the prototype of the electric machine, to be coupled to the volumetric pump and described in the following chapters, had already been designed and manufactured by Bosch. Then this work was focused on the analysis of the existing prototype, on the evaluation of potential alternatives (different electrical machines) aimed at the reduction of the permanent magnet (PM)

quantity and also on the development of dedicated control schemes to improve dynamic performances.

The thesis is divided into four chapters. In the first chapter, it is described the electrical motor design activities. In particular the motor's layouts taken into account are different from the one chosen for the Bosch prototype. This activity has led to the development of analytical design tools, which made it possible to make a quick comparison between the layout of the Bosch's prototype and alternative motor typologies. In addition, thanks to the methodology developed in the first chapter, it has been easy to carry out the verification of the layout of the electric machine designed by Bosch. This analysis has been carried out in order to get a better understanding of the possible improvements that could be reached with some design modifications. In particular, the permanent magnet quantity is the main issue to the material cost.

In parallel to the motor design, the experimental characterization of the Bosch prototype has been carried out, whose procedures and results are described and reported in the second chapter. A dedicated test bench, capable of automatically execute some experiments has been developed. The test bench was used to characterize electrical machines (following international standards); that is an important task when a new product is introduced into the market. Moreover, thanks to the test bench, alternative control algorithms have been developed. That is, alternative control solutions to the algorithms developed by Bosch (the algorithms developed by Bosch are not shown here for confidentiality restrictions). The control algorithms have been also tested on the volumetric pump, in order to verify the starting capability of the developed sensorless control, when the pump faces difficult situations (for example, a residual pressure at the starting).

Finally, the last chapter describes the implementation of the control algorithms on an industrial DSP programmed in C language.

CHAPTER I

1. Brief introduction to electrical motors

AC electric motors can be divided into two major typologies:

➢ Asynchronous motors;

➢ Synchronous motors.

In particular, the permanent magnet synchronous electric motors are the most used in automotive applications. Indeed, in applications where high power density is required, permanent magnet electric motors represent the most suitable solution; on the other hand, the cost of these machines is quite high due to the presence of permanent magnets. For this reason, a valid alternative is in using the reluctance electric motors, which are able to use the magnetic anisotropy for the torque generation.

Reluctance motors, in turn, can be subdivided into:

➢ ALA (axial laminated anisotropic) rotor;

➢ TLA (transverse laminated anisotropic) rotor.

The TLA motors are the most widely used, since they have a lower cost compared to axial laminated reluctance motors. In TLA motors, the magnetic saliency is created through flux barriers, which are in the rotor's physical structure (that is, the rotor consists of alternating layers of iron and air).

In particular, in TLA motors type, increasing the anisotropy, the power factor increases; therefore, also the efficiency increases (due to the increase of the torque); nevertheless, the negative contribution due to the presence of axial and radial ribs must be taken into account; these can affect the torque, leading to machines with low power factor. To solve the problem of low power factor, one could think of adding permanent magnets (also said PMs) to the rotor structure. Using PMs, it is possible to improve the power factor also obtaining more efficient machines. These new machines types are called PM-assisted synchronous reluctance machines (PM-Assisted SyRM).

This chapter is focused on the design criteria of electric motors such as:

➢ Surface permanent magnet motors;

➢ Reluctance motors;

➢ PM-Assisted reluctance motors.

1.1. SPM design
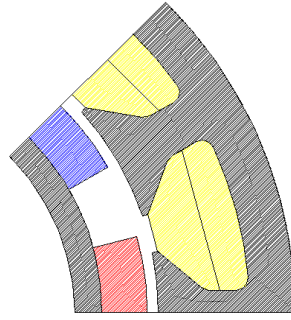
fig. 1: SPM Motor

fig. 1 shows the configuration of a surface permanent magnet synchronous motor (SPM).

The electromagnetic model of a surface permanent magnet motor in dq coordinates is:

$$v_{sd} = R_s i_{sd} + L_d \frac{di_{sd}}{dt} - \omega_r L_q i_{sq} \qquad \text{eq. 1}$$

$$v_{sq} = R_s i_{sq} + L_q \frac{di_{sq}}{dt} + \omega_r L_d i_{sd} + \omega_r \psi_{PM} \qquad \text{eq. 2}$$

$$T_{em} = \frac{3}{2}\frac{P}{2}\left\{(L_d - L_q)i_{sd}i_{sq} + \psi_{PM}i_{sq}\right\} \qquad \text{eq. 3}$$

Where L_d is the inductance along the d-axis, L_q is the inductance along the q-axis and Ψ_{PM} is the flux generated by the permanent magnets; P is the number of poles. Since the flux path is the same along the two magnetic axes, the d-axis inductance is equal to the q-axis inductance (this is true in most cases, in which the iron saturation along the d-axis is negligible). From the equality of inductances, the expression of the torque can be simplified as eq. 4 states:

$$T_{em} = \frac{3}{2}\frac{P}{2}\psi_{PM}i_{sq} = K_T i_{sq} \qquad \text{eq. 4}$$

For designing an SPM motor type, it is needed to define the elementary block, shown in fig. 2 [1]:

fig. 2: Elementary block of a linearized SPM (only one pole-pitch shown)

The parameters in fig. 2 are specified in Table 1:

Table 1: PARAMETERS OF THE ELEMENTARY BLOCK SHOWN IN fig. 2

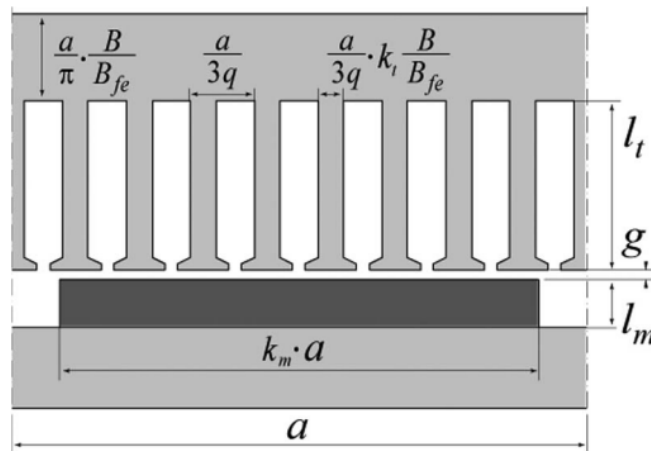| Parameter	Meaning
a	Pole pitch
l_t	Tooth height
l_m	Magnet height
g	Airgap thickness
q	Number of slots per pole-phase
k_t	Scaling factor for the stator tooth
k_m	Scaling factor for the magnet
B_{fe}	Iron saturation level
B	Airgap flux density
N_c	Number of conductors per pole-phase

To begin the design of a SPM motor, the fundamental geometric parameters to be defined are:

➢ Airgap thickness (g);

➢ Airgap radius (r);

➢ Magnetic span, defined in percent of the pole-pitch (k_m).

For k_m an optimum value is in the range 0.7÷0.8.

The other parameters to be defined are:

➢ Winding type (q, slot fill factor, winding factor..);

➢ Remanence of the permanent magnet (B_r);

➢ Iron saturation level (B_{fe});

➢ Total machine volume ($\pi R^2 l$);

➢ Number of pole pairs.

The number of pole pairs depend on the ratio between mechanical frequency and electric frequency. Mechanical frequency is limited by resonance phenomena and mechanical vibrations that can be triggered in the drive; on the other hand, the electric frequency is limited by the frequency of the PWM signals.

Finally, it is needed to define the torque and the efficiency, to be fulfilled by the machine:

➢ Target torque (T) and efficiency (η).

From the target torque and efficiency, it is possible to calculate the total losses of the motor (eq. 5):

$$Total\ losses = T\omega_m \left(\frac{1}{\eta} - 1\right)$$

eq. 5

After the basic geometric parameters and expected performance are defined, the machine design will be performed according to the following steps:

1.   Calculation of outer stator radius:

Knowing the torque and efficiency, the allowable losses can be calculated. In this phase of the design, only Joule losses will be considered (iron losses can be neglected in the preliminary design phase). For the design of the machines, it is necessary to know the cooling type; so, it is possible to use the thermal dissipation values reported in Table 2 (the values are referred to external surface units) [2]:

Table 2: STANDARD VALUES FOR kj

Type of cooling	Value
Natural ventilation	3500 W/m^2
Forced ventilation	10000 W/m^2

From the relation, that exists between k_j and the volume of the machine, the outer radius of stator can be obtained by using eq. 6:

$$k_j = \frac{Total\ losses}{Machine\ volume}\frac{R}{2}$$

eq. 6

Then, the axial length can be calculated (eq. 7):

$$Machine\ volume = \pi R^2 l$$

eq. 7

2.   Calculation of airgap flux density:

Since the remanence of the permanent magnet is known, it is possible to calculate the airgap flux density (eq. 8). In eq. 8, k_c is the Carter factor, while k_b is the form factor used to calculate the magnitude of the fundamental harmonic. The ratio between the airgap thickness and the magnet thickness (g/l_m) depends on the coercive field of the magnet [1]. A good approximation is in using a ratio equal to 5 or higher [3].

$$B = k_b \cdot \frac{B_r}{1 + k_c \cdot \frac{g}{l_m}}$$

eq. 8

$$k_b = \frac{4}{\pi} \cdot \sin\left(k_m \frac{\pi}{2}\right)$$

eq. 9

3.   Calculation of stator geometry:

The stator geometry is obtained by using the eq. 10 and eq. 11 [1]:

➤   Stator tooth width:

$$w_t = \frac{a}{3q} \cdot k_t \cdot \frac{B}{B_{fe}}$$

eq. 10

➢ Back-iron thickness:

$$l_y = \frac{a}{\pi} \cdot \frac{B}{B_{fe}}$$

eq. 11

From the outer stator radius (R), it is possible to calculate the height of the stator tooth, using the eq. 12:

$$R = r + g + l_t + l_y$$

eq. 12

4. Calculation of maximum current i_{sq}:

From the admitted Joule losses and the stator tooth height, it is possible to calculate the current i_{sq} [1]:

$$i_{sq} = \frac{\pi}{3N} R^{1.5} \sqrt{k_{cu} \frac{k_j}{\rho} \frac{l}{l'}} \sqrt{\frac{A_s}{\pi R^2}}$$

eq. 13

The parameters in eq. 13 are introduced in Table 3:

Table 3: PARAMETERS USED IN eq. 13

Parameter	Meaning
A_s	Slot area
k_{cu}	Slot fill factor
l'	Total axial length, given by the sum of axial length of the machine and end-windings connections
ρ	Copper resistivity referred to the operating temperature

In literature there exist different methods to calculate the end-winding length; in this work, it is preferred to use very simple relations [4], such as Table 4 shows:

Table 4: FORMULA FOR END-WINDING CALCULATION

Winding type	End-winding formula
Non overlapped windings	$l_{end} = 1.2 \frac{2\pi(r+g)}{Q}$
Overlapped windings	$l_{end} = 2.5 \frac{2(r+g)}{p}$

In Table 4, Q is the number of slots.

From the electric loading, it is possible to calculate the torque using eq. 14 [1]:

$$T = BA \cdot 2\pi \cdot r^2 \cdot l = \sigma \cdot 2\pi \cdot r^2 \cdot l \qquad \text{eq. 14}$$

Where σ is the shear stress, given by the product between the electric loading and the magnetic loading.

If the torque value is lower than the target value, it is possible to fix the problem using the following options:

a.   Increase the remanence of the permanent magnets;

b.   Increase the admitted Joule losses.

If the remanence of the permanent magnets is increased, then the machine cost will be higher; therefore, the efficiency and the power factor will be higher too; on the other hand, if one decides to increase the admitted Joule losses, the machine cost will be lower, but the efficiency will be also lower. To finalize the design of the SPM machine, it is needed to calculate the inductance and the power factor.

The inductance value is given in p.u. (eq. 15) [1]:

$$L_{pole,pu} = L_{g,pu} + L_{slot,pu} \qquad \text{eq. 15}$$

The L_d will be given by multiplying $L_{pole,pu}$ and the base inductance value. The base inductance value is given in eq. 16:

$$L_{base} = \frac{\mu_0 \cdot l}{2} \cdot \left(\frac{2}{\pi} \cdot k_w \cdot N_c \right)^2 \qquad \text{eq. 16}$$

$L_{g,pu}$ and $L_{slot,pu}$ expressions can change according to the type of winding. These expressions have been summarized up in Table 5:

Table 5: SPM FORMULAS FOR INDUCTANCE CALCULATION

Winding type	L_d p.u. formula
Distributed Winding Machines	$L_{g,pu} = \dfrac{\pi^2}{6 \cdot k_w^2} \cdot \left(\dfrac{1}{k_c + \frac{l_m}{g}} \right) \cdot \dfrac{a}{g}$ $L_{slot,pu} = \dfrac{\pi^2}{2 \cdot k_w^2} \cdot \dfrac{\frac{l_t}{g}}{(1 - k_t \cdot \frac{B}{B_{fe}})} \cdot \left(\dfrac{a}{g} \right)^{-1}$
Fractional Slot Machines	$L_{g,pu} = \dfrac{1}{n_l} \cdot \dfrac{\pi^2}{12(qk_w)} \cdot \left(\dfrac{1}{k_c + \frac{l_m}{g}} \right) \cdot \dfrac{a}{g}$ $L_{slot,pu} = \dfrac{\pi^2}{2 \cdot k_w^2} \cdot \dfrac{\frac{l_t}{g}}{(1 - k_t \cdot \frac{B}{B_{fe}})} \cdot (1 - \dfrac{3 \cdot (n_l - 1)}{4 \cdot Q_0}) \cdot \left(\dfrac{a}{g} \right)^{-1}$

In the formulas shown in Table 5, the symbol n_l represents the number of layers of the fractional slot winding; Q_0 is the number of slots, which are in the machine periodicity. The periodicity of the machine is given by eq. 17 [1]:

$$t = \gcd(Q, P) \qquad\qquad \text{eq. 17}$$

In the end, in order to complete the design of the machine, it is necessary to calculate the power factor [1]:

$$PF = \cos(\varphi) = \cos\left(\text{atan}\left(\frac{4\mu_0}{3\pi} \cdot L_{pole,pu} \cdot \frac{A}{B}\right)\right) \qquad\qquad \text{eq. 18}$$

1.2. Non linear effects in SPM

An iterative cycle has been created in order to take into account the saturation of the iron stator; the iterative cycle increases apparently the air thickness of the airgap, so to have a corrected equivalent reluctance value. When the iron saturation increases, the cycle increases the airgap thickness accordingly. At the beginning, the iterative process calculates the ratio between the amount of iron and the amount of air, which are at the half stator radius (that is, the radius, which passes through half the height of the stator tooth). This ratio has been indicated by parameter b.

$$b = \frac{w_t \cdot Number\ of\ slots}{(Slot\ pitch - w_t) \cdot Number of\ slots} \qquad\qquad \text{eq. 19}$$

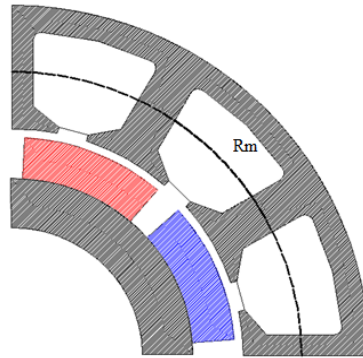To complete the iron saturation analysis, the flux path, shown in fig. 4, has been supposed.

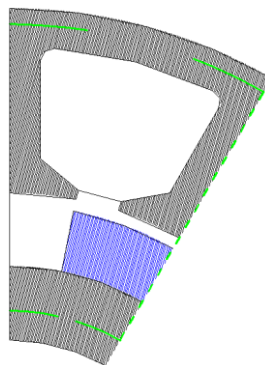fig. 3: Radius considered for the calculation of b parameter

fig. 4: Supposed flux path for the analysis of the stator iron saturation

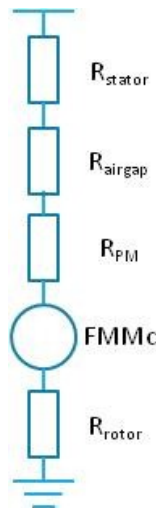From the flux path supposed, the following magnetic circuit can be drawn:

fig. 5: Magnetic circuit used for the analysis of the stator iron saturation

Where the symbols have the following meanings:

1. R_{stator}: Sum of the reluctance of the stator tooth and the back-iron;

2. R_{airgap}: Airgap reluctance;

3. R_{PM}: Permanent magnet reluctance;

4. FMM_c: Magneto-motive force due to coercive field of the magnet;

5. R_{rotor}: Rotor reluctance.

To make easier the calculations, it has been supposed that the magnetic voltage drop in the rotor iron is negligible (R_{rotor}=0).

Since the airgap flux density B depends on the value of the airgap, g, the first step consists of calculating the magnetic voltage drop at the airgap:

$$F_g = \frac{B(g)}{\mu_0} \cdot k_c \cdot g \qquad \text{eq. 20}$$

From the value of b, it is possible to calculate the flux density in the iron; then, the magnetic voltage drop in the stator iron:

$$B_{fe} = \frac{B(g)}{b} \qquad \text{eq. 21}$$

$$F_{fe} = H_{fe}(B_{fe}) \cdot L_{fe} \qquad \text{eq. 22}$$

Finally, the r value is calculated, using the eq. 23:

$$r = \frac{F_g + F_{fe}}{F_g} \qquad \text{eq. 23}$$

Until the ratio is higher than 1.2, the iterative cycle will be continuing to increase the airgap thickness. When F_{fe} is negligible in comparison with F_g, the iterative cycle stops.

To complete the paragraph, a mention about iron losses is necessary. The iron losses are calculated by means of the Steinmetz equation (eq. 24):

$$P_{fe} = p_{hy} + p_{ec} = k_i f B_{fe}^h + k_c f^2 B_{fe}^2 \qquad \text{eq. 24}$$

Where p_{hy} are the hysteresis losses and p_{ec} are the eddy-current losses; in eq. 24, it is necessary to calculate the iron flux density (by means of the ratio B/b) and set-up the electrical frequency value.

Thanks to the estimation of iron losses and the estimation of torque reduction, the analytic tool is able to estimate the efficiency by means of the relations presented before.

1.3. PM-Assisted SyRM

A very short introduction about permanent magnets is given, before introducing the fundamental relations for the design of the PM assisted reluctance machines.

Generally speaking, a permanent magnet can be represented as a flux generator with in parallel the reluctance of the magnet itself [3].
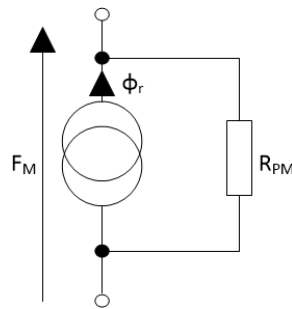

fig. 6: Equivalent magnetic circuit of PM (Norton equivalent representation)

Permanent magnets can be classified on the basis of remanence in "strong" and "weak" magnets (classification shown in fig. 7). The PM are weak permanent magnets, because of their low remanence. When the machine is designed, it is needed to evaluate the dangerous effects, which come from [2]:

➢ Temperature;

➢ Current magnitude.

Indeed, the higher the temperature, the lower remanence becomes. In normal operation, the current is in opposition to the field generated by the permanent magnets (flux weakining operation); because of that, it is likely to demagnetize the magnet itself [5] [2].
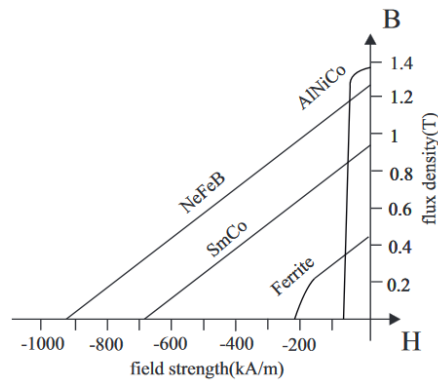
fig. 7: Permanent magnet classification

Although the problem pointed out before, in this work no attention will be paid toward demagnetization of PMs. At the end of the design phase and before prototype manufacturing, detailed calculations to assess the risk of demagnetization are needed.

1.4. Some clarifications about PM-Assisted SyRM
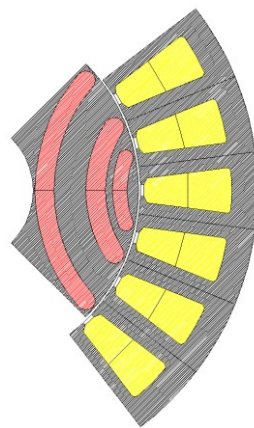
fig. 8: PM-Assisted SyRM with 3 rotor barriers

The design of the reluctance motors starts from the analysis of an Open Source software, called **Syre.** Such software has been developed in MatLab environment and it gives different tools to build the reluctance machine geometries. In particular, Syre uses an interface between MatLab and FEMM in order to design and optimize reluctance machines.

From **Syre**, it is possible to choose different rotor typologies, on the basis of rotor barrier shapes; for example:

➢   Circular;

➢   Segmented;

➢   Fluid.

To be coherent with the current scientific literature, the circular barrier type have been chosen.

fig. 9: GUI Syre

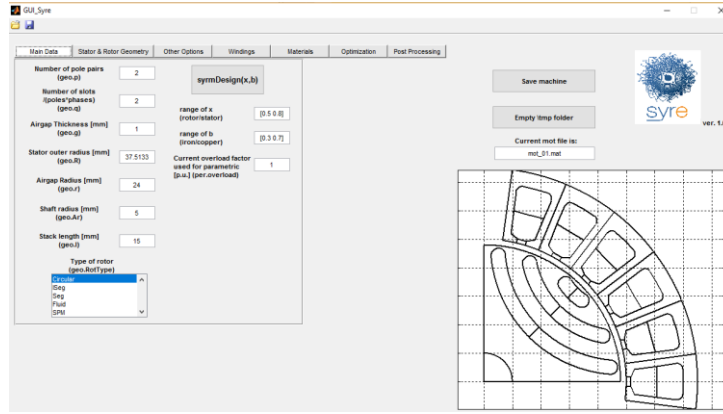A mention about the different convention used for the design of reluctance machines is necessary. In particular, in the earlier paragraph, the classical dq axes orientation has been used. In this case, for the design of reluctance machines, it is necessary to use the DQ-axes orientation. In particular, the Q-axis is aligned with the magnets, and it points against the magnet itself. Between the phasors of dq and DQ systems, there is a displacement of 90° electrical degrees, as one can see from fig. 10 [5]:
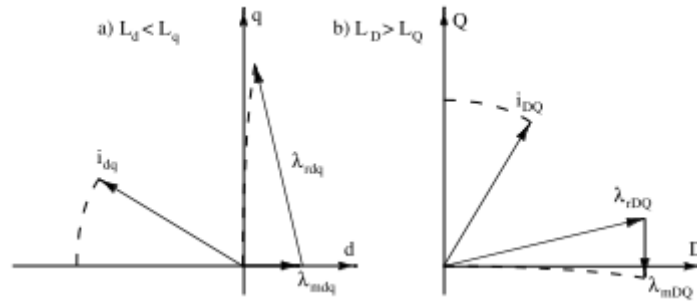
fig. 10: Comparison between dq and DQ system

In other words, in order to understand better the changes, in the new reference system, the inductance L_D matches the L_q inductance value; the same consideration is pursued for L_Q and L_d.

The electromagnetic model in the DQ reference system is:

$$v_{sD} = R_s i_{sD} + L_D \frac{di_{sD}}{dt} - \omega_r L_Q i_{sQ} + \omega_r \psi_{PM} \qquad \text{eq. 25}$$

$$v_{sQ} = R_s i_{sQ} + L_Q \frac{di_{sQ}}{dt} + \omega_r L_D i_{sD} \qquad \text{eq. 26}$$

$$T_{em} = \frac{3}{2}\frac{P}{2}\{(L_Q - L_D)i_{sD}i_{sQ} + \psi_{PM}i_{sD}\} \qquad \text{eq. 27}$$

In order to design a reluctance machine, the elementary block shown in fig. 11 must be defined.
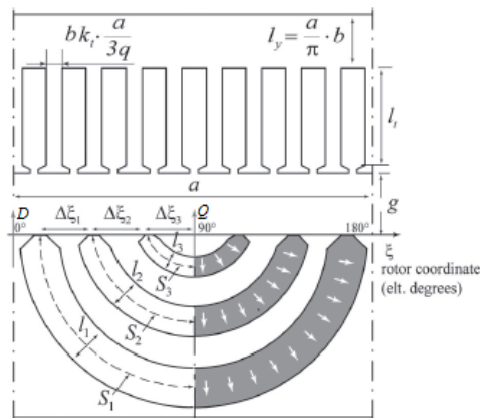
fig. 11: Linearized model of a synchronous reluctance assisted machines, with 3 barriers and permanent magnets magnetized in the radial direction

The parameters in fig. 11 are explained in Table 6:

Table 6: SYMBOLS USED FOR THE DESIGN OF PM-ASSISTED SyRM

Parameter	Meaning
a	Pole-pitch
l_t	Stator tooth height
l_y	Back-iron thickness
b	$B_{gap,d}/B_{fe}$
g	Airgap thickness
q	Number of slot per pole-phase
k_t	Scaling factor for the stator tooth
$\Delta\xi_k$	Rotor slot-pitch
S_k	Rotor barrier half width
l_k	Barrier thickness
N_c	Number of conductors per pole-phase
P	Number of poles
N	Number of turns per phase

As first step in the design of synchronous reluctance machine, it is better to introduce the calculation of the inductances.

Inductances calculation

The calculation of inductances is carried out in p.u., taking the value L_{mD} as base inductance [5].

The inductance L_{mD} is given by the ratio stated in eq. 28:

$$L_{mD} = \frac{\lambda_D}{i_D}$$

<div align="right">eq. 28</div>

where λ_D is given by:

$$\lambda_D = \frac{2\pi r l N}{\sqrt{3}P} B_{gap.d}$$

<div align="right">eq. 29</div>

The inductance along the Q-axis is calculated in such a way that only the magneto-motive force drop along the barriers is considered; consequently, the iron parts in the rotor have a constant magnetic voltage drop. So, the stator magneto-motive force, kept by rotor, is a discrete waveform, as shown in fig. 13; the sample-and-hold action takes place at each rotor slot (that is, the space between two rotor barriers).
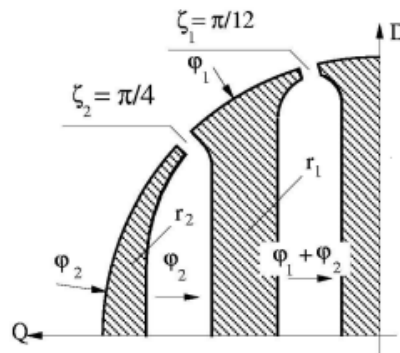
fig. 12: Flux distribution along the Q-axis

In particular from fig. 13, one can notice how the process of sampling works. At each rotor slot, a value from the stator sinusoid is sampled and hold until the next rotor slot. In the case of fig. 12, the rotor slots are in ζ_1 and ζ_2 positions, taking the D-axis as starting axis. So in ζ_1 there is the first sample, then the second sample happens in ζ_2.

fig. 13: Sampling process of the stator MMF

In fig. 14 the magnetic circuit for the case shown in fig. 12 is analyzed. One can notice the reluctances, which are between:

➢ Two rotor magnetic potential r_k and r_{k+1} (barriers reluctances);

➢ Rotor and stator magnetic potential (airgap reluctances).
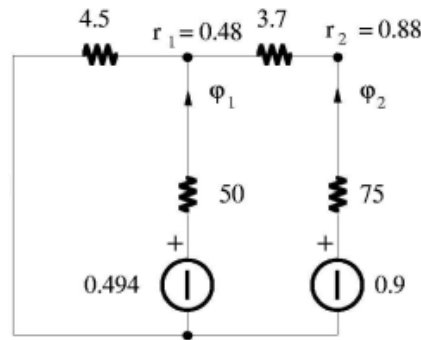
fig. 14: Equivalent magnetic circuit of fig. 12

The reluctance values, which are in the magnetic circuit shown in fig. 14 are in p.u.

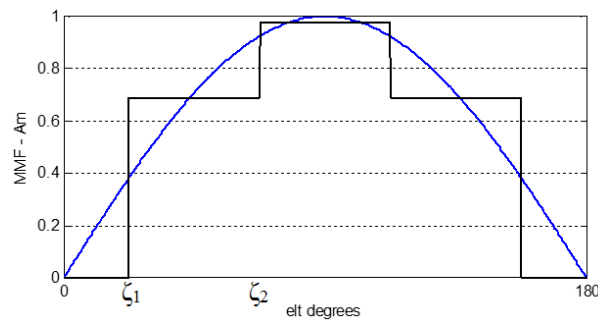With the symbols shown in fig. 15, the following formulas are used for the calculation of Q-axis magnetizing inductance.
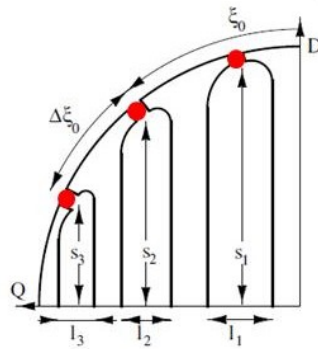
fig. 15: Main geometric dimensions of rotor barriers

In particular, the inductance L_{mQ} in p.u. is given by the sum of two components:

$$\frac{L_{cq}}{L_{mD}} = 1 - \frac{4}{\pi} \sum_k f_k^2 \Delta\xi_k \qquad \text{eq. 30}$$

$$\frac{L_{fq}}{L_{mD}} = \frac{4}{\pi}\left(\frac{P}{2}\frac{k_c g}{l_a}\right)\left(\sum_{k=1}^{n} \Delta f_k \sqrt{\frac{s_k}{r}}\right)^2 \qquad \text{eq. 31}$$

Where L_{cq} is due to the flux circulating at the airgap; L_{fq} is due to the flux flowing through the inner rotor.

Since the method used to draw the rotor barriers has been grabbed from Syre, the iron rotor space must be equal to the stator back-iron thickness; consequently, the room between the shaft and airgap

radius is decreased by l_y; the total air in the rotor is called l_a. l_a must be split among the rotor barriers, on the basis of the assigned p.u. values of each barrier; the same split criterion is used for the calculation of the rotor slot angles.

In order to complete the inductances calculation, it is needed to introduce the p.u. expression of the leakage inductance due to the stator slots [6].

fig. 16: Trapezoidal stator slot

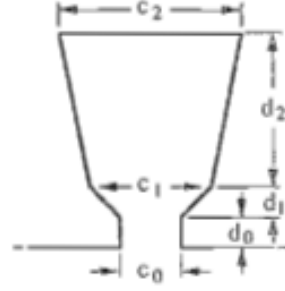Considering the fig. 16, the slot leakage inductance in p.u. is calculated following the eq. 32-eq. 34:

$$p_s = \frac{d_0}{c_0} + \frac{d_1}{c_0}\frac{1}{\frac{c_1}{c_0}-1}\ln\frac{c_1}{c_0} + \frac{d_2}{c_2}h(\beta) \qquad \text{eq. 32}$$

$$h = \frac{\beta^2 - \frac{\beta^4}{4} - \ln\beta - \frac{3}{4}}{(1-\beta)(1-\beta^2)^2}; \beta = \frac{c_1}{c_2} \qquad \text{eq. 33}$$

$$\frac{L_s}{L_{mD}} = \frac{4}{\pi}\left(\frac{P}{2}\frac{k_c g}{r}\right)p_s \sum_k \Delta f_k^2 \qquad \text{eq. 34}$$

The total inductance L_D and L_Q are given by the sum of the magnetizing inductance and the leakage inductance due to the stator slots [5] [6].

1.5. PM-Assisted SyRM design

In order to design a PM-Assisted SyRM prototype machine, it is necessary to do the following hypotheses [2] [7] [8]:

➢ Only rotor typologies called "complete" are considered; that is, each rotor slot pitch is constant along the whole periphery of the rotor;

➢ Only "naturally compensated" machines are analyzed; that is, the current along the Q-axis generates a magnetic flux equals to the flux generated by the magnets at no load, but in the opposite direction;

➢ The ferrite PMs fulfil the rotor barriers completely and they are magnetized in the radial direction.

In these machines, the torque can be expressed by means of eq. 35:

$$T = bB_{fe} \cdot A_{Q0} \cdot 2\pi \cdot r^2 \cdot l \qquad \text{eq. 35}$$

$$\text{where } A_{Q0} = \frac{3\pi}{4\mu_0} \cdot \frac{B_{gap.PM}}{L_{q.p.u.}} \qquad \text{eq. 36}$$

A_{Q0} is the electric loading along the Q-axis and $B_{gap,PM}$ is the airgap flux density due to the permanent magnets at no load.

The base parameters to be defined are:

➢ Airgap thickness (g);

➢ Airgap radius (r);

➢ Number of layers (from the number of layers, it is possible to calculate the number of rotor slots (n_r) per pole pairs; that is, n_r is equal to $4n_{lay} + 2$);

➢ Winding type (q, slot fill factor, winding factor..);

➢ Total machine volume;

➢ Iron saturation level (B_{fe}) and b value (optimum values between 0.5 e 0.65);

➢ Number of pole pairs;

➢ Target torque (T) and efficiency (η).

The steps are the same described for the SPM case. First of all, the cooling type must be defined (Table 2) in order to calculate the outer stator radius R. Since the target torque and the efficiency are known, it is possible to calculate the total losses. All of the losses will be generated by the Joule effect.

1. Calculation of outer stator radius:

$$k_j = \frac{Total\ losses}{Total\ machine\ volume} \frac{R}{2} \qquad \text{eq. 37}$$

From the outer stator radius, it is possible to calculate the axial length of the machine.

From R and b, it is possible to calculate the stator geometry:

2. Calculation of stator geometry:

➢ Stator tooth width (w_t) and stator back-iron thickness (l_y) [7]:

$$w_t = bk_t \frac{a}{3q} \qquad \text{eq. 38}$$

$$l_y = b\frac{a}{\pi} \qquad \text{eq. 39}$$

The stator tooth height can be calculated by the relation shown in eq. 40:

$$R = r + g + l_t + l_y \qquad \text{eq. 40}$$

Knowing the iron flux density B_{fe} and the b value, it is possible to calculate the current i_D value, using eq. 41 and eq. 42 [7]:

$$A_D = \frac{\pi}{2\mu_0} b \cdot B_{fe} \frac{k_c g}{a} \qquad \text{eq. 41}$$

$$A_D = \frac{\pi}{2} \cdot \frac{1}{a} \cdot (\frac{3}{\pi} k_w N_c i_D) \qquad \text{eq. 42}$$

Since the stator geometry and the current i_D are known, it is possible to calculate the i_Q current value. Indeed, the slot area and Joule losses are known; so, it is possible to calculate the maximum current i_0 from eq. 43 [9]:

$$i_0 = \frac{\pi}{3N} R^{1.5} \sqrt{k_{cu} \frac{k_j}{\rho} \frac{l}{l'}} \sqrt{\frac{A_s}{\pi R^2}} \qquad \text{eq. 43}$$

From i_0, it is possible to calculate i_Q thanks to the eq. 44 [9]:

$$i_{sQ} = \sqrt{i_o^2 - i_{sD}^2} \qquad \text{eq. 44}$$

Knowing the i_Q value, it is possible to calculate the remanence of the permanent magnets, using the relations from eq. 45 to eq. 47 [7]:

$$A_Q = \frac{3\pi}{4\mu_0} \frac{B_{gap.PM}}{L_{q.p.u.}} \qquad \text{eq. 45}$$

$$B_{gap.m} = \frac{V_{m.p.u.}}{l_{a.p.u.}} \cdot \frac{\Delta\varepsilon \cdot \cos(\frac{\Delta\varepsilon}{2})}{\tan(\frac{\Delta\varepsilon}{2})} B_{m0} \qquad \text{eq. 46}$$

$$\frac{B_{m0}}{B_r} \approx (1 + \frac{4 \cdot V_{m.p.u.}}{l_{a.p.u.}^2} (1 - \frac{\pi^2}{n_r^2}) \frac{g}{a})^{-1} \qquad \text{eq. 47}$$

Being:

$$V_{m.p.u.} = \frac{n_r l_{a.p.u.}}{2} \frac{\tan(\frac{\Delta\varepsilon}{2}) S_1}{\cos(\frac{\Delta\varepsilon}{2}) a} \qquad \text{eq. 48}$$

$$l_{a.p.u.} = \frac{l_a}{a/2} \qquad \text{eq. 49}$$

$$\Delta\varepsilon = \frac{2\pi}{n_r} \qquad \text{eq. 50}$$

Considering the equations flow from eq. 45 to eq. 47, it is possible to calculate the airgap flux density from eq. 45; then, it is possible to calculate the B_{m0} value from the next equation. Knowing the geometric dimensions of the machine, it is possible to calculate the remanence (eq. 47).

To complete the design of PM-Assisted SyRM prototypes, it is needed to introduce the expression used for calculating the power factor. In the case of naturally compensated machines, the power factor is given by the eq. 51 [7]:

$$\text{PF} = \cos\left(\tan^{-1}\varphi_0\right) = \cos\left(\tan^{-1}\left(\frac{A_d}{A_{q0}}\right)\right) \qquad \text{eq. 51}$$

If the torque value, obtained by the design process, does not fulfil the specification, one can think of:

➢ Increasing the iron flux density level;

➢ Increasing the airgap radius; in this way also the anisotropy will be increased.

Also in this case, there are some drawbacks; if the iron flux density level is increased, the efficiency will be lower, because of iron losses much higher. On the other hand, if the airgap radius is increased, then the machine will have an higher efficiency, also a cost much higher, due to the magnets [7] [9].

1.6. SyRM design

To design the synchronous reluctance machines, it is mandatory to remember that the torque is given by the only magnetic anisotropy of the machine [5] [9]. So, the eq. 52 for the calculation of the torque can be written:

$$T = k_{DQ}\lambda_D i_{sQ} \qquad \text{eq. 52}$$

$$k_{dq} = 1 - L_{mQ.p.u.} \qquad \text{eq. 53}$$

Also in this case, the design process is referred to complete rotor typology only (rotor slot pitch constant along the whole periphery of rotor).

The base parameters to be defined are:

➢ Airgap thickness (g);

➢ Airgap radius (r);

➢ Number of rotor layers (so, the number of rotor slots (n_r) per pole pairs is equal to $4n_{lay} + 2$);

➢ Type of winding (q, slot fill factor, winding factor,..)

➢ Total machine volume;

➢ Iron flux density level (B_{fe}) and b value (optimum values between 0.5 e 0.65);

➢ Number of pole pairs;

➢ Target torque and efficiency.

The method for the design of SyRM is the same described for PM-Assisted SyRM. The only difference is in the permanent magnets, which are absent. Also in this case, if the torque value given by the design process, does not fulfil the specification, both solutions introduced before are available; that is, either increasing the airgap radius or increasing the iron flux density level. In this way, one can think of meeting the specification. The power factor, in the case of synchronous reluctance machines, is given by [6]:

$$PF = \sin(\tan^{-1}\left(\frac{i_Q}{i_D}\right) - \tan^{-1}(\frac{L_Q i_Q}{L_D i_D})) \qquad \text{eq. 54}$$

1.7. Nonlinear effects in SyRM

In synchronous reluctance machines the nonlinear effects are due to:

➢ Stator iron losses;

➢ Torque ripple;

➢ Ribs.

In order to study analytically the stator iron losses, it is needed to describe a method, which is able to calculate the airgap flux density along the Q-axis. The method must be able to solve the magnetic circuit along the Q-axis. In particular, the magnetic model will be developed in p.u., taking the stator MMF as base value [2] [8]. The example machine is shown in fig. 17 and the magnetic circuit for half pole is shown in fig. 18.
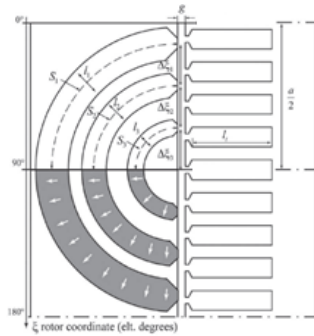

fig. 17: Reference geometry for a rotor with 3 layers. S_{123} are the half lengths of the barriers, the permanent magnets are magnetized in the radial direction, against the Q-axis current
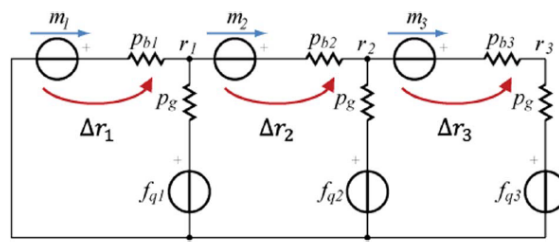

fig. 18: Magnetic circuit for the 3 layers rotor, in case stator MMF is against the permanent magnets

The magnetic circuit permeances are calculated using eq. 55 and eq. 56:

$$p_{pk} = \frac{S_k}{l_k} \qquad \text{eq. 55}$$

$$p_g = \frac{1}{k_c} \cdot \frac{a}{g} \cdot \frac{2}{n_r} \qquad \text{eq. 56}$$

Where S_k are the half lengths of the barriers, while l_k are the thickness of the barriers themselves. The MMF generators have the values stated in eq. 57:

$$m_k = \frac{\frac{B_r}{\mu_0} l_k}{F_Q}$$

eq. 57

Where F_Q is equal to (eq. 58)

$$F_Q = \frac{3}{\pi} \cdot k_w \cdot \frac{2N_c}{P} \cdot I_Q$$

eq. 58

Where B_r is the remanence of the permanent magnets.

Through the Kirchhoff laws, eq. 59 is given:

$$A \cdot \Delta r = B \cdot m + C \cdot \Delta f_q$$

eq. 59

Where A, B e C are matrices and they depend on the rotor geometry; A, B, C are symmetric.

After the magnetic potentials are calculated by the Δr values, it is possible to calculate the airgap flux density through the eq. 60:

$$B_{gQ} = (F_Q - k_f r_3) \cdot \frac{\mu_0}{k_c g}$$

eq. 60

In the eq. 60, r_3 is the maximum value of the rotor magnetic potential (fig. 19), meanwhile, k_f is the form factor, which takes into account the rotor magnetic potential, which is not a sinusoidal waveform [2] [7] [8].
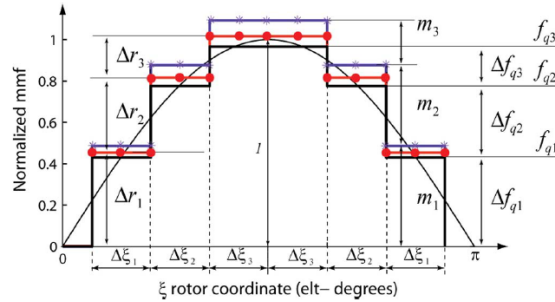

fig. 19: Stator MMF in p.u. and rotor MMF along the Q-axis

The stator iron losses can be split along the D and Q-axes (the rotor losses can be neglected because the airgap flux density is in synchronism with the rotor). The airgap flux density along the Q-axis, calculated before, is referred to the main harmonic; in order to calculate the iron losses due to the other harmonics, it is needed to introduce the eq. 61:

$$B_{gQh} = \frac{\mu_0}{k_c g_e} \frac{4}{\pi} r_3 \frac{k_r}{h}$$

eq. 61

where, k_r is equal to:

$$k_r(h) = (1 - \frac{r_2}{r_3}) \sin(h\alpha_3) + (\frac{r_2}{r_3} - \frac{r_1}{r_3}) \sin(h\alpha_2) + (\frac{r_1}{r_3}) \sin(h\alpha_1)$$

eq. 62

h is the harmonic order (1, 3, 5, 7..); meanwhile, the angles α_k indicate the distance of rotor slots from the Q-axis. Since the harmonic content is known, it is possible to calculate the iron losses, thanks to eq. 63 and eq. 64:

$$P_{ec_{tooth}} = k_e f_1^2 \sum_{h=1}^{\infty} h^2 \hat{B}_{gQ}^2 \cdot Filter(B_t)^2 \qquad \text{eq. 63}$$

$$P_{ec_{yoke}} = k_e f_1^2 \sum_{h=1}^{\infty} h^2 \hat{B}_{gQ}^2 \cdot Filter(B_y)^2 \qquad \text{eq. 64}$$

Where the filter-functions have the expressions stated in eq. 65 and eq. 66:

$$Filter(B_y) = \frac{r}{l_y} \cdot \frac{2}{hP} \qquad \text{eq. 65}$$

$$Filter(B_t) = \frac{r\alpha_s}{w_t} \cdot sinc(\frac{hP\alpha_s}{4\pi}) \qquad \text{eq. 66}$$

So, h is the harmonic order; α_s is the rotor slot-pitch in radians and it is given by the ratio between 2π and the number of rotor slots (n_r) [10].

For calculating the losses along the D-axis, it is necessary to know the iron flux density value B_{fe}, using the relation, which connects $B_{gap,D}$ and the quantity of iron in the stator. The quantity of iron in the stator is calculated at half stator tooth (R_m). From the B_{fe} value, using the Steinmetz equation (eq. 24), it is possible to calculate the iron losses along the D-axis, using the fundamental frequency [7]. In the end, the iron losses along the D and Q-axes are summed directly.

Regarding the calculation of the torque ripple, only the interactions between the stator and rotor harmonics are considered. The MMF, in a star floating connection winding, can be expressed through the relation eq. 67, if the three phase currents are symmetric and balanced [11].

$$f_s = \sum_{h \neq 3.6.9 \dots} 1.5 n_h i_m \cos(h\theta \pm \omega_r t \pm \gamma_d) \qquad \text{eq. 67}$$

γ_d is the current phase measured in dq system reference (it is needed to add 90° electrical degrees to the phase current used in the DQ system reference).

The rotor harmonics are created by the rotor slots themselves, through the sample and hold process described before; the rotor harmonics have the expression reported in eq. 68:

$$f_r = \sum_{h \neq 2.4 \dots} f_{r.h} \cos(h\theta) \qquad \text{eq. 68}$$

The analytical relation used to calculate the torque ripple is (eq. 69):

$$\frac{T_{ripple}}{T_1} = -\frac{1}{\sin \gamma_d} \cdot \sum_{\substack{h=6m\pm1 \\ m=1.2.3\dots}} \left[h \left(\frac{f_{s.h}}{f_{s.1}}\right) \left(\frac{f_{r.h}}{f_{r.1}}\right) \sin((h \pm 1)\omega_e t \pm \gamma_d) \right] \qquad \text{eq. 69}$$

It is mandatory to say that the analytical expression of the torque ripple is valid when:

➢ The stator slots are closed;

➢ It is possible to neglect the magnetic voltage drop due to the flux, which flows through the ribs and barriers;

➢ It is possible to neglect the MMF due to the permanent magnets.

In addition,

➢ Only stator components and rotor components of the same order can interact each other;

➢ The sign of harmonic components inside the sine function is:

▪ Positive when the harmonic order: $h = 6m - 1$, with $m = 1,2,3,..$

▪ Negative when the harmonic order: $h = 6m + 1$, with $m = 1,2,3,..$

➢ The harmonic content of the torque ripple will be composed of all multiples of 6;

For example, if a 2 pole machine is analyzed, with 9 stator slots, the stator harmonic content of the winding, normalized with respect to the fundamental one, will be (fig. 20):
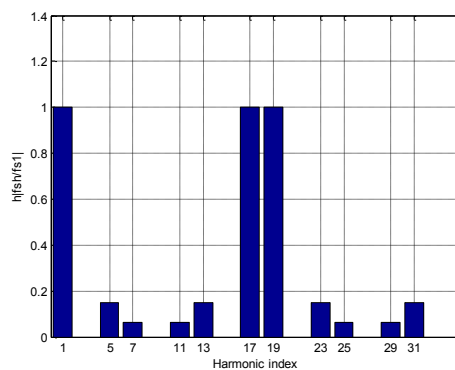

fig. 20: Normalized harmonic content of stator MMF

In particular, in fig. 20 the harmonics are multiplied by the harmonic order.

If the rotor has 2 layers, the harmonics, normalized with respect to the fundamental one, will be (fig. 21):
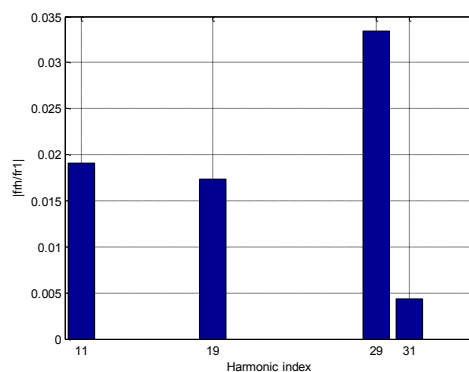

fig. 21: Normalized harmonic content of the rotor MMF

In fig. 21 are shown only the rotor harmonics, which are capable to generate torque ripple (that is, $11^{st}, 19^{th}, 29^{th}, 31^{st}$) [11] [12].

Finally, speaking about the non linear effects, the ribs have a particular role. In fact, they reduce the torque value due to the leakage flux; the phenomenon is more severe in the reluctance machines (SyRM); indeed, in PM-Assisted SyRM machines, the ribs are saturated by the permanent magnets; consequently, their presence can be neglected.
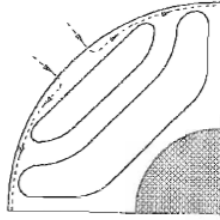

fig. 22: Leakage flux and its path through ribs

The flux, which flows through the ribs, is a leakage flux. The analytical expression of the leakage flux is given by eq. 70:

$$\lambda_r = \frac{4}{\sqrt{3}} wlNB_s \qquad \text{eq. 70}$$

Where w is the rib thickness, while B_s is the saturation value of the ribs; therefore, the torque expression is modified as eq. 71 shows:

$$T = \frac{3}{2}\frac{P}{2}\{k_{DQ}\lambda_D i_Q - \lambda_r i_D\} \qquad \text{eq. 71}$$

So, the flux λ_r represents a part of the leakage flux; consequently, the L_Q inductance will increase; such phenomenon has been taken into account during the development of the analytical tool [6] [9].

1.8. Optimization algorithm for weight and cost

The electrical machine to be designed must move a mechanical gear pump. The pump is a component of the low pressure part of a diesel injection system. In particular, the electrical machine must have a rated mechanical power equal to about 350 [W]. The rated values of speed and torque are 8500 [rpm] and 0.4 [Nm], respectively. The operating condition considered during the electromagnetic design of the electrical machine is at 2700 [rpm] with a load torque equal to 0.4 [Nm]. In practical applications, it is expected that the maximum speed reached by the electrical machine will increase with the time due to the degraded condition of the filter located at the pump output. The rated speed is expected to be reached only in unlikely conditions when the filter is at the end of his life time. The speed equal to 2700 [rpm] is expected for the pump with regular maintenance and it is considered to be the most representative of the actual pump operation. Another

important specification is the electrical machine efficiency, which must be equal to or higher than 80%.

Summing up, the specifications to be verified are as follows:

➢ Target torque: 0.4 [Nm];

➢ Target speed: 2700 [rpm];

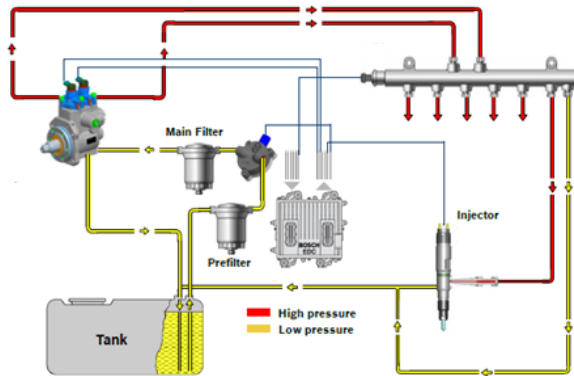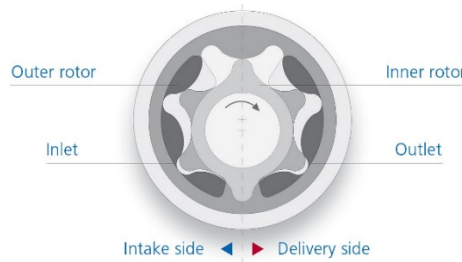➢ Minimum efficiency: 80%.

fig. 23: Diesel injection system

fig. 24: Generic gerotor similar to that used in the application under study

The motor typologies considered are:

➢ Surface permanent magnet motors;

➢ Reluctance motors;

➢ PM-assisted reluctance motors.

Thanks to the optimization genetic algorithms, the optimum machine, which satisfies the specifications of weight and cost can be found.

The main parameters to be optimized are the geometric ones (such as: stator tooth height, airgap radius...). If the motor has permanent magnets, also the remanence is a parameter to be optimized. As fitness function, the analytic model developed and described before is used; the analytic tool has been modified for this purpose. It is needed to specify that the analytic tools are able to consider all the reluctance machines types; not only the regular ones. This is connected to the possibility to calculate the rotor angles, thanks to Syre parameterization. In addition, since the current is given by the admitted Joule losses and the remanence is a parameter to be optimized, the PM-assisted

reluctance machines are not naturally compensated, but have the same behaviour of a generic IPM machine (in fact, the compensation between the stator flux along the Q-axis and the flux due to permanent magnets at no load is likely to happen during the optimization process).

Some penalty factors are applied to the cost function optimized by the search algorithm. The search algorithm tries to optimize the total cost and the total weight of the electrical machines analyzed. The penalty factors depend on the target torque and efficiency. Each time, a machine does not fulfil the target values, it will be penalized in such a way that it will be moved away from the Pareto front.

An example of MatLab code for the optimization of a SPM motor is given in appendix.

To calculate the cost of the machine, the index prices reported in table 7 are used. The reported prices are not fully representative of the current market status. They just suit as ballpark figure for calculation purposes.

After the machine is given by the optimization process, it will be simulated by means of the software MotorSolve, in order to confirm the analytic design.
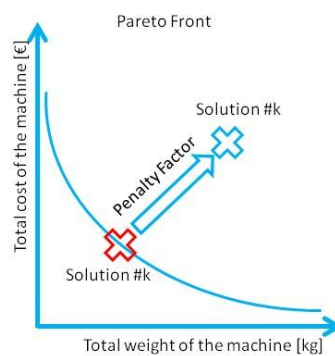

fig. 25: Action of penalty factors

Table 7: INDEX PRICES

Machine part	Price
Stator	2 €/kg
Rotor	13 €/kg
Rare Heart PM	100 €/kg
Copper	7 €/kg

1.9. SPM: optimization results

Only a part of the admitted losses will be Joule ones (the Joule losses part is indicated by "x" in the analytic tool). In fact, the tool is able to calculate the iron losses; so, it must select the admitted Joule losses in order to select the proper value of current in order to accomplish the target torque and efficiency.

The optimum machine must fulfil the following requirements:

➢ Airgap thickness (g) equal to a 1 [mm];

➢ Number of pole pairs equal to 4;

➢ Shaft radius (r_a) equal to 20 [mm];

➢ Remanence (B_r) equal to 1.07 [T];

➢ Maximum outer stator diameter (2R) equal to 85 [mm];

➢ Axial length (l) equal to 15 [mm];

➢ Operating temperature equal to 90 [°C].

The number of slots chosen is equal to 12; in this case, the winding is tooth-winding like. The combination 12 slots/8 poles was chosen. The only parameters to be optimized will be the geometric ones (the search space is shown in Table 8). In particular the geometric parameters are about the stator and the shape of the magnets.

Table 8: SPM: SEARCH SPACE

Parameter	Range
Tooth width [mm]	[3.33 6]
Tooth height [mm]	[8.1 14.6094]
Magnet Thick. [mm]	[3 5]
Magnet Span [mech. Deg]	[31.5 40.5]
x	[0.7 0.9]

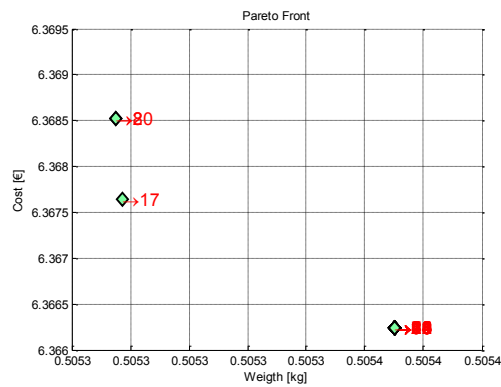The Pareto front given by the optimization process is shown in fig. 26:

fig. 26: SPM Pareto front

The solutions are close each other; so, it is not very important which solutions one decides to pick-up; in fact, the geometric dimensions are similar. In particular, it is evident the action of the penalty factors, which move away all the solutions not satisfying the requirement about the efficiency and the torque from the Pareto front. This observation is valid for the other optimized machines shown in the following.

From the Pareto front, the machine number 17 was chosen; this is shown in fig. 27 with the main geometric dimensions.

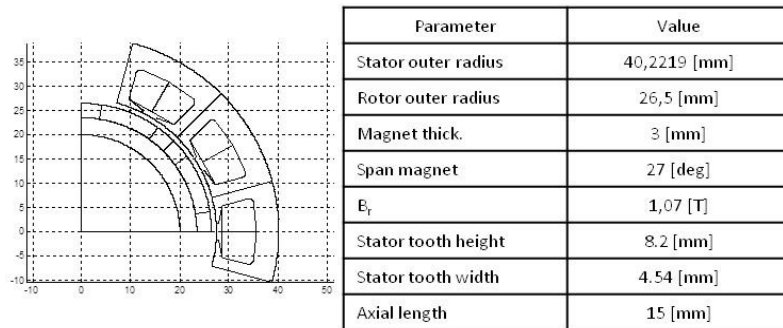| Parameter	Value
Stator outer radius	40,2219 [mm]
Rotor outer radius	26,5 [mm]
Magnet thick.	3 [mm]
Span magnet	27 [deg]
B_r	1,07 [T]
Stator tooth height	8.2 [mm]
Stator tooth width	4.54 [mm]
Axial length	15 [mm]

fig. 27: Machine n. 17 from SPM Pareto front

The analytic and FEM results are shown in Table 9:

Table 9: PERFORMANCE SPM

Parameter	Analitic	MotorSolve
T [Nm]	0.4	0.43
PF	0.998	0.996
Copper Losses [W]	14.71	11.4
Stator Iron Losses [W]	2.21	3.48
Eff. [%]	87	88.7
L_d [µH]	0.26	0.3
Current [A_{pk}]	148	148

In fig. 28 is reported the FEM simulation, regarding the magnetic flux at no load. Although the permanent magnet thickness is lower than 5 times the airgap thickness, the permanent magnets are not subjected to demagnetizing.
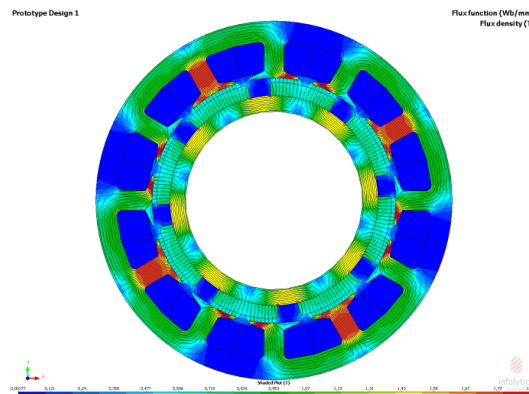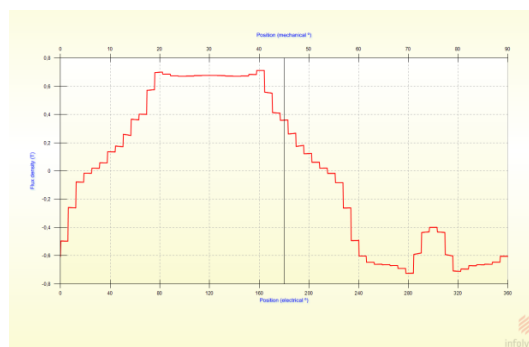

fig. 28: Flux function at no load

fig. 29: Airgap field at no load

In addition, from fig. 29, one can notice the maximum value of the magnetic field at the airgap; it is about 0.67 [T]. Instead, the analytic tool has estimated a value equal to 0.6 [T]. This confirms the

good reliability of the tool in the preliminary optimization phase of surface permanent magnet motors.

1.10. SyRM: optimization results

As said, a valid alternative to the SPM motors are the reluctance machines. The reluctance machines work in a better way if the winding is characterized by an integer q value (full-pitch winding). Since the number of pole pairs was given, only the number of stator slots will be modified, in order to investigate if it exists a valid alternative to SPM motors, using the same number of pole pairs. For this reason, the combinations 24 slots/8 poles and 48 slots/8 poles have been chosen. For 24 slots/8 poles case, the winding arrangement is shown in fig. 30:
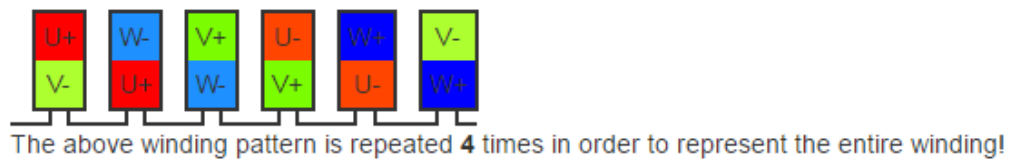

fig. 30: Configuration 24 slots/8 poles, Double-Layer, kw=0.866, Coil Span=2 slot

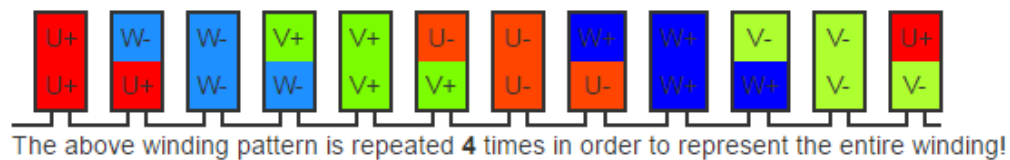Instead, for the 48 slots/8 poles case, the winding layout is (fig. 31):

fig. 31: Configuration 48 slots/8 poles, Double-Layer, kw=0.933, Coil Span=5 slot

The search space was set in such a way that the maximum outer diameter is equal to 340 [mm]; while, the minimum outer diameter value is equal to about 80 [mm]. The search space is shown in Table 10:

Table 10: SyRM: SEARCH SPACE

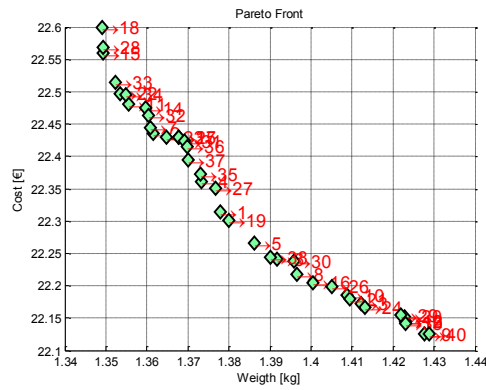| Parameter	Range
Tooth width [mm]	[1.3823 6.9115]
Tooth height [mm]	[8.5 42.5]
Barrier Thick. [pu]	[0.2 1]
Barrier Angle [pu]	[0.25 0.5]
Rotor outer radius [mm]	[27.5 110]
Axial length [mm]	[15 54]
B_r	[0 1.07]
x	[0.8 0.95]

➢ PM-Assisted SyRM 24 slots / 8 poles

fig. 32: PM-Assisted SyRM 24 slots / 8 poles Pareto front

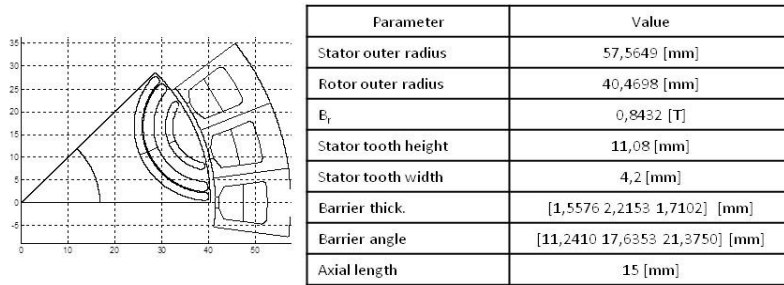| Parameter	Value
Stator outer radius	57,5649 [mm]
Rotor outer radius	40,4698 [mm]
E_r	0,8432 [T]
Stator tooth height	11,08 [mm]
Stator tooth width	4,2 [mm]
Barrier thick.	[1,5576 2,2153 1,7102] [mm]
Barrier angle	[11,2410 17,6353 21,3750] [mm]
Axial length	15 [mm]

fig. 33: Machine n. 5 from PM-Assisted SyRM 24 slots / 8 poles Pareto front

Table 11: PERFORMANCE PM-ASSISTED SyRM 24 SLOTS / 8 POLES

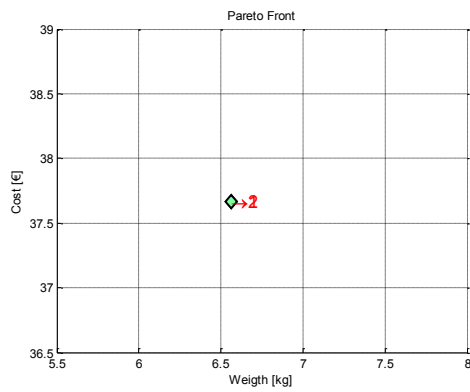| Parameter	Analitic	MotorSolve
T_{total} [Nm]	0.4	0.382
T_{rel} [Nm]	0.0075	0.025
PF	0.7152	0.71
Copper Losses [W]	25.42	18
Stator Iron Losses [W]	2.5	4.3
Eff. [%]	80	83
L_d [μH]	2.1	2
L_q [μH]	6	4.5
Phase current [deg.]	60	60
Current [A_{pk}]	93.3	93.3

➢   SyRM 24 slots / 8 poles

fig. 34: SyRM 24 slots / 8 poles Pareto front

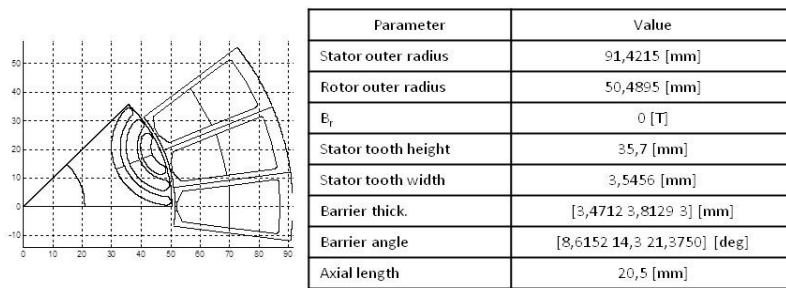| Parameter	Value
Stator outer radius	91,4215 [mm]
Rotor outer radius	50,4895 [mm]
E_r	0 [T]
Stator tooth height	35,7 [mm]
Stator tooth width	3,5456 [mm]
Barrier thick.	[3,4712 3,8129 3] [mm]
Barrier angle	[8,6152 14,3 21,3750] [deg]
Axial length	20,5 [mm]

fig. 35: Machine n. 1 from SyRM 24 slots / 8 poles Pareto front

Table 12: PERFORMANCE SyRM 24 SLOTS / 8 POLES

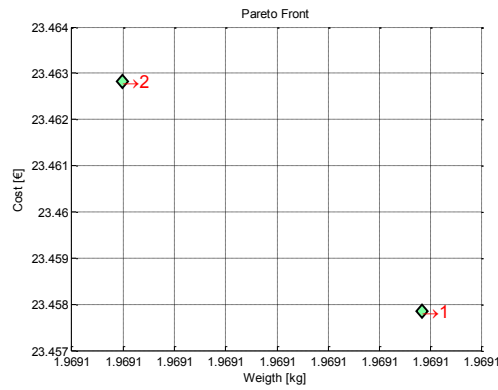| Parameter	Analitic	MotorSolve
T_{total} [Nm]	0.4	0.283
T_{rel} [Nm]	0.4	0.283
PF	0.2725	0.3
Copper Losses [W]	24	26
Stator Iron Losses [W]	4	6
Eff. [%]	80	71
L_d [µH]	5.2	5.5
L_q [µH]	10	8.4
Phase current [deg.]	67.4	67.4
Current [A_{pk}]	200.34	200.34

➢ PM-Assisted SyRM 48 slots / 8 poles

fig. 36: PM-Assisted SyRM 48 slots / 8 poles Pareto front

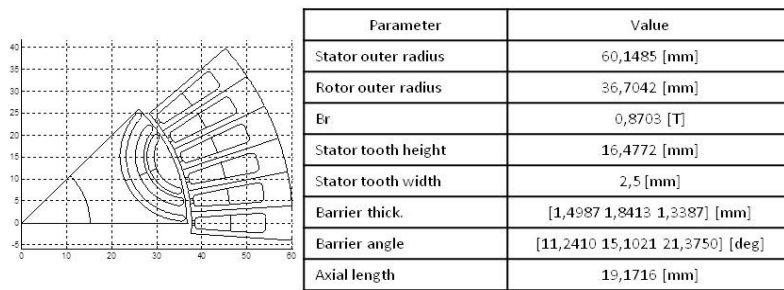| Parameter	Value
Stator outer radius	60,1485 [mm]
Rotor outer radius	36,7042 [mm]
Br	0,8703 [T]
Stator tooth height	16,4772 [mm]
Stator tooth width	2,5 [mm]
Barrier thick.	[1,4987 1,8413 1,3387] [mm]
Barrier angle	[11,2410 15,1021 21,3750] [deg]
Axial length	19,1716 [mm]

fig. 37: Machine n.1 from PM-Assisted SyRM 48 slots / 8 poles Pareto front

Table 13: PERFORMANCE PM-ASSISTED SyRM 48 SLOTS / 8 POLES

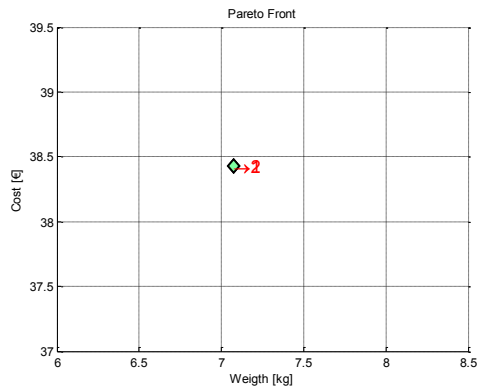| Parameter	Analitic	MotorSolve
T_{total} [Nm]	0.4	0.518
T_{rel} [Nm]	0.0045	0.042
PF	0.8	0.72
Copper Losses [W]	23.05	19.6
Stator Iron Losses [W]	2.6	4
Eff. [%]	81.5	86
L_d [μH]	12	11
L_q [μH]	30	25
Phase current [deg.]	61.5	61.5
Current [A_{pk}]	52	52

➤ SyRM 48 slots / 8 poles

fig. 38: SyRM 48 slots / 8 poles Pareto front

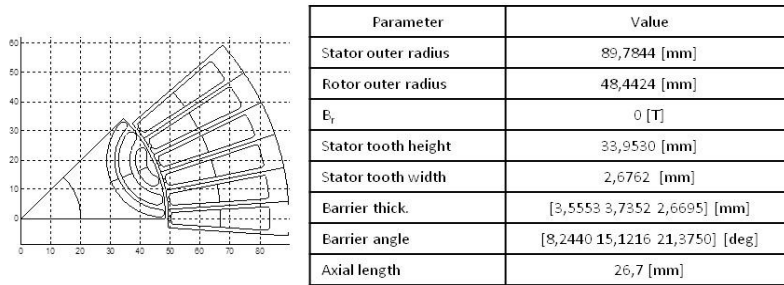| Parameter	Value
Stator outer radius	89,7844 [mm]
Rotor outer radius	48,4424 [mm]
B_r	0 [T]
Stator tooth height	33,9530 [mm]
Stator tooth width	2,6762 [mm]
Barrier thick.	[3,5553 3,7352 2,6695] [mm]
Barrier angle	[8,2440 15,1216 21,3750] [deg]
Axial length	26,7 [mm]

fig. 39: Machine n.1 from SyRM 48 slots / 8 poles Pareto front

Table 14: PERFORMANCE SyRM 48 SLOTS / 8 POLES

Parameter	Analitic	MotorSolve
T_{total} [Nm]	0.4	0.356
T_{rel} [Nm]	0.4	0.356
PF	0.2356	0.337
Copper Losses [W]	24	25
Stator Iron Losses [W]	3.3283	5
Eff. [%]	81	77
L_d [μH]	32	34
L_q [μH]	54	46
Phase Current [deg.]	87.2	87.2
Current [A_{pk}]	64	64

To sum up the results obtained, the Table 15 shows the size, weight and cost of the optimum machines.

Table 15: OPTIMUM MACHINES COMPARISONS

Machine Type	Stator outer diameter [mm]	Axial length [mm]	Cost [€]	Weight [kg]
SPM	80.44	15	6.4	0.51
SyRM – 24 / 8	182.8431	20.5	33.44	6.237
PM-Assisted SyRM – 24/8	115.13	15	14.45	1.233
SyRM – 48 / 8	179.5687	26.7	33.36	6.685
PM-Assisted SyRM – 48 / 8	120.3	19.1716	12.94	1.81

From a point of view of cost and weight, the SPM machine seems to be the most suitable for the purpose; having a cost equal to 6.4 [€] and a weight equal to 0.51 [kg].

One can notice that in the case of 24 slots/8 poles configuration, the synchronous reluctance machine has a torque lower than the one calculated by FEM simulations; the reason is in the reluctance machine winding factor, which is lower than 0.9 (exactly, the winding factor is equal to 0.833); the analytic tool considers turns distributed in a sinusoidal way. So, the lower is the winding factor, the less reliable are the analytic estimations of torque.

1.11. Torque ripple remark

In this paragraph the torque ripple for the machine with 48 slots and 8 poles is analyzed.

In the case of synchronous reluctance machine, the torque is generated by the magnetic anisotropy. The torque waveform is shown in fig. 40 and it was obtained by using software MotorSolve. In particular only 90 mechanical degrees have been considered, which correspond to 360° electrical degrees. The fig. 41 shows the harmonic content of the torque itself. The torque ripple calculated by the analytic tool is equal to about 7.6% (the torque ripple is given by sum of the normalized harmonic components shown in figures); while, from FEM simulations a value equal to 16.72% is obtained (for the calculation of torque ripple only the 6th, 12th and 18th are taken into account).
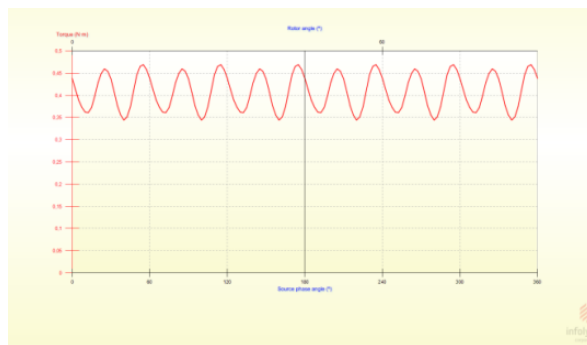

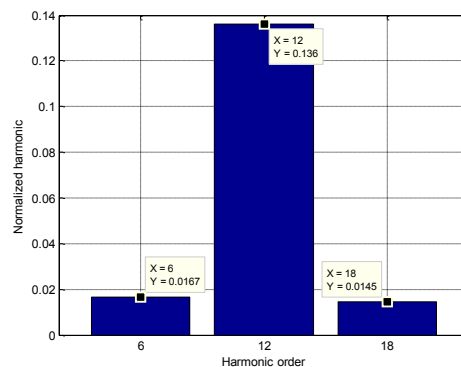fig. 40: Torque for SyRM 48 slots/8 poles calculated by FEM

fig. 41: Torque harmonic content of SyRM 48 slots/8 poles obtained by FEM simulations, normalized using the mean value of torque
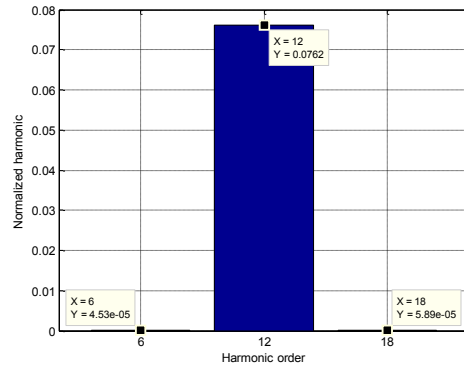
fig. 42: Torque harmonic content of SyRM 48 slots/8 poles obtained by analytic tool, normalized using the mean value of torque

When the permanent magnets fulfil the rotor barriers (that is, the PM-assisted reluctance machine is analyzed), the torque is shown in fig. 43. From FEM simulations, a torque ripple equal to 7.6% is obtained; the same is obtained by using the analytic tool.
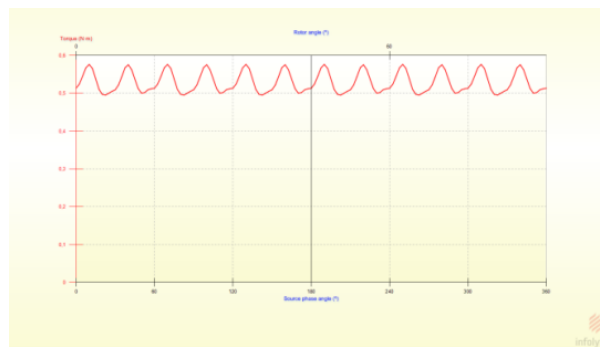

fig. 43: Torque for PM-Assisted SyRM 48 slots/8 poles calculated by FEM
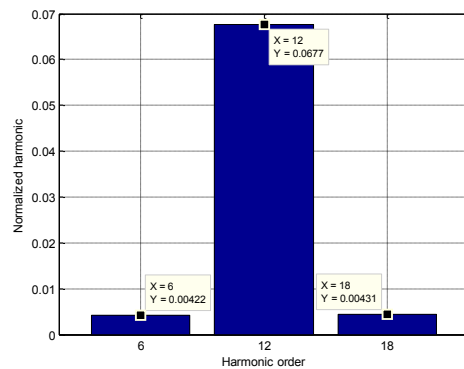

fig. 44: Torque harmonic content of PM-Assisted SyRM 48 slots/8 poles obtained by FEM simulations, normalized using the mean component value of torque
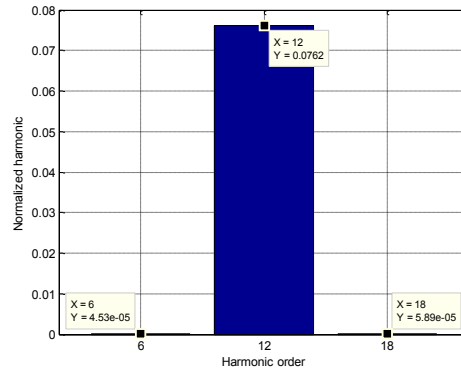
fig. 45: Torque harmonic content of PM-Assisted SyRM 48 slots/8 poles by analytic tool, normalized using the mean component value of torque

The torque ripple estimated by the analytic tool is about the same for both reluctance machines, since the current magnitude of the two machines are almost equal each other, as well as the phase (about 60°). So, when the machine is equipped with magnets, the torque ripple estimation is quite good; if the machine is without magnets, the torque ripple estimated by the analytic tool is lower than FEM one. This can be explained saying that the ribs in the synchronous reluctance machines are not saturated in normal operating conditions; so, their presence cannot be neglected. Although the analytical tool gives a good estimation of the torque ripple, the best way, to optimize it, is by means of FEM simulations; in fact, only using FEM simulations, the side effects given by permanent magnets, stator slots and ribs are taken into account at the same time. For all these reasons, the ripple calculation has been not used in the optimization tool.

1.12. Stator winding design

From the previous analysis, it is clear that the surface permanent magnet machine be the most suitable for moving the mechanical pump; in fact, it has a lower cost and weight than the other machines considered. In order to complete the design, it is necessary to provide some guidelines for the construction of the stator winding. In fact, the tool considers only one turn for each coil; in the case of a surface permanent magnet machine, the number of coils is 4, which is also the number of parallel paths to be used in the design of the stator winding.

In Table 16 are shown the typical slot current density values [3]:

Table 16: TYPICAL VALUES OF SLOT CURRENT DENSITY IN [A/mm^2]

Cooling type	Current density
TENV (Totally enclosed; not ventilated)	1.5 – 5
Air over; fan-cooled	5 – 10
Liquid cooled	10 – 30

Using eq. 72, it is possible to compare the slot current density with the reference values; this helps understanding in which operating condition the motor is.

$$J = \frac{Number\ of\ layers \cdot 3 \cdot MMF_{rms}}{Q \cdot SFF \cdot A_{slot}}$$

eq. 72

In eq. 72 the parameters have the following meanings:

- ➢ SFF: Slot fill factor;
- ➢ A$_{slot}$: Slot area;
- ➢ MMF: Magneto-motive force;
- ➢ Q: Number of slots.

The MMF value is known from the design of the motor; so, thanks to eq. 72, it can be stated that the machine can be totally enclosed; in fact, in this case, the result of the calculation gives the value 2 [A/mm^2].

In fig. 46 there are the diameters of copper wires, used for stator winding construction purposes. It could be useful to choose nominal sections lower than 0.71 [mm], in order to build the stator winding more easily.

Copper internal diameter [mm]	Section [mm²]	Electr. Resistivity [Ω/km] at 20 [°C]
0.04	0.00126	13720
0.05	0.00196	8781
0.063	0.00283	5531
0.071	0.00395	4355
0.08	0.00503	3430
0.09	0.00636	2710
0.1	0.00785	2195
0.112	0.00984	1750
0.125	0.01226	1405
0.14	0.01539	1120
0.16	0.02011	857.5
0.18	0.2545	677.5
0.2	0.03142	548.8

fig. 46: Copper wire dimensions for stator winding

Before choosing the wire diameter, it is necessary to calculate the skin depth, using eq. 73:

$$\delta = \sqrt{\frac{\rho}{\pi f \mu_0}}$$ eq. 73

Since the maximum frequency is equal to 200 [Hz], the skin depth is about 5 [mm]; this value is lower than the maximum wire diameter considered (i.e., 0.71 [mm]); so, the litz-wire is not useful in this case.

The maximum line voltage induced in a coil with a single turn is given by (eq. 74):

$$E_\Delta = \frac{T \omega_m}{3 \cdot MMF \cdot \cos \varphi \cdot a} \sqrt{2}$$ eq. 74

where:

- ➢ a: Number of parallel paths;
- ➢ MMF: Stator magneto-motive force;
- ➢ cosφ: Power factor;
- ➢ T·ω$_m$: Mechanical power.

From eq. 74, it is possible to calculate the peak value of E$_\Delta$, which is equal to 0.13 [V].

The number of turns is selected so that to fulfil the rated voltage requirement, also considering the available DC bus voltage.

CHAPTER II

2. IEEE 1812-2014

The IEEE 1812-2014 standard is a reference guide for conducting tests on permanent magnet motors in order to determine their performance and parameters. The tests described could be applied to both motors and generators. It is mandatory to specify that the following guide does not contain all the possible tests that could be made on permanent magnet machines; in fact, it describes general and non-specific methods that could, for example, be required in the search field.

The guide constitutes a set of steps necessary for the first commissioning of permanent magnet electric machines [13].

The standard IEEE 1812 is composed of six parts, that is:

➢ Part I: Purpose and instrumentation;

➢ Part II: Normative references;

➢ Part III: Condition and integrity tests (resistance measurement, vibrations, acoustic noise..);

➢ Part IV: Steady-state tests (open-circuit tests, short-circuit tests...);

➢ Part V: Transient tests (retardation test, sudden short-circuit test);

➢ Part VI: Machine operating characteristics (losses and efficiency, torque ripple).

The part VI is the most important chapter of the guide, because it describes the main methods for the characterization of mechanical losses and the methodology to be used in order to calculate the efficiency. This is useful to confirm the initial project.

In this chapter, the machine prototype realized will be described. Then, the tests performed on it.

2.1. Description of the prototype

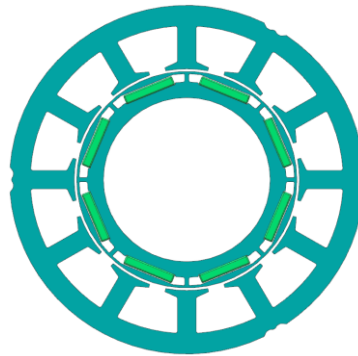An appearance of the prototype analyzed is shown in fig. 47:

fig. 47: IPM machine similar to the prototype used

The machine has 12 slots and 8 poles; the stator winding is delta connected and it is double-layer (tooth-winding) as fig. 48 shows. For this configuration, the winding factor is equal (k_w) to 0.866.

fig. 48: Winding periodicity of the prototype analyzed

The four coils of each phase are connected in parallel and they consist of 53 turns.
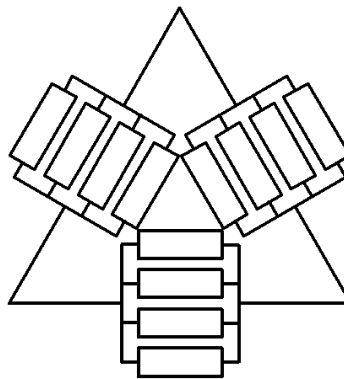

fig. 49: Winding configuration of the prototype analyzed

The main dimensions of the machine are summarized up in Table 17. In this table is pointed out also the weight.

Parameter	Value
Stator outer radius [mm]	42.5
Shaft radius [mm]	20
Weight [kg]	0.652

The rotor has been realised massive instead of laminated. In particular, the rotor is a sintered steel [14]. The fact that the rotor is massive, has a negligible effect on the performance of the machine. The sintered material features are:

Table 18: SINTERED MATERIAL FEATURES

Characteristics	Value
Density [g/cm^3]	6.4-6.8
Hardness HB	>120
Radial Strength [N/mm^2]	360

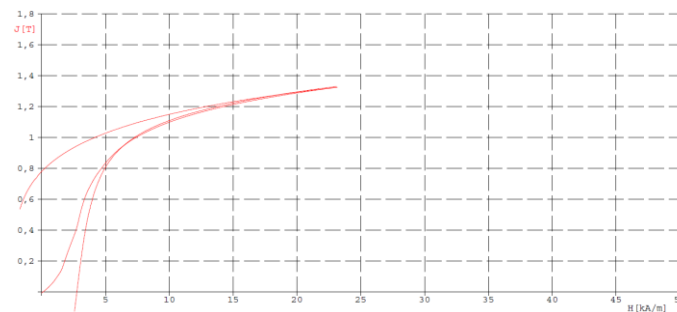The BH characteristic is shown in fig. 50:

fig. 50: Sintered material - BH characteristic

Summarizing up, every single part of the machine is made up of:

Table 19: PROTOTYPE MATERIALS

Machine part	Material
Laminated Stator	Electrical steel M400-50A
Solid Rotor	Sintered steel (D39)
Magnet	Sm-Co rare earths magnets (Recoma 26-HE)
Shaft	Aluminium

In fig. 51 are shown the demagnetization curves of the permanent magnet used (Recoma 26-HE).
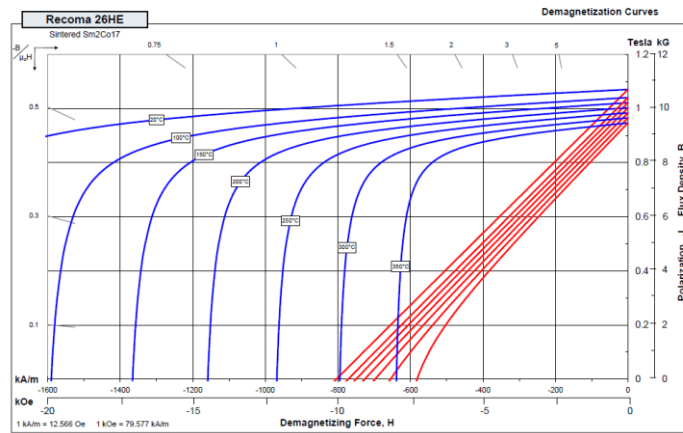

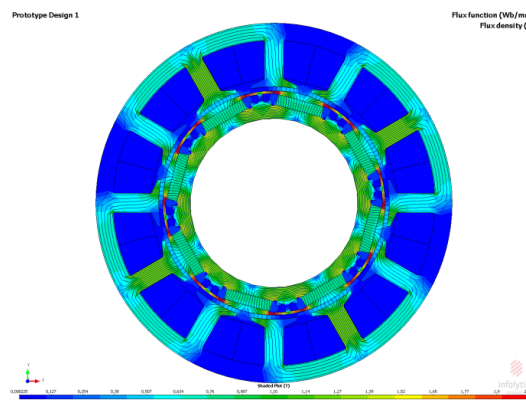fig. 51: Demagnetization curves of permanent magnet Recoma 26-HE

fig. 52: Flux function at no load of the prototype realized by Bosch
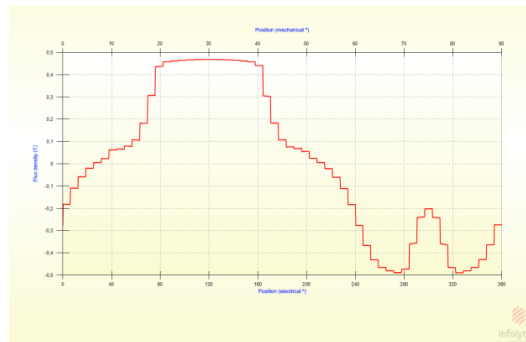
fig. 53: Airgap field at no load of the prototype realized by Bosch

From FEM simulations (fig. 52 and fig. 53), one can notice that the maximum airgap flux value is about 0.48 [T]. Instead, in the SPM machine designed in chapter I, the airgap flux has a value equal to 0.7 [T]. If the magnet thickness of the SPM is decreased until 2.5 [mm], the airgap flux becomes equal to 0.6 [T] (fig. 54). Concluding, the machines are almost equal each other, although the SPM machine has a power density, which is a bit higher than analyzed prototype; for this reason, the SPM machine could be a valid alternative to the prototype realized by Bosch.
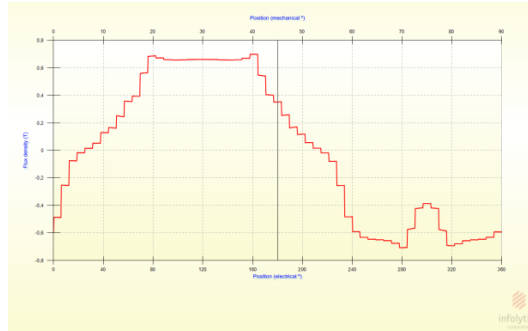
fig. 54: Airgap field at no load of the optimized SPM with magnet thickness equal to 2.5 [mm]

2.2. FEM characterization of the prototype
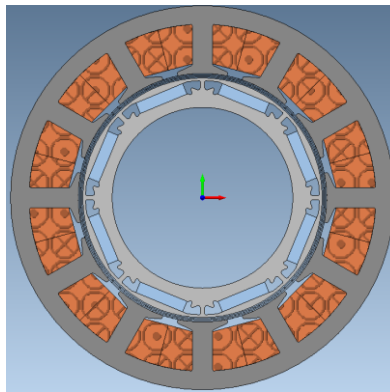
fig. 55: FEM model of the prototype

The FEM analysis have been pursued on the machine for the following mechanical speeds:

➢ 8500 [rpm];

➢ 2700 [rpm];

➢ 1500 [rpm].

The temperature of the FEM model has been set equal to 90 [°C], in particular, the simulations have been performed, considering the machine must deliver a torque equal to 0.3 [Nm]; the simulation results are in Table 20:

Table 20: FEM SIMULATION RESULTS

| Parameter	8500 [rpm] / 0.3 [Nm]	2700 [rpm] / 0.3 [Nm]	1500 [rpm] / 0.3 [Nm]
Torque [Nm]	0.3	0.3	0.3
Torque ripple [%]	7.1	6.5	6.2
Copper Losses [W]	20.8	20.8	20.8
Stator Iron Losses [W]	8.6	1.5	0.7
Rotor Iron Losses [W]	1.1	1.1	1.1
Phase Voltage [V_{rms}]	6.04	2.15	1.34
Phase Current [A_{rms}]	19.6	19.6	19.6
Power factor	0.84	0.86	0.88
Efficiency [%]	89.75	78.36	67.62
$L_{d\Delta}$ [mH]	0.11	0.11	0.11
$L_{q\Delta}$ [mH]	0.13	0.13	0.13

As one can notice, in the operating points of interest, the inductances are quite equal each other; so the machine can be considered isotropic magnetically.

In order to understand how the efficiency varies with the mechanical speed, several simulations have been performed in the range speed 1500 [rpm]÷15000 [rpm] (fig. 56). In this case, the operating temperature has been set equal to 120 [°C] and the torque has been set equal to 0.3 [Nm], as said before.
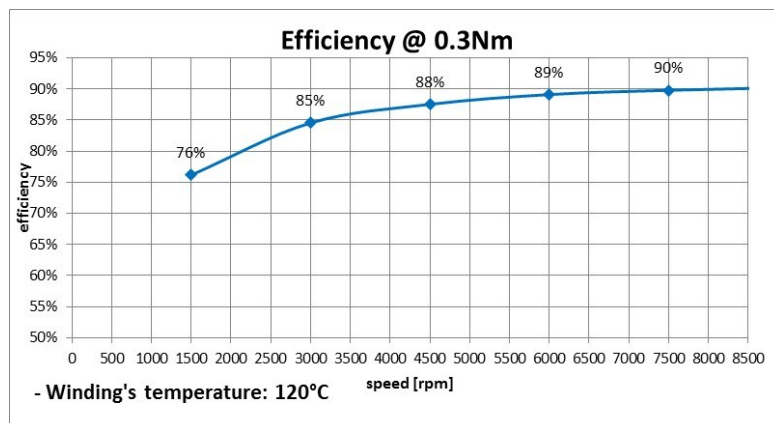

fig. 56: Efficiency vs. mechanical speed obtained by FEM simulations

From fig. 56, one can notice the efficiency value, which reaches the 90% when the speed is equal to 7500 [rpm].

In the end, to complete the analysis of the machine, thermal simulations have been pursued, in order to understand how much is the thermal power to be disposed by the prototype. In nominal conditions, the fuel goes through the airgap; since the fuel has a constant temperature and it is equal to about 20 [°C] (in the most cases), it is possible to suppose that the rotor has a constant temperature, equal to fuel temperature. The results of the thermal simulations have been shown in fig. 57 and fig. 58. In particular, the temperature of the different parts of the machine are highlighted. The thermal simulations have been carried out for 2700 [rpm] and 8500 [rpm] cases, respectively.
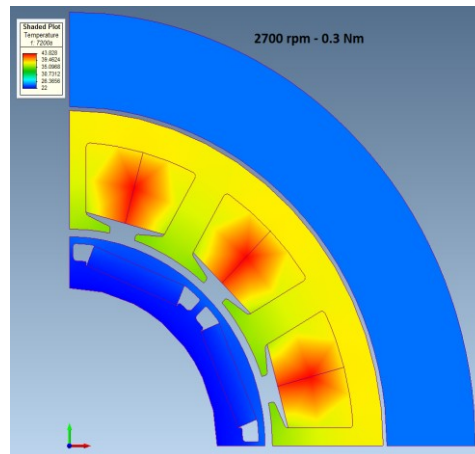
fig. 57: Temperature gradients for a speed equal to 2700 [rpm] and torque 0.3 [Nm]
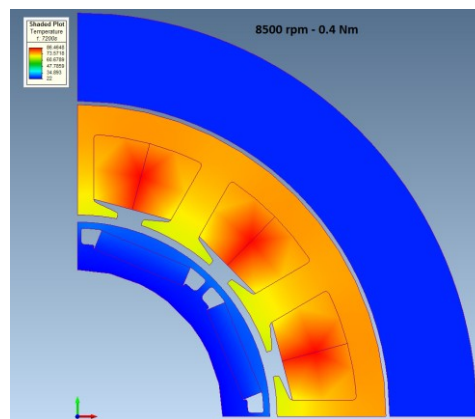
fig. 58: Temperature gradients for a speed equal to 8500 [rpm] and torque 0.4 [Nm]

To carry out the thermal simulations, the following conditions have been set:

➢ Heat exchange between box and room air through natural convection;

➢ Convection coefficient equal to 10 [W/m^2 $^\circ$C];

➢ Temperature room air constant and equal to 20 [°C].

From fig. 57 and fig. 58, one can notice the box, which contains the electrical machine (it is at the top part of the machine); the box is made up of aluminium and considering the temperature gradients, the box is not subjected to overheating.

2.3. Test-Bench: measurements performed on the prototype

In fig. 59 is shown the test-bench realized. Thanks to test-bench, it is possible to test the electrical machines realized. In particular, the prototypes does not have standard dimensions; because of that, it is necessary to adapt the machine to standard flanges (in this case IEC 63), in order to attach the machines themselves to the test-bench, which is designed for standard flanges.
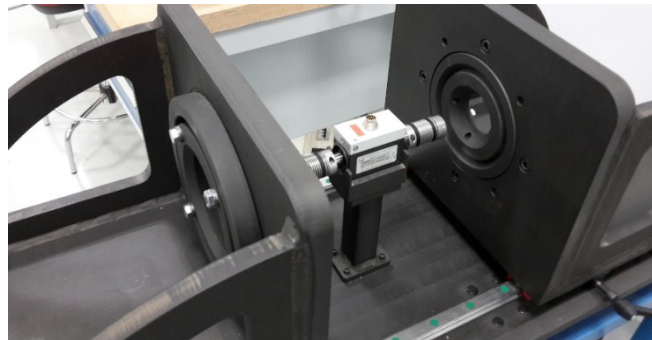
fig. 59: Test-bench

fig. 60: Flanges IEC 63, bearings, shaft, rotor

fig. 61: Complete motor support used to carry out the tests

In fig. 60 and fig. 61 the different mechanical parts, used to assemble the motors and attach them to the test-bench, are shown.

The room between the stator and the inner part of the IEC 63 flange has been filled by a bushing in aluminium. The aluminium is a good material for this purpose, because of its thermal conductivity; in fact, it is important to measure the temperature of the machine during the tests.

As said by standard IEEE 1812-2014, the back-to-back configuration is the configuration test to be used for the characterization of the permanent magnet machines (fig. 62). In this configuration, there are two motors, which are equal to each other (PM1 and PM2); also the drives must be equal to each other. There is only a DC power supply. At steady-state, the power delivered by DC power supply is equal to the sum of the losses of the two motors and drives.
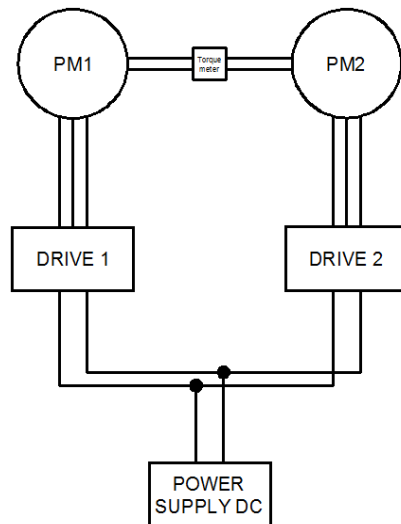
fig. 62: Back-to-back configuration test

In this work, the drives used were different, according to the type of measurements to be done. In particular, for inductances and inertia measurements, DSpace has been used; while, for the other tests, two equal commercial powerboxes have been used, in order to control a machine in current mode and the other one in speed mode.

2.3.1. Back-EMF measurements

The back-EMF measurements consist in driving the test machine (in this case PM2) until a certain speed; the terminals of the test machine must be open, because the currents can flow along the legs of the inverter thanks to the diodes, making the measurements not suitable. The configuration test is shown in (fig. 63) [13]:
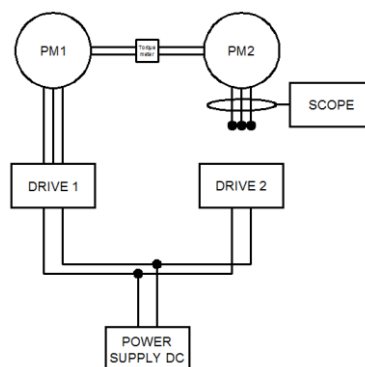
fig. 63: Back-EMF measurement setup

As shown in fig. 63, the PM2 machine is not connected to the inverter; the back-EMF is measured by an oscilloscope (fig. 64).
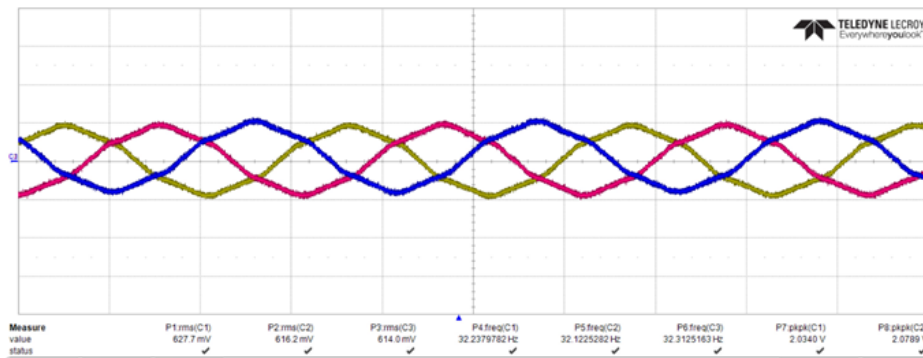
fig. 64: Back-EMF measurements

At 480 [rpm], the root mean square value of the back-EMF is equal to 620 [mV]; in addition, the waveforms are symmetric and balanced; that is, neither misalignment between rotor and stator nor stator winding faults are present. The FEM simulations (pursued at 480 [rpm]) are shown in fig. 65:
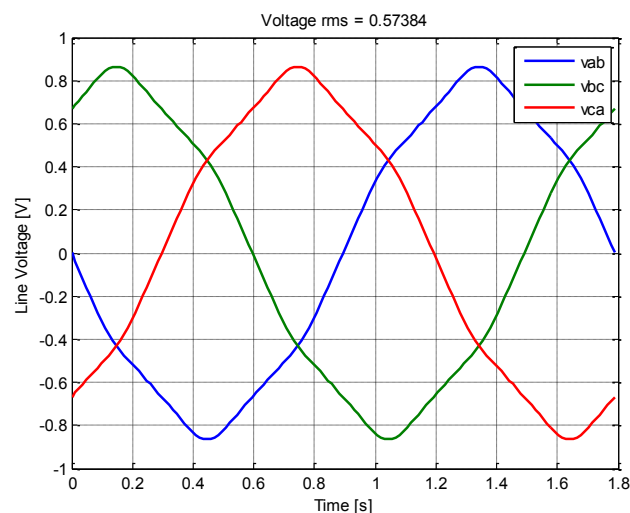
fig. 65: Back-EMF given by FEM simulations

As one can notice, the waveforms measured and estimated by FEM are coherent; in addition, the real back-EMF has a root mean square value higher than estimated one.

Doing the measurements for different speeds, it is possible to estimate the electro-motive force constant K_e. The measurements of the K_e constant is referred to a star winding connection, for a machine with two poles (this for control purposes).

Table 21: BACK-EMF MEASUREMENTS

Speed [rpm]	Voltage [V]
500	0.3351
1000	0.6773
1500	1.02
2000	1.3608
2500	1.7038
3000	2.05
3500	2.4
4000	2.74
4500	3.1
5000	3.4

The electro-motive force is given by the slope of the following straight line:
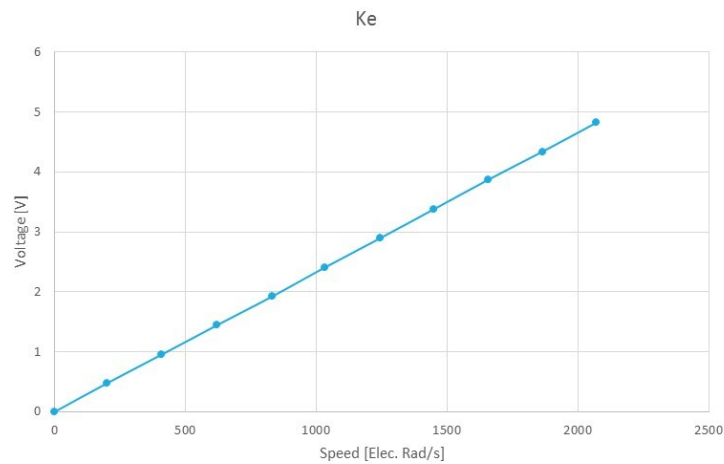
fig. 66: Back-EMF vs. speed (obtained from Table 21)

The slope is equal to 0.0023 [Vs/rad$_{ele}$]; this value is also equal to the permanent magnets flux linked to the stator windings.

2.3.2. Phase resistance measurements

The resistance measurement has been performed by using the surge-test device (fig. 67). Thanks to this device, it is possible to measure the stator winding resistance using the 4-wire method; in this way, the measurement does not contain the resistance of the wires, used to connect the motor to the device. In addition, it is possible to test the insulation resistance, in order to investigate on the possibility of stator winding faults. The measurements are referred automatically to 20 [°C], thanks to a temperature probe, which is used during the test session [13].

fig. 67: Surge-test device

The experimental results are:

Summary		
Resist.nomin. 1-2	24.88 mOhm (20.0°C), Temperatura ambiente=23.4°C	*Tested*
Resist.nomin. 2-3	24.90 mOhm (20.0°C), Temperatura ambiente=23.4°C	*Tested*
Resist.nomin. 3-1	24.81 mOhm (20.0°C), Temperatura ambiente=23.4°C	*Tested*
Resistenza d'isolamento	506.1V, >100.000 GOhm, Imax1=1.775µA, Imax2=1.390µA, DAR= -, PI= -	*Tested*

fig. 68: Report generated by surge-test device

From the experimental data, it results that the phase resistance is equal to 12.5 [mΩ] (it is referred to a star connected winding). Instead, the insulation resistance is equal to 100 [GΩ]; that is, there are not faults in the stator winding.

2.3.3. Inductance measurements

For the inductance measurements, different methods could be used; some are mentioned in the standard IEEE 1812-2014; others can be found in scientific literature.

In this work the methods used are:

➢ Stand-still;

➢ Slip-test;

➢ Magnetic identification.

In the case of stand-still measurements, it is needed to align the rotor along the A-phase axis (fig. 69). So, for the L_d measurement, the d-axis is aligned along the A-axis; instead, for the L_q measurement, it is necessary to align the q-axis along the A-axis. The value of the inductances are given by eq. 75:

$$L_{d/q} = \frac{V \sin \varphi}{\omega_e I}$$
eq. 75

Where:

➢ ω_e is the electrical pulsation;

➢ V e I are the rms phase voltage and current;

➢ φ is the displacement between the voltage and the current.

To do the measurements, it is necessary to use an AC power supply. The voltage is applied to the A-phase and B-C phases, which are short-circuited each other [13] [15].
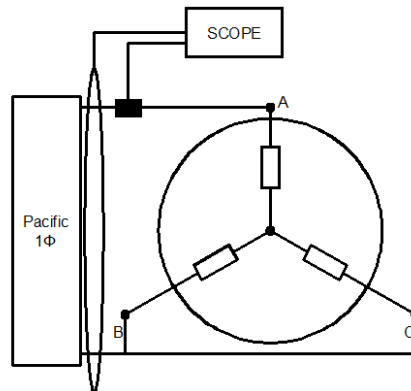
fig. 69: Stand-still setup

Instead, for slip-test, it is needed to drive the rotor up to steady-state, until a constant speed value; meanwhile, the motor under test must be powered by an AC power supply, using a frequency equal to ten times (at least) the electrical frequency of the back-EMF induced in the machine under test. The test configuration is shown in fig. 70:
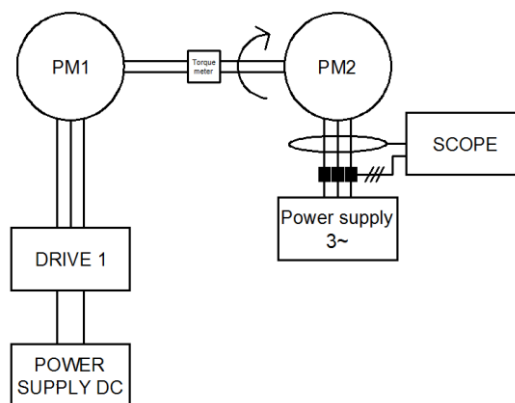
fig. 70: Slip-test setup

During the test, the voltage phasor will rotate along a circumference, because of the power supply, which delivers a constant voltage; while, the current phasor will rotate along an ellipse, because of the anisotropy of the machine. In order to perform correctly this measurement, it is necessary to remember that the back-EMF must be removed from the measurements of the voltages, because it can be considered as offset.
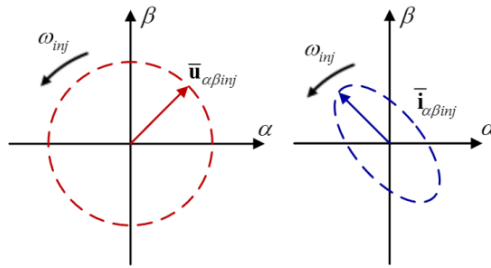
fig. 71: Voltages and currents locus when using high frequency voltages

The inductance L_d will be given by the ratio between major axis current locus and the voltage; the same thing for L_q, but considering the minor axis current locus [15].
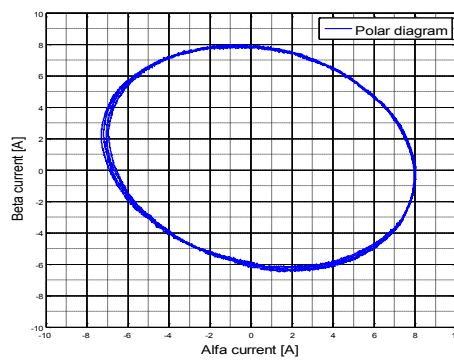
fig. 72: Measured current locus

In the end, the last method (magnetic identification) is present only in scientific literature, the reference is [16]. To carry out the measurements, it is necessary to use DSpace board (only for a rapid execution of the test). The main goal is the identification of the magnetic model of the machine, calculating the d-axis and q-axis flux for all the operating points; the electromagnetic model of a generic electrical machine is (eq. 76):

$$\begin{cases} \lambda_d = f(id, iq) \\ \lambda_q = f(id, iq) \end{cases} \qquad \text{eq. 76}$$

In order to calculate fluxes, it is necessary that the following hypotheses be satisfied:

1. The test machine must be driven at a constant speed by a second machine; the speed is measured by an encoder;

2. The test machine is vector current controlled;

3. The PWM voltages must be measured or accurately estimated;

4. The stator resistance voltage drop must be compensated;

5. In the case of PM machines, all tests must be at the same operating temperature;

6. The effect of iron loss must be negligible.

The current value chosen can be represented in the dq system reference like in fig. 73:

fig. 73: dq current mesh for electromagnetic model identification process

In order to neglect the iron losses during the test, it is needed to choose the speed equal to 1/3 of the nominal speed; meanwhile, to avoid the overheating, it is needed to pursue the tests rapidly, making a break between two points of the mesh. At last, to compensate the stator resistance voltage drop, the test machine must be driven by positive (motoring operation) and negative (breaking operation) i_q current values. A typical mesh used for this purpose is shown in fig. 73.
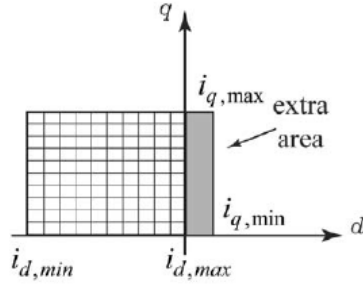
The negative i_d current values represent the weak flux operating points; meanwhile, the positive i_d current values represent the transient operating points (grey part of mesh in fig. 73).
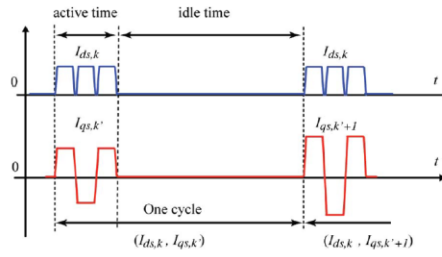
fig. 74: i_q and i_d references over the time, used for the identification of the electromagnetic model of the machine

So, at steady-state conditions, the d-flux and the q-flux are given by (eq. 77-eq. 78):

$$\lambda_d = \frac{1}{2}\left(\frac{v_{q,1} + v_{q,3}}{2} + v_{q,2}\right)\frac{1}{\omega_e} \qquad \text{eq. 77}$$

$$\lambda_q = -\frac{1}{2}\left(\frac{v_{d,1} + v_{d,3}}{2} - v_{d,2}\right)\frac{1}{\omega_e} \qquad \text{eq. 78}$$

where $v_{q,1}$, $v_{q,3}$, $v_{d,1}$ e $v_{d,3}$ are the voltages supplied during the motoring operation; while $v_{q,2}$ e $v_{d,2}$ are the voltages supplied during the breaking operation. The third impulse is put to avoid the resistance modifies its value, during a positive and a negative i_q impulse. A mention is necessary for the voltages; in fact, it is possible to use the reference values, thanks to the fact that the non-linear effects of the inverter are compensated. In this way, it is possible to simplify the identification process.
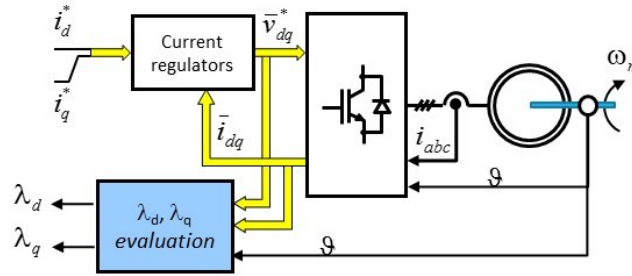
fig. 75: Electromagnetic identification setup

Using the three different methods, the inductance values are:

Table 22: INDUCTANCE MEASUREMENTS RESULTS

Method	L_d	L_q
Standstill	46 [μH]	57 [μH]
Slip Test	45 [μH]	57 [μH]
Magnetic model identification	61 [μH]	72 [μH]

2.3.4. Inertia measurement

In this paragraph is analyzed the method to identify the inertia momentum (J) and the viscous friction coefficient (B). The identification process takes place using DSpace system. To estimate B, it is necessary to estimate the iron losses at no load, because of the presence of permanent magnets. To estimate the iron losses at no load, FEM simulations have been used. In particular, Infolytica MotorSolve software has been used. Thanks to FEM simulations, the relation between iron losses and speed is calculated (fig. 76).
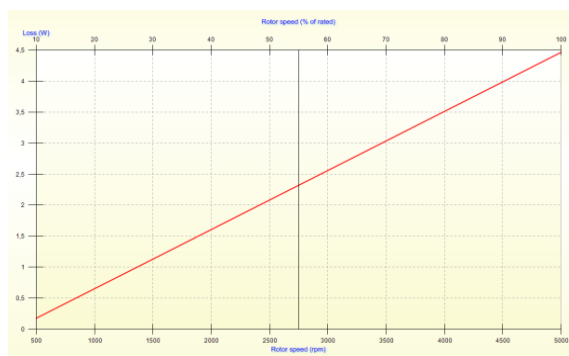
fig. 76: Iron losses vs. speed estimated by FEM simulations

The B value is given by reducing the shaft power (given by the product between the shaft torque and speed) from the iron losses at each speed reached. The machine under test must be driven by a second machine.
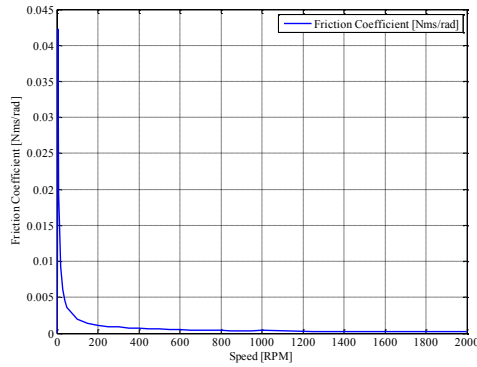
fig. 77: B vs. speed

As one can notice, at low speeds, the B value has an higher value than the values obtained from 1000 [rpm] up to 2000 [rpm]. This is due to noise, which affects the torque measurements at low speeds. For this reason, to carry out the B calculation, the speeds considered are from 1000 [rpm] until 2000 [rpm] [17]. Another method used to estimate the B value consists of using a dummy-rotor (that is, a rotor without magnets). In this case, the shaft power is equal to the friction losses themselves [13].

To estimate the inertia momentum, it is needed to accelerate and decelerate the machine, using a shaft torque waveform similar to that shown in fig. 78 [17]:
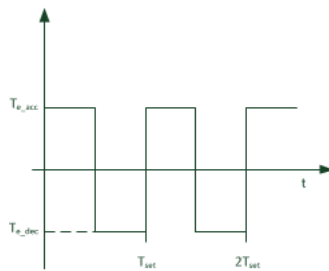
fig. 78: Torque waveform to be used to estimate the inertia momentum

Consequently, the speed will have the waveform shown in fig. 79:
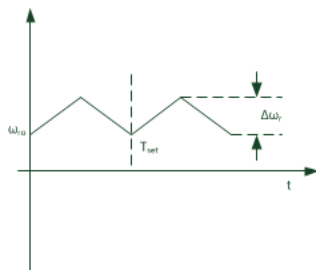
fig. 79: Speed waveform due to torque waveform shown in fig. 78

Carrying out the experimental tests, it is possible to measure the speed by using the encoder. The real waveform of speed is reported in fig. 80:
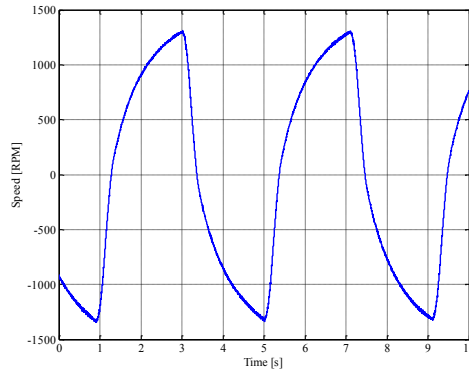
fig. 80: Speed waveform measured by the encoder on the test machine (measurements in [rpm])

Knowing the period of the acceleration waveform, it is possible to estimate the inertia momentum, using the eq. 79:

$$J = \frac{\left(\dfrac{\frac{T_{acc}-B\omega}{\Delta\omega}}{\frac{T}{2}} - \dfrac{\frac{T_{dec}-B\omega}{\Delta\omega}}{\frac{T}{2}}\right)}{2}$$

eq. 79
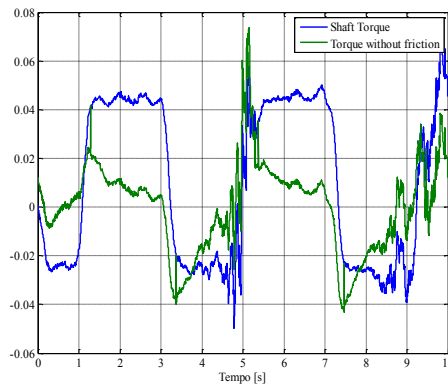
fig. 81: Shaft torque and shaft torque without friction losses

Concluding, the mechanical parameters values obtained are:

Table 23: MECHANICAL PARAMETERS

Parameter	Value
J	1.12e-4 [Nms2/rad]
B	2J [Nms/rad]
k_T	0.0145 [Nm/A]

From Table 23, one can notice the k_T factor, which is the torque constant of the machine. This value has been estimated during the tests.

2.4. Mechanical losses estimation

In this paragraph, the main purpose is the calculation of the mechanical losses, which affect the performance of the prototypes analysed; this is accomplished in order to use them in the calculation of the efficiency. In order to replicate the measurements in different labs, two commercial powerboxes are used.

The losses at no load of an electrical machine equipped with permanent magnets, are equal to the sum of iron losses and friction/ventilation losses [13]. Such losses depend on the speed of the machine and the operating temperature. In fact, because of the temperature, the followings harmful effects arise:

➢   Variation of the iron losses (because the PM remanence depends on the temperature);

➢   Increasing of the friction and the ventilation losses (because of the mechanical dilation of the bearings).

Since the permanent magnets cannot be turned off, in order to estimate the friction and ventilation losses, one can think of:

➢   Using a rotor, with the permanent magnets to be magnetized;

➢   Using a rotor, with the permanent magnets replaced with a non magnetic material, which has the same density of the permanent magnets;

➢   Using a dummy rotor, which has the same weight of the rotor to be replaced.

After the machine is equipped with the dummy rotor, it is needed to drive the machine under test up to a constant speed by using a second motor. Since the test-bench is equipped with a torque meter, it is possible to measure the total mechanical losses. The relation to be used is (eq. 80):

$$P_{FW} = T_{Fw} \cdot \omega_m \qquad\qquad \text{eq. 80}$$

If the rotor is magnetized, to carry out the measurements, it is needed to estimate the iron losses at no load. To accomplish that, FEM simulations can be used. In fact, as said, FEM simulations permit to estimate the iron losses at a given speed at no load (fig. 76). In this case the relation to be used is (eq. 81):

$$P_{FW} = T_{Fw} \cdot \omega_m - P_{FE\_Estimated} \qquad\qquad \text{eq. 81}$$

To measure the mechanical losses, the test-bench must have the configuration shown in fig. 82 [13]:
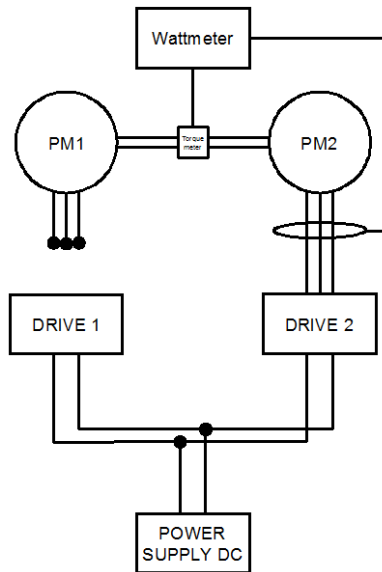
fig. 82: Mechanical losses estimation setup

fig. 83: Dummy rotor in stainless steel, used to estimate the mechanical losses

The speeds considered to estimate the mechanical losses vary from 500 [rpm] up to 4000 [rpm], using a discrete step of 500 [rpm]. The results are in Table 24:

Table 24: MECHANICAL LOSSES

Speed [rpm]	PM1 [W]
478.4	0.91154
984.6	2.7307
1479	4.7172
1976	6.9357
2468	9.1618
2966	10.976
3454	13.24
3950	15.1

The measurements have been realized using the dummy rotor. As one can notice, the speeds reported in Table 24 are not multiple of 500 [rpm]; the reason is in the real rotational speed. In fact, the reference speed is set using an analog signal. The analog signal comes from a DC power supply; not being sure if the analog signal is correctly conditioned, it has been necessary to calculate the mechanical speed from the electrical frequency of the currents measured from the motor, which drives the machine under test. Finally, the temperature measured on surface of the bushing of the machine under test was constant and equal to 28 [°C] during the tests execution.

Replicating the same measurements for a machine with a magnetized rotor, it is possible to estimate the iron losses, and compare them with the losses estimated by FEM simulations.
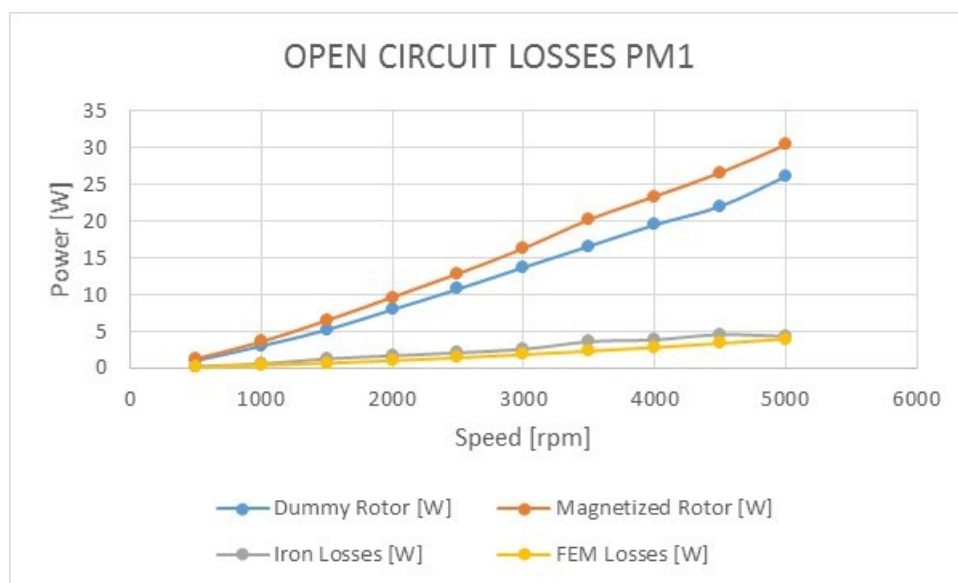
fig. 84: Open circuit losses PM1

In fig. 84 the acronyms have the following meanings:

➢ *Dummy Rotor*: Friction and ventilation losses;

➢ *Magnetized Rotor*: Friction and ventilation losses + Iron losses;

➢ *Iron Losses*: Iron losses calculated by experimental tests;

➢ *FEM Losses*: Iron losses calculated by FEM simulations, for all the speeds considered in the tests.

In particular, the FEM simulations consider only the stator iron losses, because at no load the airgap flux density moves synchronously with the rotor. Although there are small differences in the mechanical speed values measured during the tests with dummy rotor and the magnetized rotor, the considerations about the losses are made considering the reference speeds, in order to make easier the understanding of the results.

2.5. Efficiency tests

Using the back-to-back configuration (as described by IEEE 1812-2014) shown in fig. 85, the efficiency of the machines has been measured. In particular the efficiency measurements have been carried out for the following shaft torque:

➤ 0.1 [Nm];

➤ 0.2 [Nm].

The PM1 machine is vector speed controlled, while the PM2 machine is vector current controlled. The speed value used to carry out the experimental tests has been set equal to 2700 [rpm]; in particular, the efficiency calculation has been performed only for PM1 machine.
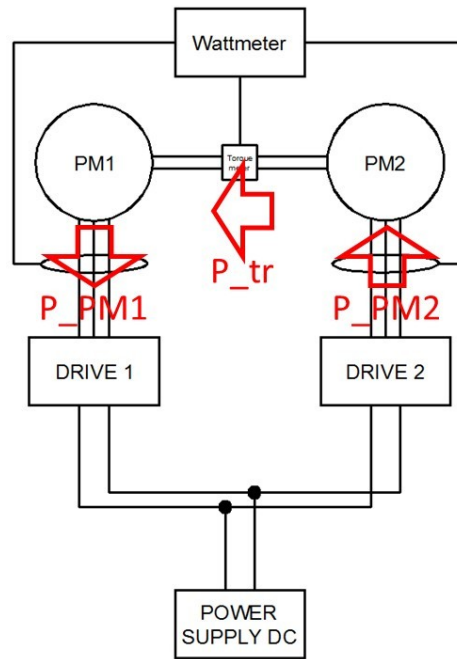
fig. 85: Efficiency measurements setup with power flows highlighted

Since the speed considered is equal 2700 [rpm], the friction and ventilation losses are equal to 11.3 [W]; therefore, the torque due to the friction and ventilation is equal to 0.04 [Nm]. For comparison purposes, the experimental data have been compared with the FEM simulations, using the same line current measured during the efficiency tests. The electromagnetic torque and the efficiency are calculated from the experimental data using the relations stated in eq. 82:

$$P_{PM1} = From\ wattmeter$$
$$Losses_{PM1} = P_{transmitted} - P_{PM1} - P_{FW\_PM1}$$
$$T_{PM1} = T_{transmitted} - T_{FW\_PM1} \qquad eq.\ 82$$
$$\eta_{PM1} = \frac{T_{PM1}\omega_m}{T_{PM1}\omega_m + Losses_{PM1}}$$

Where:

➢   Losses$_{PM1}$ are total losses of the PM1 machine;

➢   T$_{PM1}$ is the electromagnetic torque of the PM1 machine.

The eq. 82 becomes clear, if one observes the fig. 85, where power fluxes are highlighted.

To distinguish the experimental tests done, the shaft torque value has been used as reference.

➢   Shaft torque equal to 0.1 [Nm]

Table 25: EFFICIENCY STUDY - 0.1 [NM] CASE

	Experimental	FEM
Torque [Nm]	0.06	0.05
P_PM1	14.6	16.4
Losses [W]	2.37	2.15
Eff. [%]	87.72	87
RMS Voltage [V]	3.26	3.6
RMS Current [A]	2.64	2.64

➢   Shaft torque equal to 0.2 [Nm]

Table 26: EFFICIENCY STUDY - 0.2 [NM] CASE

	Experimental	FEM
Torque [Nm]	0.16	0.161
P_PM1	36.13	49.9
Losses [W]	9.12	4.28
Eff. [%]	83.22	91.4
RMS Voltage [V]	2.91	3.78
RMS Current [A]	7.5	7.5

From results shown in Table 25 and Table 26, one can notice that in the case of shaft torque equal to 0.1 [Nm], the experimental results and FEM ones agree. An abnormal behaviour happens when the shaft torque equals to 0.2 [Nm]; in fact, the real power delivered by PM1 is lower than FEM estimation; so, in the real case, the losses of the electrical machine are higher than estimated ones; but, the electromagnetic torque is equal to FEM estimation.

Concluding, the experimental data obtained from the prototype are in good accordance with the theoretical ones; in fact, the torque measured and the torque estimated by FEM are equal.

The only discordant point is about the inductance values; in fact, inductance values estimated by FEM simulations are slightly lower than values obtained by experimental method.

This is highlighted by the Table 27:

Table 27: INDUCTANCE VALUES COMPARISONS

Method	L_d	L_q
Standstill	46 [µH]	57 [µH]
Slip Test	45 [µH]	57 [µH]
Magnetic model identification	61 [µH]	72 [µH]
FEM simulations	36 [µH]	43 [µH]

From Table 27 can be stated that the best way to estimate the inductance is in using experimental methods.

CHAPTER III

3. Sensorless control introduction

Permanent magnet synchronous motors are widely used in variable frequency drives; moreover, due to the presence of permanent magnets, it is possible to produce machines with high power density; particularly advantageous in all the applications where the size of the machine is an issue.

Permanent magnet machines are driven in almost all applications by vector speed control. In order to have a uniform profile of speed, it is needed to know the rotor position at any instant of time; i.e. from the standstill state until the steady-state. In order to obtain the rotor position, it is possible to use a special sensor, such as an encoder, or a resolver. However, the presence of these components has certain disadvantages, such as hardware complexity, increased costs, reduced cable and sensor reliability, electromagnetic noise, and nevertheless increasing the inertia momentum of the machine itself [18]. For the reasons listed above, it is desirable to use a sensorless control, i.e. a vector control, which does not use a position sensor.

Sensorless control algorithms are particularly sensitive to the following problems:

➢ Timing of microcontroller;

➢ Uncertainty on machine parameters;

➢ Mismatch between real voltages and reference voltages.

Concerning the timing of microcontroller, this causes a bad estimation of the rotor position; in fact, in order to estimate correctly the rotor position, it is necessary to know the voltage and the current supplied to the motor at the same time instant. This is not possible because of the timing of microcontroller; the problem can be solved by entering delays within the control, in such a way there is a match between a sample of the phase current and the corresponding reference voltage; in other words, it is necessary to synchronize the control with the sampling process. It is mandatory to say that this problem becomes very important when the ratio between sampling frequency and the electrical frequency is lower than 10, at very high rotational speed.

Concerning the inverter, non-linearities come from:

➢ dead-time;

➢ ohmic nature of switches;

➢ other side-effects inside the inverter.

To take into account the non-linear nature of the inverter, the electrical model of the inverter must be obtained. Once this model is obtained, the control must be able to face these additional negative effects.

This chapter shows the sensorless control algorithm used for starting and controlling the prototype shown and described in chapter II.

Concerning the control algorithms, in the industrial field, the most used sensorless algorithms are:

➢ Model based;

➢ Saliency tracking;

➢ IF control.

Model-based control can track the rotor position using the electromagnetic machine model; however, these algorithms suffer at low speeds, where rotor information is too low to be processed by estimation algorithms [18]. At zero speed or at low speeds, it is preferable to use saliency tracking or starting the machine via IF (Current - Frequency) control. So, a combination between these control algorithms is used in order to improve the performance.

3.1. IPMSM Model
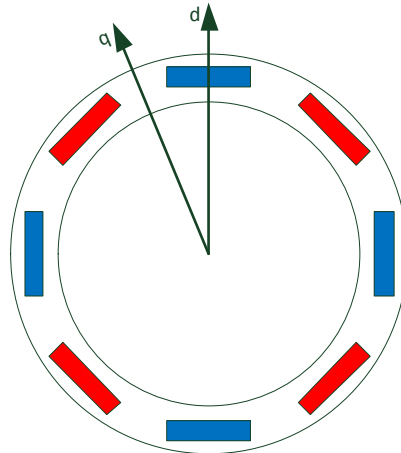
fig. 86: Rotor of the motor under test

In fig. 86 there is the rotor used by the prototype analyzed. The rotor has four pole pairs. The d-axis coincides with the magnetic north pole axis.

The electromagnetic model of the IPM machine in dq coordinates is:

$$v_{sd} = R_s i_{sd} + L_{sd} \frac{di_{sd}}{dt} - \omega_r L_{sq} i_{sq} \qquad \text{eq. 83}$$

$$v_{sq} = R_s i_{sq} + L_{sq} \frac{di_{sq}}{dt} + \omega_r L_{sd} i_{sd} + \omega_r \psi_{PM} \qquad \text{eq. 84}$$

$$T_m = \frac{3}{2} \frac{P}{2} \{ (L_{sd} - L_{sq}) i_{sd} i_{sq} + \psi_{PM} i_{sq} \} \qquad \text{eq. 85}$$

On the basis of eq. 83 and eq. 84, it is possible to draw the electrical circuits shown in fig. 87, where L_{sd} is the d-axis inductance (that is, the sum of the L_{ls} and L_{md} in fig. 87), L_{sq} is the q-axis inductance (that is, the sum of L_{ls} and L_{mq} in fig. 87) and Ψ_{PM} is the flux due to the permanent magnets; P is the number of poles.

fig. 87: d-axis and q-axis circuits

Another useful representation of the electromagnetic model of the machine is in the αβ reference system. Such representation is used to estimate the rotor position. The mathematical model in αβ coordinates of the machine in use is (eq. 86):

$$v_{s\alpha\beta} = R_{s\alpha\beta}\bar{i}_{s\alpha\beta} + \frac{dL_{s\alpha\beta}}{dt}\bar{i}_{s\alpha\beta} + L_{s\alpha\beta}\frac{d\bar{i}_{s\alpha\beta}}{dt} + \frac{d\bar{\Lambda}_{PM\alpha\beta}}{dt}$$
eq. 86

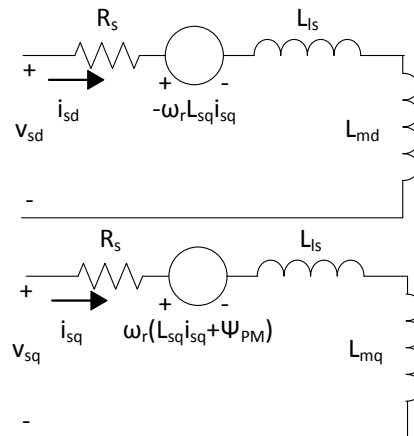where $\Lambda_{PM\alpha\beta}$ is the vector of the flux due to the permanent magnets, while $L_{s\alpha\beta}$ is a 2x2 matrix, which has the structure stated in eq. **87** [18]:

$$\begin{bmatrix} L + \Delta L \cos(2\theta_r) & -\Delta L \sin(2\theta_r) \\ -\Delta L \sin(2\theta_r) & L - \Delta L \cos(2\theta_r) \end{bmatrix}$$
eq. 87

where

$$L = \frac{L_{sq} + L_{sd}}{2}, \Delta L = \frac{L_{sq} - L_{sd}}{2}$$
eq. 88

3.2. Model-based control

The rotor position can be estimated by using an open-loop structure observer. The open-loop observer is based on the electromagnetic model of the machine; in particular, in this work, the sensorless control, using the model-based estimation process, is called more simply MB control. The observer structure is shown in figure below:
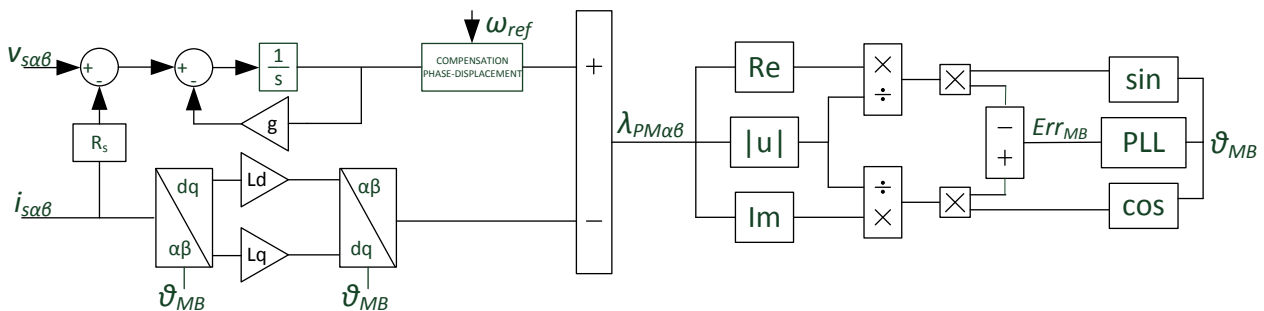

fig. 88: Model-based estimation process

The PLL used inside the model-based estimation process is shown in fig. 89 (in the estimation process, the scheme until the PLL is called model-based observer, from here on):
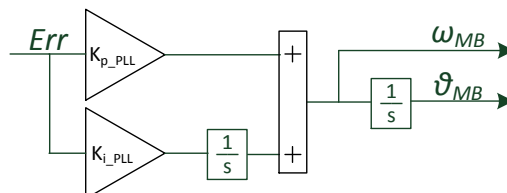

fig. 89: PLL structure used inside the model-based observer

The permanent magnets flux is estimated by means of eq. 89:

$$\lambda_{PM\alpha\beta} = \int_0^t (V_{\alpha\beta} - R_s i_{\alpha\beta})d\tau - L_{\alpha\beta}i_{\alpha\beta} \qquad \text{eq. 89}$$

In the Laplace domain, the eq. 89 becomes:

$$\begin{cases} \lambda_{PM\alpha} = \dfrac{1}{s}(v_{s\alpha} - R_s i_{s\alpha}) - L_{s\alpha}i_{s\alpha} \\ \lambda_{PM\beta} = \dfrac{1}{s}(v_{s\beta} - R_s i_{s\beta}) - L_{s\beta}i_{s\beta} \end{cases} \qquad \text{eq. 90}$$

Instead of using a pure integrator to estimate the permanent magnets flux, a low pass filter is used. In fact, the g parameter inside the estimation scheme works in such a way that the drift of integrator is avoided. The drift of the integrator is due to offsets, which affect the current measurements. It could be proved that the steady-state error due to the offsets is given by eq. 91:

$$\lim_{t\to\infty}\lambda_{r0} = \frac{1}{g}(V_{s0} - R_s i_{s0}) \qquad \text{eq. 91}$$

V_{s0} e i_{s0} represent constant terms related to voltages and currents. If g is equal to zero, the error would be infinite, bringing the angle estimated toward the infinite; so, it would become unuseful. Generally speaking, g has a value between 20 [rad/s] and 100 [rad/s], and from fig. 90, one can notice how the transfer function of the pure integrator is modified (that is, it is the same of a low-pass filter, where the cut-off frequency varies with the g value) [17] [18].
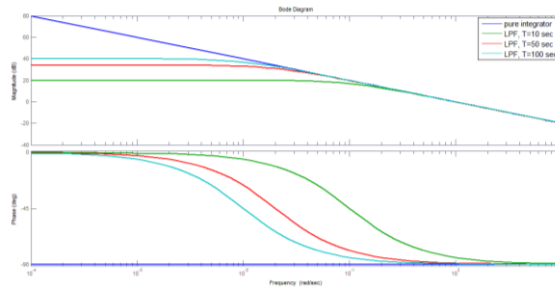
fig. 90: Comparisons between the transfer function of the pure integrator and the transfer function of the low-pass filter for different cut-off frequencies

Inside the estimation algorithm of the rotor position, a compensation of the displacement given by the low-pass filter is introduced. The compensation has the expression stated in eq. 92:

$$\varepsilon_{compensation\ displacement} = 90° - \tan^{-1}\frac{\omega}{g} \qquad \text{eq. 92}$$

where ω represents the electrical speed of the motor; because of the noise, which affects the estimated speed, the compensation is carried out using the reference speed; in particular, the compensation can be carried out either after the integrator or at the output of the PLL, directly on the estimated angle, denoted by ϑ_{MB} in fig. 88.

It is preferable to use a PLL to estimate the rotor position (ϑ_{MB}), how the fig. 89 shows, because it is able to overcome the problem due to the noise introduced by the phase currents measurements. In addition, the PLL is able to give in output the estimation of the rotor speed (ω_{MB}).

So, the αβ components of the rotor flux, obtained by means of eq. 90, are normalized and sent to the PLL. The error in input to the PLL is given by the expression stated in eq. 93:

$$Err_{MB} = \sin \vartheta_r \cos \vartheta_{MB} - \cos \vartheta_r \sin \vartheta_{MB} \qquad \text{eq. 93}$$

Where ϑ_r is the rotor angle; $\cos\vartheta_r$ is the normalized $\lambda_{PM\alpha}$ component of the rotor flux; $\sin\vartheta_r$ is the normalized $\lambda_{PM\beta}$ component of the rotor flux.

In addition, knowing the rotor flux components, it is possible to calculate the magnitude of the rotor flux itself; that is, the Ψ_{PM} value. At steady-state, if Ψ_{PM} value is equal to zero, it is for sure that the machine is not running.

It is important to mention the main rules adopted for tuning the PLL shown in fig. 89. In particular, the PLL used is second order type; consequently, the transfer function is [19]:

$$H_{PLL}(s) = \frac{k_{p\_PLL}s + k_{i\_PLL}}{s^2 + k_{p\_PLL}s + k_{i\_PLL}} = \frac{2\delta\omega_n s + \omega_n^2}{s^2 + 2\delta\omega_n s + \omega_n^2} \qquad \text{eq. 94}$$

The PLL parameters (k_{p_PLL} and k_{i_PLL}) are tuned using the rules stated in eq. 95 and eq. 96:

$$k_{p\_PLL} = \frac{9.2}{t_s} \qquad \text{eq. 95}$$

$$k_{i\_PLL} = \frac{9.2 \cdot 2.3}{t_s^2 \delta^2} \qquad \text{eq. 96}$$

where δ is the damping coefficient and t_s is the rise time; taking δ equal to 0.707, one can act on t_s value during the test sessions, in order to get the best performance from the PLL. Generally speaking, the most used values for t_s are in the range 0.02-0.05 [s]. These rules, to design the PLL, are valid only when the PLL works with quantities, whose magnitudes are equal to the unity [19]; that is, the error in input must have an expression as defined in eq. 93.

3.3. Saliency tracking control

At low speeds, it is not possible to use the model-based algorithm in order to track the rotor position; for this reason, it is better to use the saliency tracking control method (also called HF control). This method uses the magnetic anisotropy of the machine; that is, the difference, in reluctance terms, which exists between d-axis and q-axis. Even when the machine is magnetically isotropic (as in the case of the considered prototype), it is possible to adopt the HF control thanks to the saturation along the d-axis induced by PMs. Using the difference between the d- and q-axis inductances, the rotor position can be tracked, through high frequency currents and voltages, whose frequency is, at least, 5 times the fundamental one. Consequently, thanks to the heterodyning process, it is possible to extract the rotor position from the currents and voltages. When the injected quantities are the currents, the rotor position is obtained by processing the voltages. In most practical cases, the voltages are the injected quantities; consequently, the rotor information is obtained by processing the currents (because the currents are the only measured quantities). There are two types of injection methods:

1. Rotating;
2. Pulsating.

In the rotating method, the injected voltage vector rotates in the αβ reference system; while, in the pulsating method, the injected voltage vector is a sinusoid along the estimated d- or q-axis. In this work, only the first method has been used. The physical effect is explained using fig. 91:
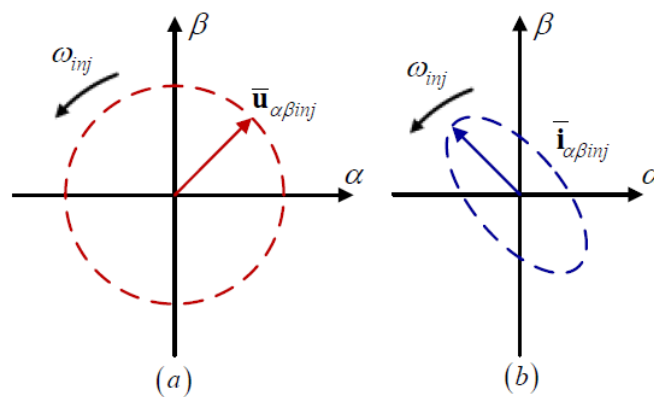
fig. 91: Injected voltages (a) and measured currents (b) loci

From fig. 91, one can notice the effect of the anisotropy on the measured currents, which describe an ellipse in the stationary system reference αβ; while the voltages describe a circular locus. The major axis of the ellipse (tracked by currents) corresponds to the d-axis, which represents the highest reluctance path [18].

Before introducing the heterodyning process, it is needed to describe the electromagnetic model of the machine, when high frequency voltages are injected.

The injected voltages have the expressions stated in eq. 97:

$$u_{si} = \begin{bmatrix} u_{s\alpha i} \\ u_{s\beta i} \end{bmatrix} = U_{si} \begin{bmatrix} \cos(\omega_i t) \\ \sin(\omega_i t) \end{bmatrix} \qquad \text{eq. 97}$$

where U_{si} is the magnitude of the injected voltages; such value is set by trial-and-error method, since it is not possible to know which is the current value more suitable to exasperate the anisotropy. In addition, the higher is the frequency, the higher must be the magnitude of the voltages injected, because of the impedance. The most frequently adopted frequencies are in the range 200 [Hz] ÷ 500 [Hz]. Before using the heterodyning process, it is useful to perform some preliminary tests under sensored vector control to check the actual HF current locus obtained. If the high frequency current locus is similar to that shown in fig. 91b, then the rotor position estimation is feasible by using the HF control. It is possible to derive the mathematical expression of the high frequency current locus (eq. 89):

$$\begin{bmatrix} i_{\alpha i} \\ i_{\beta i} \end{bmatrix} = \begin{bmatrix} I_{spi}\sin(\omega_i t) + I_{sni}\cos(2\vartheta_r - \omega_i t) \\ -I_{spi}\cos(\omega_i t) - I_{sni}\cos(2\vartheta_r - \omega_i t) \end{bmatrix} \qquad \text{eq. 98}$$

where I_{spi} is the positive high frequency stator phase current and I_{sni} is the negative high frequency stator phase current; the expressions of I_{spi} and I_{sni} are (eq. 99-eq. 100):

$$I_{spi} = \frac{U_{si}L}{\omega_i(L^2 - \Delta L^2)} \qquad \text{eq. 99}$$

$$I_{sni} = \frac{U_{si}\Delta L}{\omega_i(L^2 - \Delta L^2)} \qquad \text{eq. 100}$$

where L and ΔL have the same expressions stated before (eq. 88) [20] [21]; finally, ω_i is the frequency of the injected voltages. The rotor position (ϑ_r) information is inside the negative component of the current. In order to estimate the rotor position, it is needed to cut-off the high frequency content through a synchronous frame filter. The high frequency synchronous frame filter translates the frequency of the positive high frequency current to zero, that is, equal to direct current component pointed out by i_{sdqi} in fig. 92. The direct component of the current i_{sdqi} can be eliminated easily by a band-pass filter. The entire signal process diagram is shown in fig. 92.
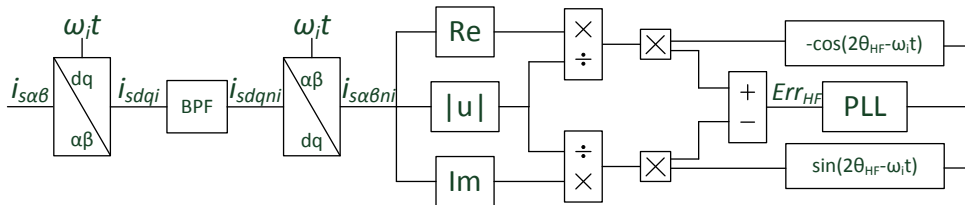

fig. 92: Heterodyning process

In the scheme of fig. 92, instead of using a band-pass filter (i.e. BPF), an high-pass filter (i.e. HPF) [20] can be used, but the band-pass filter increases the rejection to the noise. After the elimination of

the positive high frequency current, the current is again translated into the stationary reference system. From here, there is only the negative phase sequence current components, $Is_{\alpha ni}$ and $Is_{\beta ni}$. The components of the negative high frequency current are normalized and multiplied by $-\cos(2\vartheta_{HF}-\omega_i t)$ and $\sin(2\vartheta_{HF}-\omega_i t)$; in this way the error is calculated and sent to PLL, whose structure is similar to that shown in fig. 89. The expression of the error is (eq. 101):

$$Err_{HF} = -\frac{I_{s\alpha ni}}{\sqrt{I_{s\alpha ni}{}^2 + I_{s\beta ni}{}^2}} \cdot \cos(2\vartheta_{HF} - \omega_i t) - \frac{I_{s\beta ni}}{\sqrt{I_{s\alpha ni}{}^2 + I_{s\beta ni}{}^2}} \cdot \sin(2\vartheta_{HF} - \omega_i t) = \sin(2\Delta\vartheta_e) \qquad \text{eq. 101}$$

where ϑ_{HF} is the rotor angle estimated by the heterodyning process (the heterodyning process without PLL is called HF observer from here on).

Before using the saliency tracking method, the estimation of the magnetic polarity at standstill must be solved. For this purpose, the scheme shown in fig. 93 can be used:
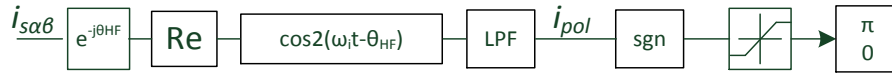

fig. 93: Magnetic polarity detection

In fig. 93, $i_{s\alpha\beta}$ are the high frequency currents in the stationary reference system. The sign of the current i_{pol} is necessary to estimate the magnetic polarity. There can happen two cases:

1.   positive i_{pol}: The estimated rotor angle and the real one are in opposition of π radians;

2.   negative i_{pol}: The estimated rotor angle is in the direction of the real one.

The magnetic polarity must be summed to the estimated angle ϑ_{HF} by the heterodyning process; after the standstill phase, the magnetic polarity estimation must be stopped in order to avoid the interference with the heterodyning process itself. In order to better understand the scheme of fig. 93, it is necessary to analyze the expression of the high frequency current. For this purpose, a new expression of the high frequency current is presented in eq. 102 [21]:

$$I_{s\alpha\beta} = \frac{V_c}{j2\omega_i}\left\{\left(\frac{1}{L_d}+\frac{1}{L_q}\right)e^{j\omega_i t} - \left(\frac{1}{L_d}-\frac{1}{L_q}\right)e^{-j(\omega_i t - 2\vartheta_{HF})}\right\} + \frac{V_c^2}{2\omega_c^2}\frac{d^2 i_d}{d\lambda_d^2}(\psi_{PM})\sin^2(\omega_i t - \vartheta_{HF})e^{j\vartheta_{HF}} \qquad \text{eq. 102}$$

Performing the operation shown in fig. 93, it is possible to obtain the expression of i_{pol} (eq. 103):

$$i_{pol} = -\frac{V_c^2}{8\omega_c^2}\frac{d^2 i_d}{d\lambda_d^2}(\psi_{PM})\cos 2(\vartheta_r - \vartheta_{HF})\cos(\vartheta_r - \vartheta_{HF}) \qquad \text{eq. 103}$$

So, when ϑ_r is equal to ϑ_{HF}, the i_{pol} has a negative value; the positive sign happens when there is a displacement of π between ϑ_r and ϑ_{HF}. In other words, if the estimated d-axis is along the real d-axis, i_{pol} is positive; on the contrary, when the estimated d-axis is in opposition with the real d-axis.

From fig. 94, it is evident how the magnetic polarity identification process works; in particular, when the stator flux and the magnet flux are in the same direction, the iron saturation is higher. This phenomenon can be detected using the high frequency current.
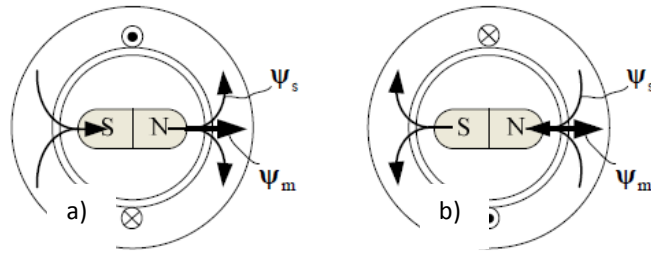
fig. 94: Physical explanation of the polarity magnet estimation; a) stator flux concordant to magnet flux; b) stator flux discordant to magnet flux

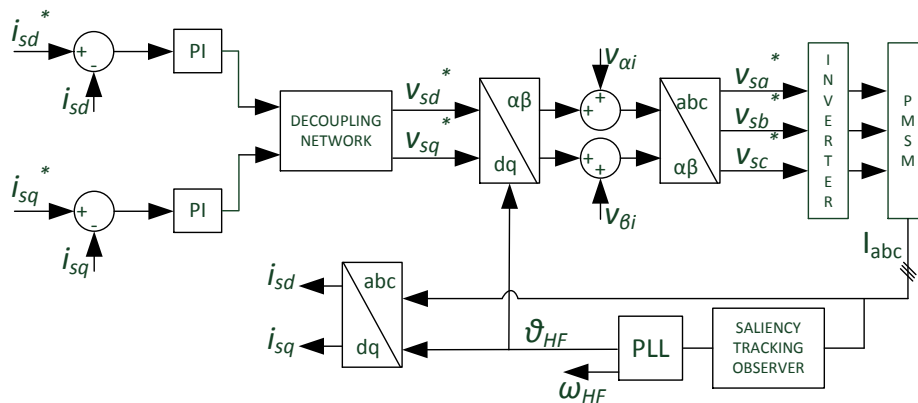fig. 95 shows the control scheme, when high frequency voltages are used for tracking the rotor position.

fig. 95: Control scheme when high frequency voltages are used

3.4. Hybrid control

In this paragraph the hybrid control is described. The control is said hybrid, since it uses the model-based control and the saliency-tracking control in two different phases. In particular, at standstill and in general at low speeds, the saliency-tracking control is on. When the speed becomes higher than a predetermined threshold, there is the switching to the model-based control. To simplify the transition from saliency-tracking to model-based control, a single PLL can be used (both observers, MB observer and HF observer, sent their errors to the single PLL). The single PLL is able to estimate the rotor position; in particular, the same PLL structure shown in fig. 89 has been used. The PLL can damp the transition, because of its own nature; for this reason, it is important to correctly tune the damping factor of the PLL. In this work, a damping factor δ equal to 0.707 has been used; the δ value chosen helps reducing the ripple in the estimation of the rotor position. The rise time must be tuned in such a way that the bandwidth is not very large, in order to reduce the noise (it is important to remember that the lower is the PLL bandwidth, the slower will be the control). In this case, an optimum value for the bandwidth has been found in the range 100 [rad/s] ÷ 200 [rad/s].

From fig. 96, it is possible to take a look of the control scheme, when a single PLL is used. One error comes from the HF observer, (Err$_{HF}$, eq. 101), the other one comes from the MB observer (Err$_{MB}$, eq. 93). The two errors are summed by means of a weighted sum. In particular, the weights have values, which are in the range $0 \div 1$ and they depend on the reference speed values. At standstill the weight for Err$_{HF}$ is one, instead of the weight for Err$_{MB}$, which is zero; from standstill to the threshold speed, the weights vary in a linear way. When the threshold value is passed, the weight for Err$_{MB}$ becomes one, while Err$_{HF}$ is equal to zero. The same variation happens in a reverse way when there is a reduction in the speed value; so, when the speed of the machine is lower than the threshold, the control switches from MB to HF (the logic is shown in fig. 96).
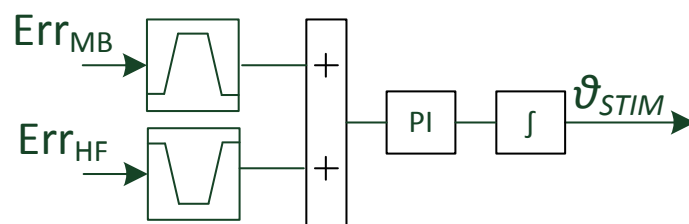

fig. 96: Estimation process scheme when a single PLL is used

Concerning the estimation of the electrical speed, it is more suitable to use a special type of observer, called mechanical observer (or simply speed observer, for clarification purposes). This structure comes from the mechanical equation of the machine (2nd Newton law). The state variable model of the mechanical observer is (in eq. 104, L is the gain matrix) [17]:

$$\dot{\hat{x}} = A\hat{x} + Bu + L(y - C\hat{x}) \qquad \text{eq. 104}$$

$$\begin{bmatrix} \dot{\vartheta}_{MECHOBS} \\ \dot{\omega}_{stim} \\ T_L \end{bmatrix} = \begin{bmatrix} 0 & 1 & 0 \\ 0 & -\frac{\hat{B}}{\hat{J}} & -\frac{1}{\hat{J}} \\ 0 & 0 & 0 \end{bmatrix} \begin{bmatrix} \vartheta_{MECHOBS} \\ \omega_{stim} \\ T_L \end{bmatrix} + \begin{bmatrix} 0 \\ \frac{1}{\hat{J}} \\ 0 \end{bmatrix} T_e + \begin{bmatrix} l_1 \\ l_2 \\ l_3 \end{bmatrix} \left(\theta_{stim} - \begin{bmatrix} 1 & 0 & 0 \end{bmatrix} \begin{bmatrix} \vartheta_{MECHOBS} \\ \omega_{stim} \\ T_L \end{bmatrix} \right) \qquad \text{eq. 105}$$

Using the Laplace transform and making some simplifications, it is possible to build the Simulink model shown in fig. 97:
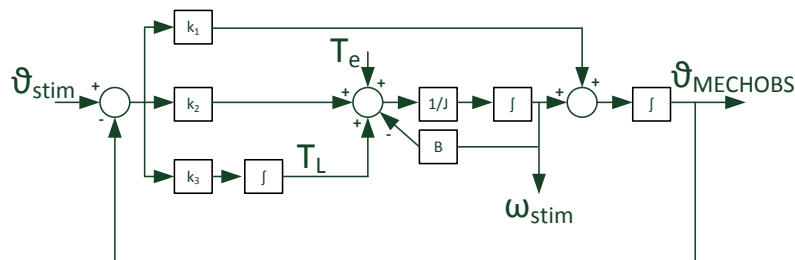

fig. 97: Mechanical observer in the Laplace domain

where it is possible to see that a PID regulator takes the place of the gain matrix L. In particular, the K_1, K_2 and K_3 parameters (which are the derivative, proportional and integral gains of the PID), have the expressions stated in eq. 106:

$$K_1 = l_1$$
$$K_2 = \hat{J} l_2$$
$$K_3 = -l_3$$

eq. 106

In fig. 97, ϑ_{stim} is the angle estimated by the PLL; $\vartheta_{MECHOBS}$ is the angle estimated by the mechanical observer and not used for transformation purposes; T_e is the electromagnetic torque, ω_{stim} is the speed estimated by the mechanical observer and used for speed control; finally, the mechanical observer is able to estimate the load torque (T_L).

Tuning a PID is very simple, because the rules are well-founded. In addition, the mechanical observer can be thought acting like a filter; so, using the rules used for the Butterworth filters, the first step is to set the damping factor equal to 0.5; instead, the bandwidth ω_n must be chosen by the operator and it must be smaller than the bandwidth used to estimate the rotor position. So, the rules, for the tuning the PID, are (eq. 107):

$$K_1 = 2\omega_n$$
$$K_2 = 2J\omega_n^2$$
$$K_3 = J\omega_n^3$$

eq. 107

In particular, in order to make easier the tuning procedure, the B value has been neglected. The total control scheme is shown in fig. 98:

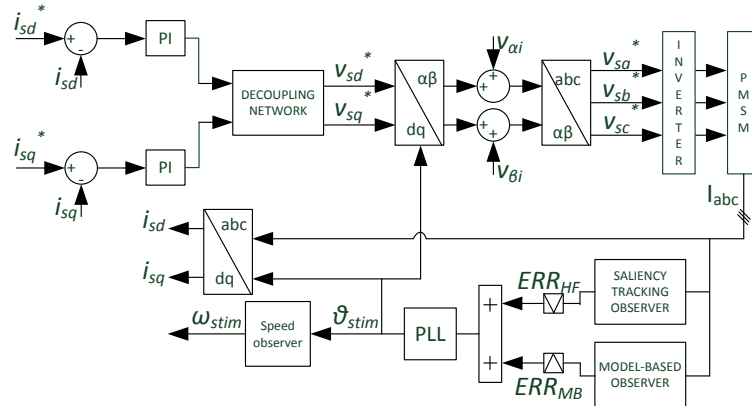

fig. 98: Hybrid control scheme when a single PLL is used

where ϑ_{stim} is the rotor position estimated by the PLL, while ω_{stim} is the rotor speed estimated by the mechanical observer [17] [20] [21].

3.5. IF Control

In this work, to simplify the integration of the control scheme in the microcontroller adopted in the final application, it has been used another starting method, which is able to start the machine from the standstill to the model-based control. The starting method is called IF control, that means current (I) frequency (F) control [22]. The IF control is simpler to be implemented in DSPs than saliency tracking control, since it requires less arithmetic operations. In addition, thanks to IF control, it is possible to control the magnitude of the currents during the starting process; so, thinking to the maximum load capability (maximum load torque at the starting), the electronic devices, which supply the phase currents, are safe from damaging.

The IF algorithm can be explained introducing an arbitrary reference system (d_{IF},q_{IF}), rotating at ω_{dqIF} speed. The d_{IF}-axis has a displacement of ϑ_{crt} with respect to phase A-axis. Supplying the machine by means of a constant magnitude phasor current, which is oriented according to quadrature axis q_{IF}, the rotor is able to rotate, because of the electromagnetic torque, given by the interaction of the permanent magnets and the stator MMF. If the speed of the reference system (d_{IF},q_{IF}) is slowly increased from the zero value, the machine is able to start. The most important thing is in increasing the frequency of the reference system (d_{IF},q_{IF}), in such a way that the rotor has the possibility to follow the stator MMF vector, without losing the synchronism. Moreover, the amplitude of the reference current must be adequate to the maximum load level expected at standstill.
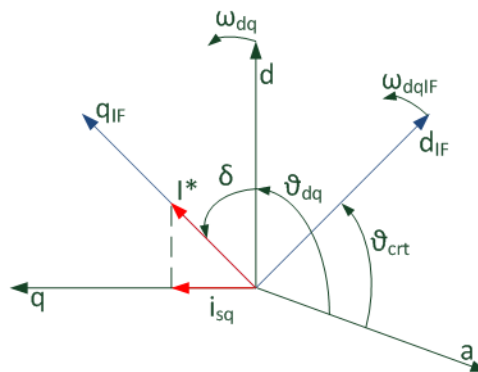

fig. 99: System (d_{IF},q_{IF})

Under IF control, the rotor is able to rotate at ω_{dq} (equal to ω_{dqIF}, the electrical pulsation of the stator currents, if the machine has two poles). In these conditions, the real d-axis has a displacement of angle δ with respect to the q_{IF}-axis, depending on the load. The higher the I^* magnitude is, the lower the δ angle is. Such angle represents the displacement between the real reference system (d,q) and the arbitrary reference system (d_{IF},q_{IF}) used to start the machine. This is a consequence of load capability of the machine. The electromagnetic torque is given by eq. 108:

$$C_e = k_T i_{sq} = k_T I^* \sin \delta \qquad\qquad \text{eq. 108}$$

at a given load level, if the I^* is low, the machine can start only when the current is close to the real q-axis. In the worst case, if I^* is too low, the machine could not be able to start at all. It is necessary to know the maximum value of the load torque at standstill, in order to choose an adequate magnitude of the current, which is able to move the rotor.

That said, the IF control realizes an open loop speed control. At steady-state, when the speed is equal to ω_{dqIF} and it is constant, the electromagnetic torque is equal to the load torque.

The variation over the time of the frequency must be suitable for the machine, considering the load conditions. Generally speaking, the heavier is the load, the slower must be the variation of the frequency. An example of frequency variation is introduced in eq. 109:

$$f^* = kt \qquad\qquad \text{eq. 109}$$

where k is a positive constant. Then, the frequency is integrated over the time, in order to obtain the angle ϑ_{crt}. Given the ϑ_{crt} angle, it is possible to make the coordinate transformation from the $\alpha\beta$ reference system to (d_{IF},q_{IF}) reference system, and vice-versa.

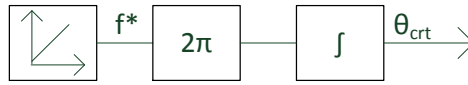$$\vartheta_{crt} = \int 2\pi f^* dt \qquad\qquad \text{eq. 110}$$

fig. 100: ϑcrt calculation

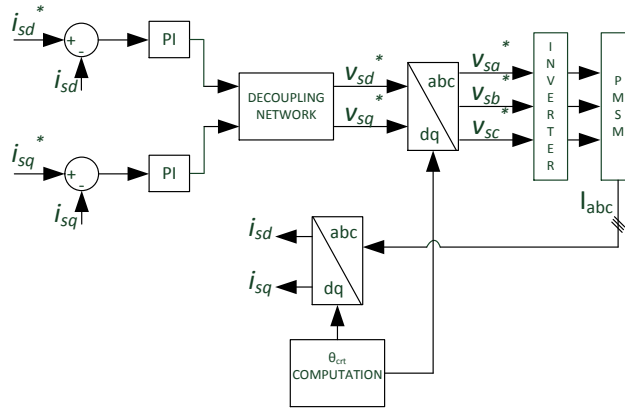The control scheme, developed in Simulink notation, is shown in fig. 101.

fig. 101: IF control scheme

The instantaneous commutation from the IF control to MB control may generate an instability condition, either due to high current value along the q-axis (there will be an increase in the torque value) either due to the under damped δ angle dynamic (the acceleration rate will increase).
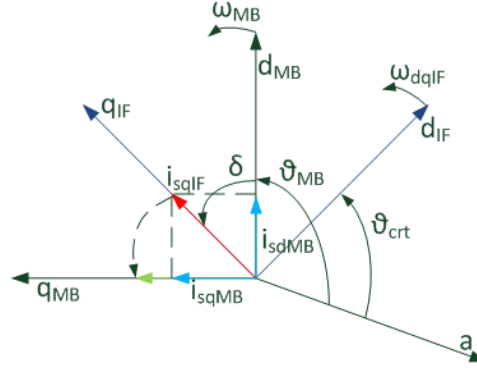
fig. 102: Phasor diagram of the phase currents, when the IF control is used

To avoid these drawbacks, it is possible to use a smooth transition from ϑ_{crt} angle to ϑ_{MB} angle (that is, the angle estimated by the MB observer). As mathematical law, the transition could follow the dynamic of a first order filter. Being t_{tr} the time when the transition must start, the angle transition can be described by using eq. 111:

$$\begin{cases} \vartheta_{tra} = \vartheta_{crt} & if\ \omega_{ref} < \omega_{min} \\ \vartheta_{tra} = \vartheta_{comp} + \vartheta_{MB} & if\ \omega_{min} \leq \omega_{ref} \leq \omega_{MAX} \\ \vartheta_{tra} = \vartheta_{MB} & if\ \omega_{ref} > \omega_{MAX} \end{cases} \qquad \text{eq. 111}$$

Where ϑ_{tra} is the angle used for transformation purposes; ϑ_{comp} is the angle in output from a first order filter, and finally ϑ_{MB} is the angle estimated by the MB observer. In particular, the filter must be set in a such way that it has an input equal to zero (u = 0) and as initial condition the error (ϑ_{crt} - ϑ_{MB}), calculated at the time ttr (eq. 112)

$$\theta_{comp} = \frac{1}{1 + s\tau_{tr}} \cdot u$$

$$\theta_{comp}(0) = \vartheta_{crt}(t_{tr}) - \vartheta_{MB}(t_{tr}) \qquad \text{eq. 112}$$

The higher is the time constant of the filter (τ_{tr}), the slower is the transition. The same logic transition can be used to avoid an excessive increase of q-axis current, during the transition from IF control to MB control. In this case the equations, stated in eq. 113, can be used:

$$\begin{cases} i_{sq}^* = i_{sqIF} & if\ \omega_{ref} < \omega_{min} \\ i_{sq}^* = i_{comp} + i_{sqMB} & if\ \omega_{min} \leq \omega_{ref} \leq \omega_{MAX} \\ i_{sq}^* = i_{sqMB} & if\ \omega_{ref} > \omega_{MAX} \end{cases} \qquad \text{eq. 113}$$

Where i_{sq}^* is the reference current along the q-axis, i_{sqIF} is the current along the q_{IF}-axis, i_{sqMB} is the current along the q_{MB}-axis, i_{comp} is the output of the first order filter, which has an input equal to zero (u = 0) and as initial condition the difference (i_{sqIF} - i_{sqMB}); as before, the difference is estimated when the switching occurs.

$$i_{comp} = \frac{1}{1 + s\tau_{tr}} \cdot u$$
$$i_{comp}(0) = i_{sqIF}(t_{tr}) - i_{sqMB}(t_{tr})$$

<div style="text-align:right">eq. 114</div>

For a given torque and time constant of the filter (τ_{tr}), the transition from open loop to closed loop is heavy, when the current i$_{sqIF}$ is high; it means that the displacement between the IF frame and estimated one is high. From the point of view of the transient, in the same interval time (equal to 4÷5 τ_{tr}), the IF frame must rotate of an higher angle and the magnitude of the reference current must decrease much more [22].

3.6. PI tuning

In all electric drives, it is needed to guarantee the robustness of the control algorithm; this is done by tuning the PI parameters properly. Particular care must be adopted when the machine parameters are not well known. Attention must be paid in the tuning the bandwidth of the current loop and speed loop. In general, the current control loop must have a bandwidth large enough, in such a way that it can track correctly the current set-point and to avoid ripple in the stator currents. In fact, the current ripple generates torque ripple; in turn, the torque ripple generates acoustic noise and losses.

If the torque and the speed have harmonics, which are multiple of the synchronism frequency, it is necessary to tune the gains of the current transducers by software, in such a way that the ripple is brought to zero.

To tune the speed control loop, it is needed to remember:

➢ The speed control loop bandwidth must be lower than the bandwidth of current control loop (at least, 4/5 times);

➢ The speed control loop must be lower than the PLL bandwidth (at least, 3/4 times).

Typical values for the bandwidths are:

➢ 200 [rad/s] - 500 [rad/s], for the current loop regulation;

➢ 50 [rad/s] - 100 [rad/s], for the mechanical observer.

To tune the PI parameters, the eq. 115 and eq. 116 are useful [17]:

• Current PI

$$k_p = L_{dq}\omega_b$$
$$k_i = R\omega_b$$

<div style="text-align:right">eq. 115</div>

• Speed PI

$$k_p = \frac{J\omega_{sc}}{K_T}$$
$$k_i = k_p \cdot \frac{\omega_{sc}}{5}$$

<div style="text-align:right">eq. 116</div>

Using the equations stated, the transfer function of the current loop is (in case of perfect cancellation of the motor pole with the zero of the controller):

$$G_i(s) = \frac{\omega_b}{s + \omega_b}$$
<div align="right">eq. 117</div>

Consequently, the open loop transfer function of the speed loop is:

$$G_v(s) = \frac{\omega_{sc}}{s}(1 + \frac{\omega_{sc}}{5s})$$
<div align="right">eq. 118</div>

In particular, ω_b is the current control loop bandwidth, R is the phase resistance, L_{dq} are the inductances along the d-axis and the q-axis, k_T is the torque constant, J is the inertia momentum, and, finally, ω_{sc} is the bandwidth of the speed control loop chosen by the operator during the design phase. To make easier the tuning of the speed loop, the transfer function of the current loop has been supposed equal to 1 (for this reason G_i is absent in eq. 118) and the viscous coefficient B has been neglected.

3.7. Parametric identification

The tuning rules presented in the previous section require the knowledge of machine parameters that must be identified as explained in chapter II. Their values are summarized-up in Table 28, Table 29 and Table 30. Here, only the current-voltage model identification of the inverter is described.

3.7.1. Mechanical and electromagnetic identification results

The mechanical parameters are in Table 28.

Table 28: MECHANICAL PARAMETERS

Mech. Para.	Value
J	1.12e-4 [Nms^2/rad]
B	2J [Nms/rad]
K_c	0.0145 [Nm/A]

Using the electromagnetic model identification, the inductance values obtained are (Table 29):

Table 29: Ld AND Lq VALUES BY ELECTROMAGNETIC IDENTIFICATION

Inductance	Value
L_d	61 µH
L_q	73 µH

Using the standstill tests, the inductance values obtained are (Table 30):

Table 30: Ld AND Lq VALUES BY STANDSTILL METHODS

Inductance	Value
L_d	45 µH
L_q	57 µH

In this work only the inductance values obtained by electromagnetic identification are used; in addition, a short investigation about the anisotropy of the machine has been realized.

The anisotropy of the machine has been investigated using the high frequency injection method, varying the reference current along the q-axis (i_{sq}). This task has been necessary in order to check the anisotropy in all the possible operating conditions, when the high frequency injection method is used. The value of the injected frequency was set to 200 [Hz]; the value of the injected voltage amplitude was equal to 2 [V]. Varying the i_{sq} set-point, it is possible to check the anisotropy of the machine in different operating conditions.
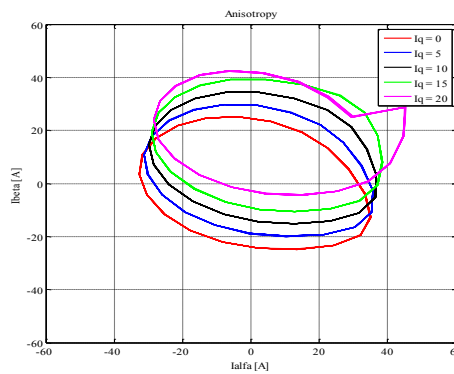

fig. 103: Current locus in the αβ frame, varying i_q values

When the set-point along the q-axis is set to zero (the fundamental frequency is set to zero during the tests), the anisotropy ratio is equal to 0.67 (it is possible to calculate it by observing the fig. 103). In particular, from fig. 103, it is possible to see the high frequency current value, which is equal to about 35 [A]. When the q-current set-point is different from zero, the current locus translates in upward direction, but the ratio between the two axes stays constant, as one can see from fig. 103.

In general, to show the anisotropy of the machine, it is necessary to get high current values; for the prototype analyzed, the high frequency current to be used to exasperate the anisotropy is more than 20 [A].

3.7.2. Inverter voltage-current model identification

The voltage-current model of the inverter is not linear, especially when the duty-cycle values are low. This phenomenon comes from power switches, whose resistance varies from the on-state to the off-state (in addition, the power switches resistance depends on the current value). There is also an additional issue, which comes from the dead-time. If the non-linearity of the inverter is compensated, it is possible to get quasi-sinusoidal stator currents using sinusoidal reference voltages. Different methods can be used, but in this work only the self-commissioning method described in [23] is used.
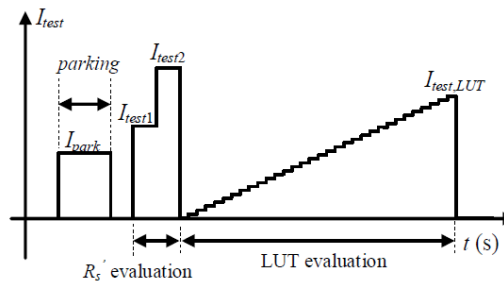

fig. 104: Self-commissioning procedure

During this test, the machine is vector current controlled. The first operation is the alignment of the phase A-axis with the d-axis (this operation is called parking). After that, two current impulses along d-axis are applied, in order to evaluate the total phase resistance (which is the sum of the phase resistance, wires resistance, power switches resistance). After the parking operation, the self-commissioning procedure can start. The self-commissioning consists of emitting a series of current impulses along the d-axis, whose values increase over the test execution. The experimental curve obtained by the self-commissioning operation is reported in fig. 105.
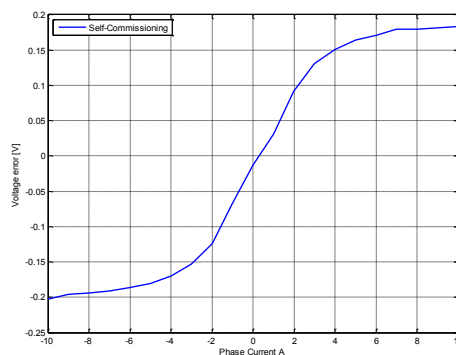

fig. 105: Voltage-current curve of the inverter using the self-commissioning procedure

Thanks to the self-commissioning procedure, it is possible to estimate the total phase resistance, which is about 40 [mΩ].

It must be remembered that the voltage-current model of the inverter depends on the dead-time and switching frequency. In the case of this experiment, the dead-time is equal to 0.8 [μs]; the switching frequency is equal to 10 [kHz].

3.8. Experimental results

In order to test the motor experimentally, using the sensorless control developed for this purpose, a DSpace platform has been used. The DSpace system used is equipped with a control board DS1006 AMD Opteron_QC (2.8 [GHz]) and an FPGA board (Xilinx Virtex-5 SX95T). In particular, to the FPGA is demanded the task of sampling the stator currents, the signals from the encoder and generating of PWM signals. In the test bench is also used a RapidPro unit, which is a multi-integrated inverter, equipped with 4 power units DS178. To carry out the experiments, the maximum DC voltage value must be equal to 24 [V] due to the final automotive application.
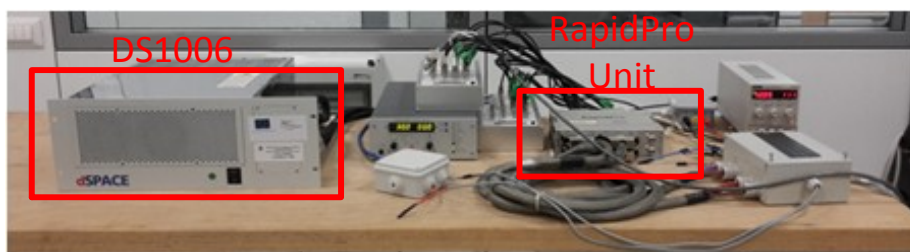

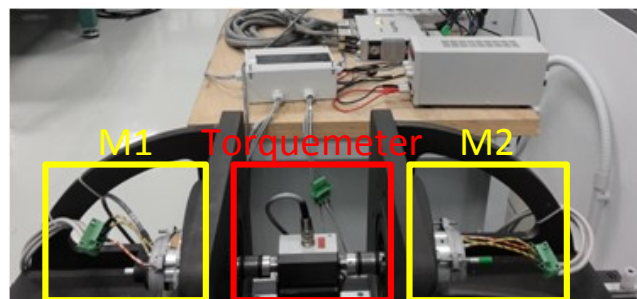fig. 106: Test-bench equipped with DSpace

fig. 107: Motors under test

3.8.1. Performance indicators evaluation for testing the sensorless control

The minimum performances required by the control are:

➤   Acceleration rate: 840 rad/s^2;

➤   Reference speed: 800 rad/s;
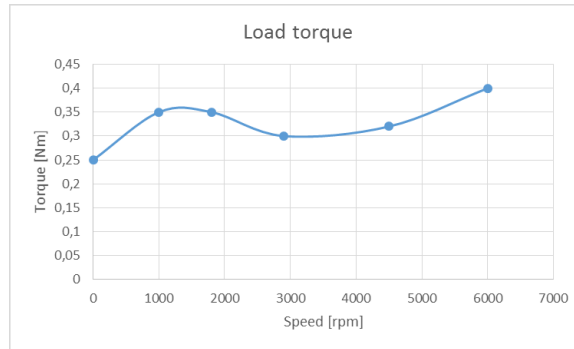
➤   Load as fig. 108 shows:

fig. 108: Load torque profile

Since the control is implemented in the discrete-time domain, there are delays between the currents samples and PWM updates. These delays are proportional to the sampling time T_c (which is equal to 100 [μs]). So, in order to estimate correctly the rotor position, it is necessary to take into account the timing of the microcontroller used by DSpace.
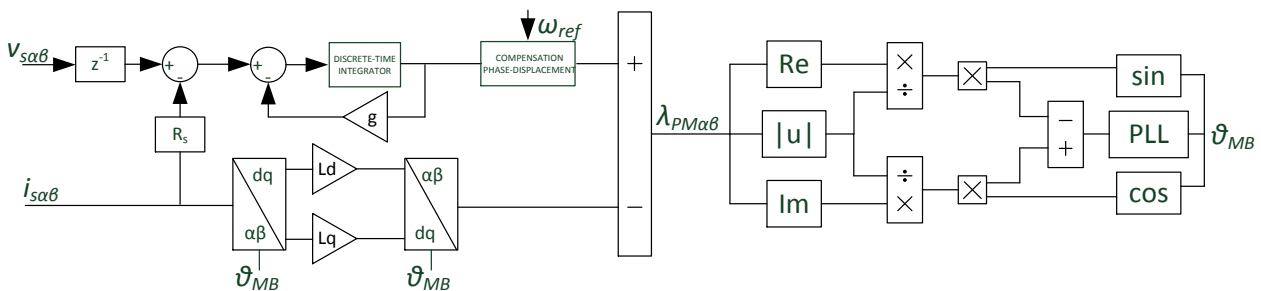

fig. 109: Model-based observer for a correct rotor position estimation

Consequently, the model-based observer scheme has been modified as fig. 109 shows; that is, it has been inserted a delay equal to T_c on the reference αβ voltages. This helps reducing the angle error, which is the difference between the real angle and the estimated one. The angle error depends on the voltages magnitude too. In fact, due to asynchrony between the current sampling and the PWM update, a voltage magnitude error is present at low speeds. Concerning the last problem, at 800 [rad/s] the error between the reference voltages and the real ones is negligible. So, it is possible to say that in order to compensate the error angle, it is necessary to insert only a delay equal to T_c in the observer.

The control must satisfy some KPIs (Key Performance Indicator); in particular, they are:

1.   Computing time;

2.   Nominal performance;

3.   Minimum transition speed to model-based control;

4.   Ability to read a starting failure;

5. Minimum error angle at steady-state;

6. Robustness of the MB control against the parameters variations.

In addition, the following performances must be satisfied:

➢ Torque quality;

➢ Maximum torque load at the start;

➢ Load torque estimation;

➢ Minimum current for the starting (< 45 [A]).

In order to estimate the torque quality, only the interaction between each edge of the rotor PMs with the slot opening are considered (in this case, the electrical machine has been supposed as it was a surface permanent magnet machine) [4].
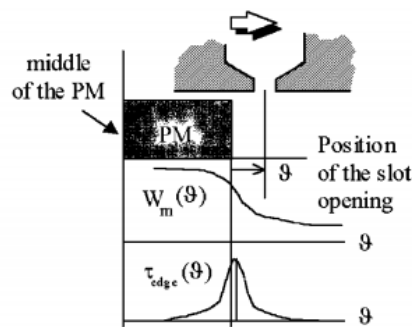

fig. 110: Simple model of the T_{cog} mechanism, based on the superposition of each PM edge

In fig. 110 it is explained the mechanism of cogging torque generation. The physical explanation is in the magnetic energy W_m, sum of the air and PM energies, which is a function of the angular position ϑ_r. If the slot opening is in the middle of the PM, the variation of W_m with ϑ_r is null, while it is large if the slot opening is near to the PM edge. Moreover, W_m is monotonously decreasing with ϑ_r, as shown in fig. 110. The number of cogging torque period during a slot pitch rotation is computed by:

$$N_p = \frac{Poles}{GCD(Slots; Poles)}$$
eq. 119

In our case N_p is equal to 2; because of that, the mechanical angle corresponding to each period is:

$$\alpha_{\tau c} = \frac{2\pi}{N_p \cdot Slots}$$
eq. 120

So, the ripple will be calculated by means of eq. 109:

$$Ripple_\% = \frac{HO_{24}}{HO_{DC}} \cdot 100$$
eq. 121

where HO indicates the acronym "Harmonic Order". In eq. 121, the 24th harmonic ($24 \cdot f_m$) produces the cogging torque (the torque ripple is calculated at steady-state). Due to the noisy nature of the

torque meter output, only the torque component at $24 \cdot f_m$ will be measured to evaluate the torque quality.

Before introducing the experimental data, it may be useful to observe the speed dynamic when the mechanical observer is used, in order to demonstrate the benefits from using it. From fig. 111 b), it is possible to see the speed estimated by mechanical observer (green curve) and the measured speed (red curve). Although the hybrid control is used, the estimated speed does not contain an high harmonic content; this leads to reduced torque ripple; instead, the speed estimated by the PLL has an high harmonic content; for this reason it cannot be used for control purposes.
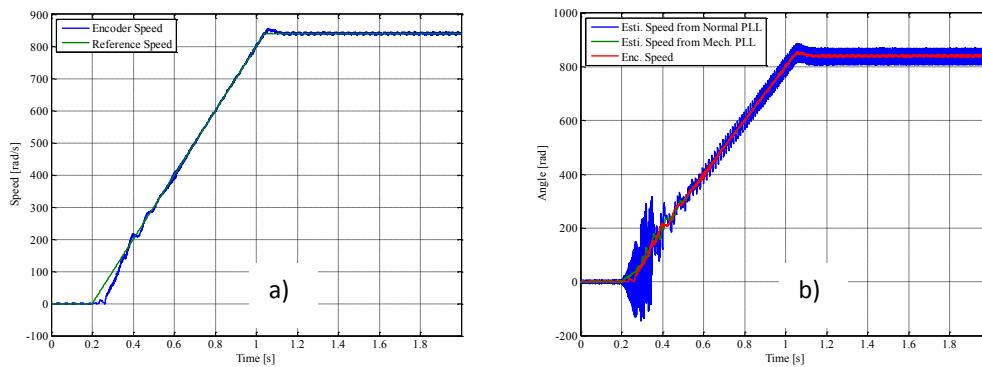

fig. 111: a) Reference and measured speed; b) Comparison between the measured speed (red curve) and speed estimated by: PLL (blue curve), mechanical observer (green curve) when the hybrid control uses a single PLL

Concerning the PI tuning, it has been preferred to use an experimental method. In particular, for the current control loop, the dynamic is shown in fig. 112:
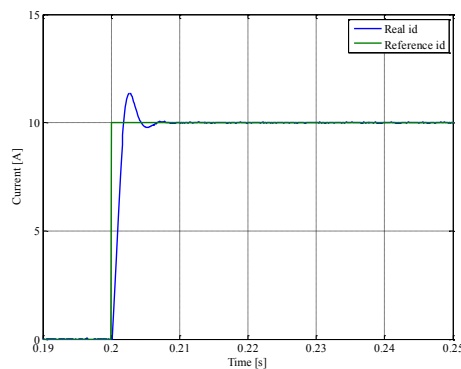

fig. 112: id response when the set-point is equal to 10 [A]

The speed PI regulator has been tuned by using a trial-and-error method, in such a way that the PI is able to satisfy the requirements (in particular, starting time at rated load). In the end, the electrical machine has been treated as if it was isotropic; so, no reference has been set along the d-axis current.

3.8.1.1. KPI investigation

Computing time

The computing time for each control method is reported in Table 31. It is expressed in mathematical operations, in such a way that it is independent from the microprocessor architecture.

Table 31: COMPUTING TIME, WHEN IF CONTROL AND HF CONTROL ARE USED FOR THE STARTING

Control Type	Number of operations
IF method	166 arithmetic operations
	13 integrators
HF method	275 arithmetic operations
	11 integrators

To verify the other KPI requirements, the first task is the calculation of the nominal performance:

➢ Acceleration rate equal to 1000 [rad_e/ s^2] (higher than the specification);

➢ Nominal load (fig. 108);

➢ Reference speed equal to 800 [rad_e/s].

finally, the switching to the model based control occurs to the constant value 200 [rad_e/s]. The most important thing to remember is that all the tests are pursued under load (as load a twin motor is used; in particular, the load motor is vector current controlled using an encoder), so the requirement about the load capability at the starting is automatically satisfied; in addition, for each case the torque ripple is highlighted.
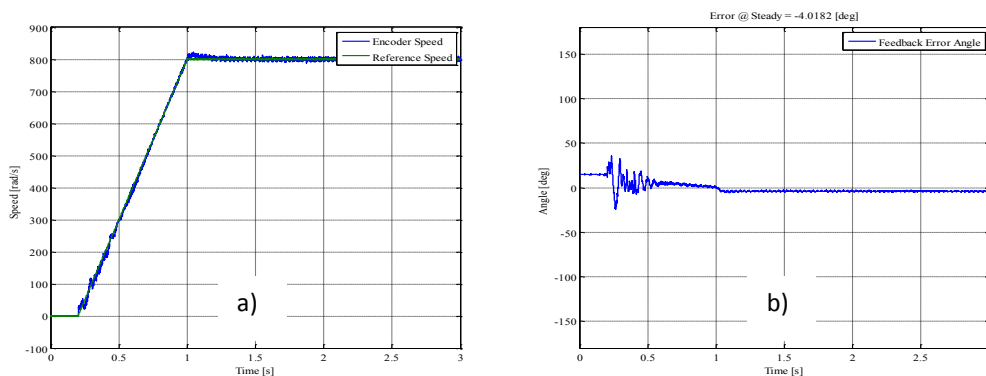
Nominal performance:

fig. 113: HF control (torque ripple equal to 0.6%): a) Speed; b) feedback error position - Nominal performance
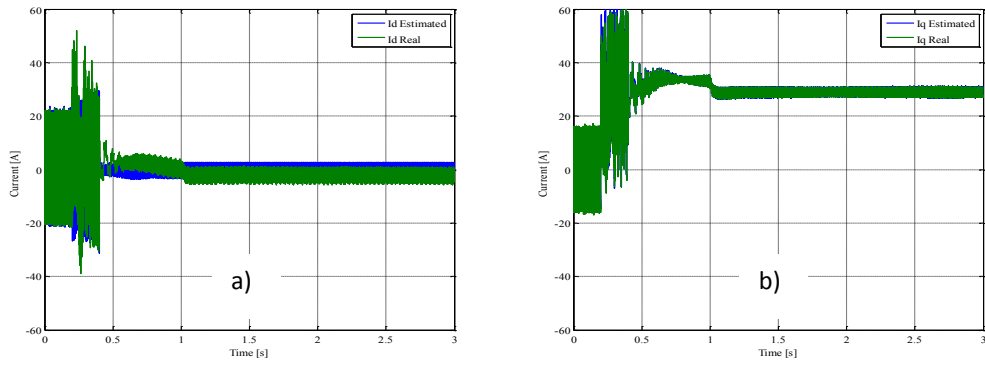
fig. 114: HF control: a) real and estimated i_{sd}; b) real and estimated i_{sq} - Nominal performance
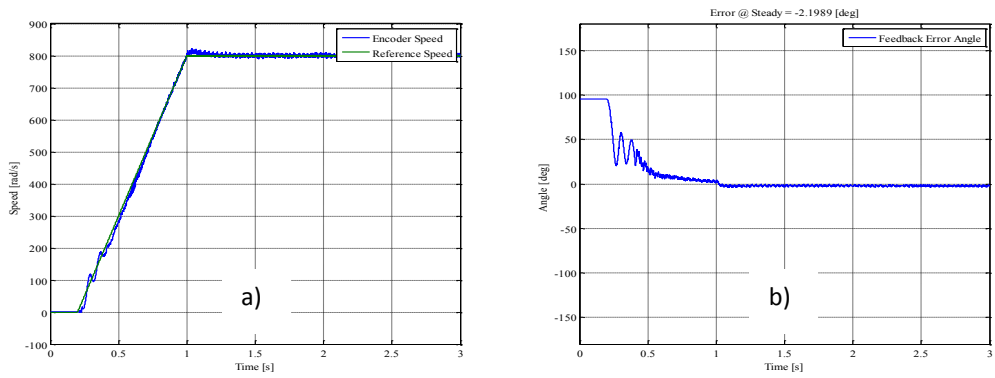

fig. 115: IF control (torque ripple equal to 2.1%): a) Speed; b) feedback error position - Nominal performance
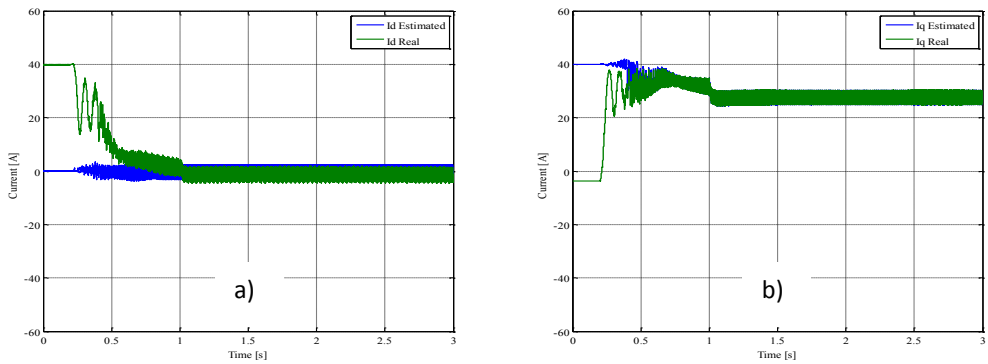

fig. 116: IF control: a) real and estimated i_{sd}; b) real and estimated i_{sq} - Nominal performance

Minimum transition speed to model-based control:

This analysis has been performed in this case the switching to model-based control occurs at 50 [rad$_e$/s]; the speed set-point and the load are the same as said before.
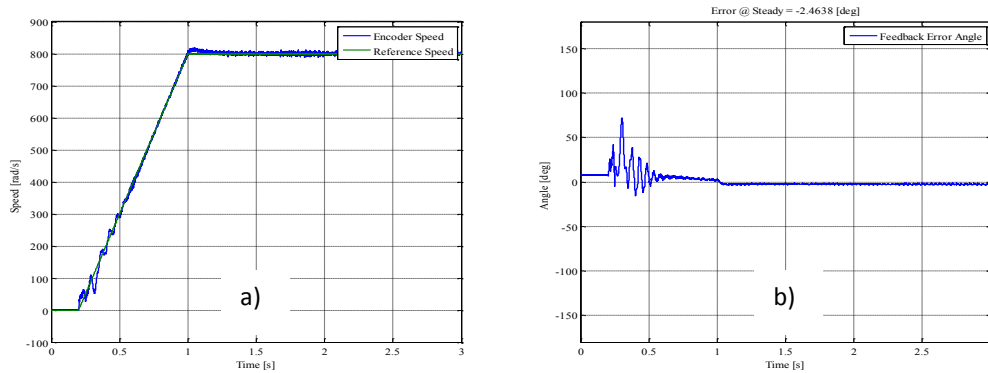

fig. 117: HF control (ripple torque equal to 0.5%): a) Speed; b) feedback error position - Minimum transition speed to model-based control
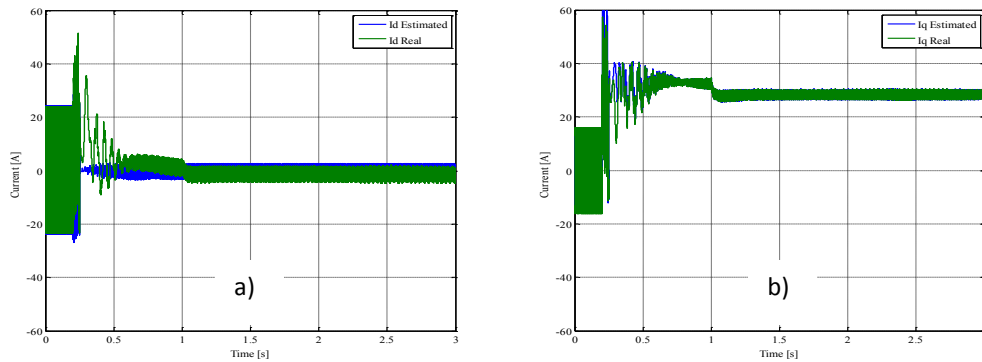

fig. 118: HF control: a) real and estimated i$_{sd}$; b) real and estimated i$_{sq}$ - Minimum transition speed to model-based control
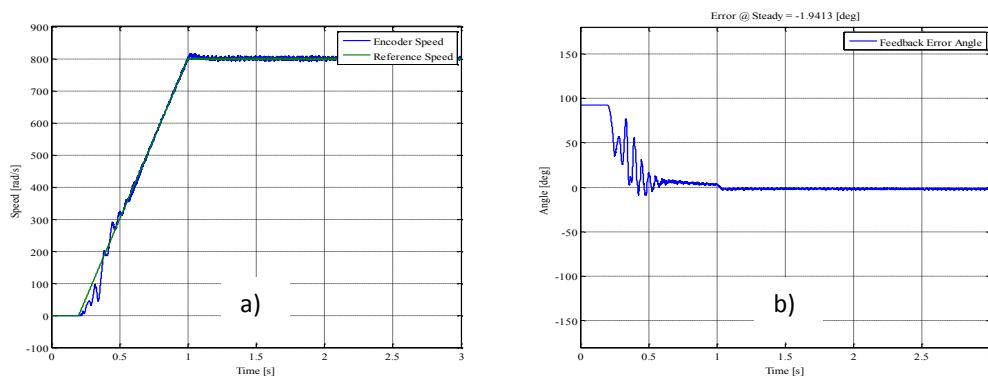

fig. 119: IF control (torque ripple equal to 0.81%): a) Speed; b) feedback error position - Minimum transition speed to model-based control
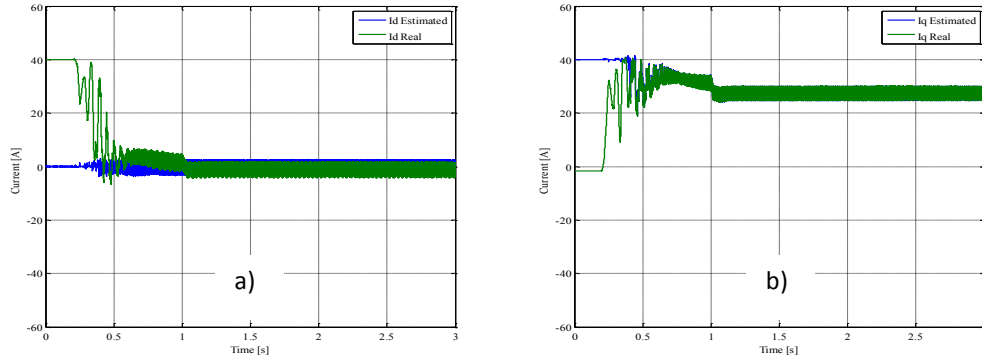
fig. 120: IF control: a) real and estimated i_{sd}; b) real and estimated i_{sq} - Minimum transition speed to model-based control

Although the transition speed is much lower than one used in nominal condition, the speed control is able to drive the machine until the speed set-point. This is possible, because the PM flux is quite strong and its action becomes fundamental for the estimation of rotor position as soon as the speed becomes higher than 24 [rpm] (10 [rad$_e$/s]); so, after a short transient, the MB control is able to drive the machine. The results here reported only consider transition speed down to 50 [rad$_e$/s], being this value low enough for the specific application. A compromise between dynamic performances (speed transient behaviour) and the need of switching to MB control as soon as possible to reduce current and control the torque must be obtained in selecting the transition speed.

Load torque estimation:

At steady-state the electromagnetic torque is equal to load torque. To evaluate the electromagnetic torque, it is possible to use the eq. 122:

$$T_e = K_T i_{sq} \qquad \text{eq. 122}$$

where k_T is the constant torque, equal to 0.0145 [Nm/A] and i_{sq} is the current along the estimated q-axis. The estimated torque is compared with the measured shaft torque.
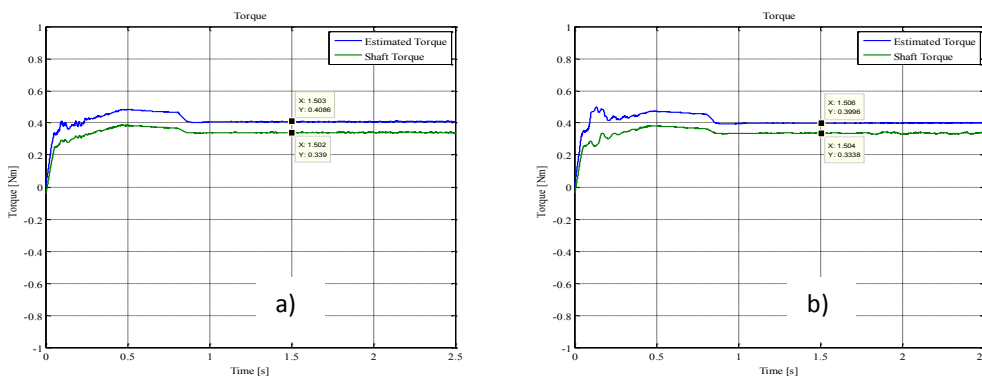

fig. 121: HF control: Measured and estimated torque in the case the transition is at: a) 200 [rade/s]; b) 50 [rade/s]
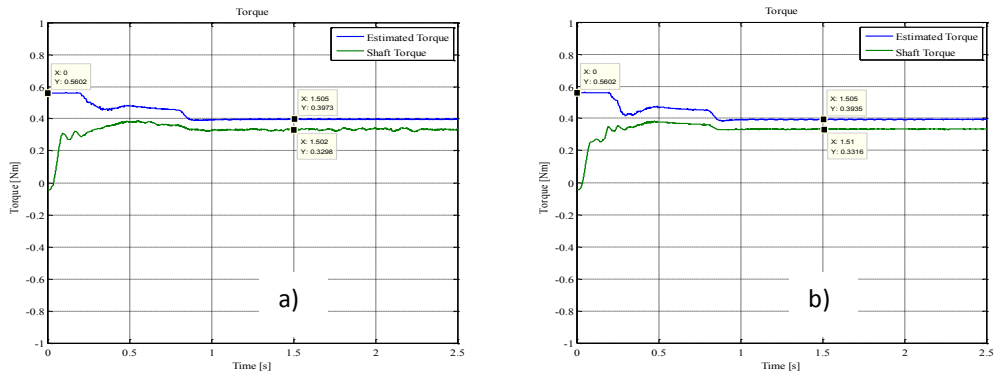
fig. 122: IF control: Measured and estimated torque in the case the transition is at: a) 200 [rade/s]; b) 50 [rade/s]

In the case the HF control is used for the starting, it is possible to notice that from the starting to steady-state the estimated torque waveform is similar to the measured value, although there is an offset between the two waveforms. In particular the offset is justified considering mechanical losses. It is possible to calculate the offset at steady-state; such value is equal to 0.07 [Nm], about equal to the measured friction torque at 2700 [rpm] and analyzed in chapter II, in the paragraph 2.5 [13]. If the IF control is used, fig. 122 demonstrates its inability to estimate the electromagnetic torque. In fact, at the starting the IF control estimates an electromagnetic torque much higher than real one; only, at steady-state, when the model-based control is acting, there is a good estimation of the electromagnetic torque.

Minimum error angle at steady-state:

Another key point is the estimation of position errors in nominal conditions. The results are:
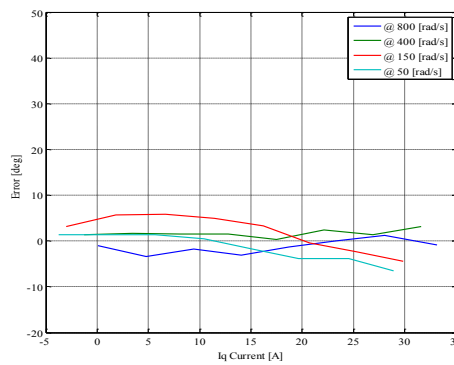

fig. 123: HF control: Error position for different i_{sq} values and for different speeds

In fig. 123 is shown the error angle in the case the steady-state speeds are:

➢   50 [rad$_e$/s]

➢   150 [rad$_e$/s]

➢   400 [rad$_e$/s]

> ➤ 800 [rad$_e$/s]

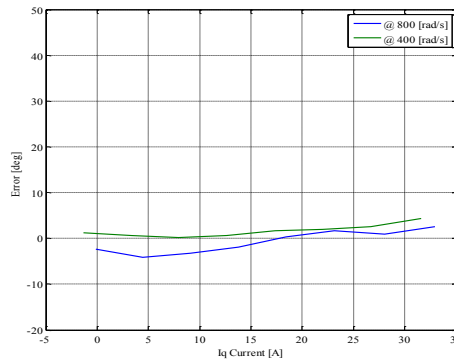The same graph has been obtained when the IF control is used (fig. 124):

fig. 124: IF control: position for different i$_q$ values and for different speeds

The fig. 124 has been obtained for two different speeds; that is, 400 [rad$_e$/s] and 800 [rad$_e$/s], because it makes no sense to talk about position errors when the IF control is on. For this reason, from 200 [rad$_e$/s] and on, the position error both for IF control and for HF control are more or less equal each other. The values along the x-axis of fig. 123 and fig. 124 are the actual i$_{sq}$ current values at steady-state of the motor under test. The most important thing to be noticed is that the error value is in the range ±10 [deg.] in both cases. This is a good result, because it demonstrates that it is possible to drive the electrical machine without having a lot of Joule losses because of a bad rotor estimation.

Robustness of the MB control against the parameters variations:

The main purpose is to investigate the performances of the MB observer in the estimation of the rotor position when the electromagnetic parameters used for the motor model (see the scheme shown in fig. 109) are wrong. The IF control and HF control are not considered during this investigation because their performances do not rely on the motor model parameters. In particular, the following tests are realized under load equal to the rated value (see fig. 108).

So, varying the resistance and the inductance values inside the MB observer, the robustness of its performances against parameters variations is investigated; in particular, it has been supposed a variation equal to ±20% for each parameter. Table 32 reports the parameters values considered during the tests.

Table 32: MACHINE PARAMETERS USED FOR THE ROBUSTNESS ANALYSIS

Parameter	Nominal value	Variation +20%	Variation -20%
R_s	38 mΩ	46 mΩ	30 mΩ
L_d	61 μH	73 μH	50 μH
L_q	72 μH	86 μH	58 μH

fig. 125: HF control (torque ripple equal to 0.95%): a) speed; b) position error / Rnomi+20%

fig. 126: HF control (torque ripple equal to 3%): a) speed; b) position error / Rnomi-20%

fig. 127: IF control (torque ripple equal to 4.1%): a) speed; b) position error / Rnomi+20%

fig. 128: IF control (torque ripple equal to 0.6%): a) speed; b) position error / Rnomi-20%

fig. 129: HF control (torque ripple equal to 2.1%): a) speed; b) position error / Ldnomi+20%
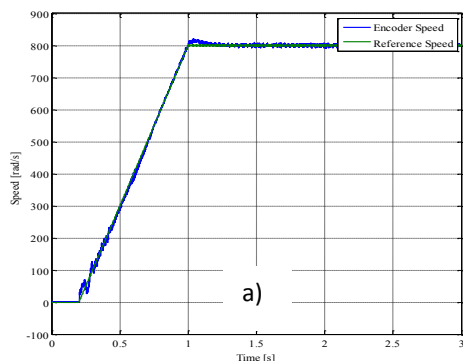
fig. 130: HF control (torque ripple equal to 0.6%): a) speed; b) position error / Ldnomi-20%
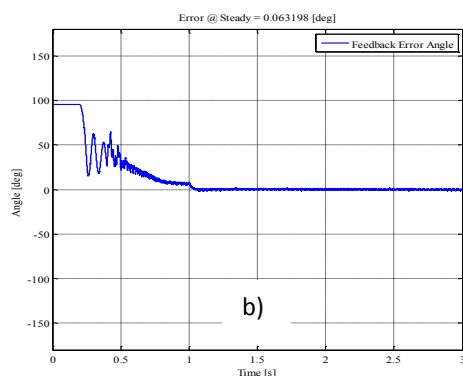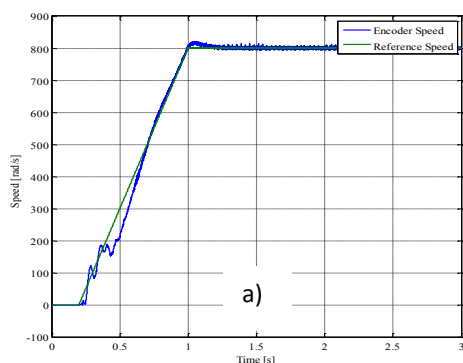
fig. 131: IF control (torque ripple equal to 0.015%): a) speed; b) position error / Ldnomi+20%
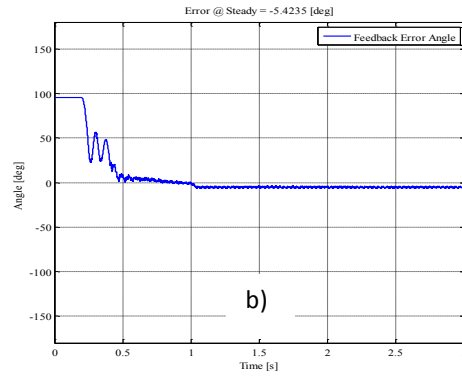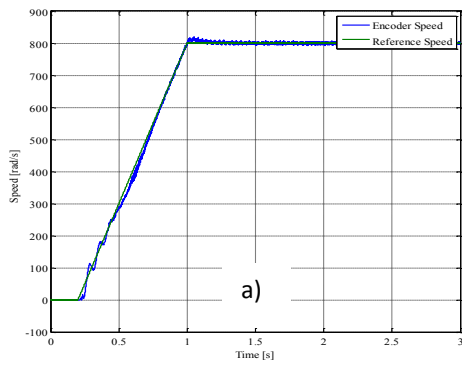
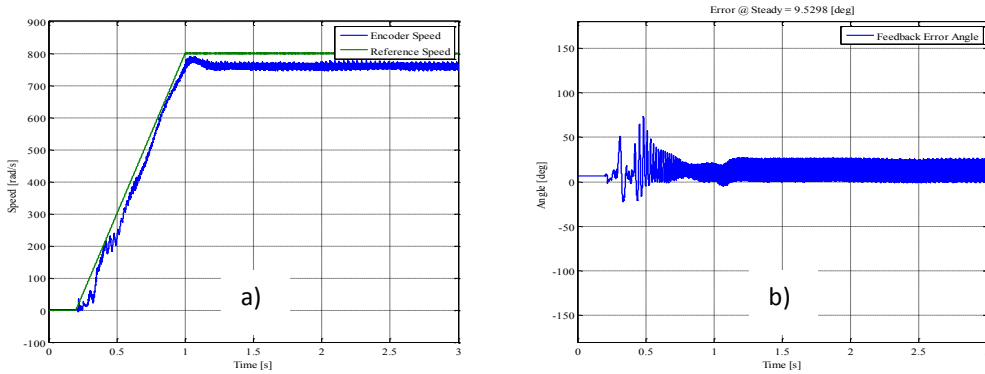fig. 132: IF control (torque ripple equal to 0.46%): a) speed; b) position error / Ldnomi-20%
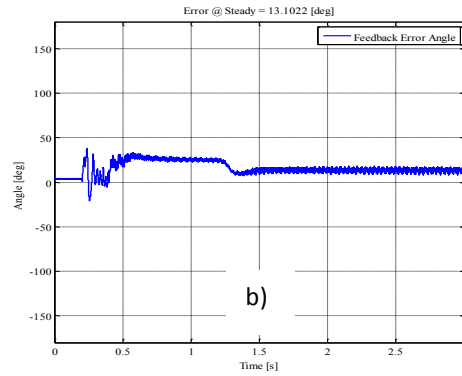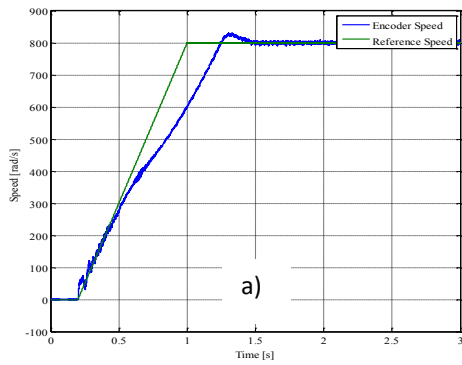
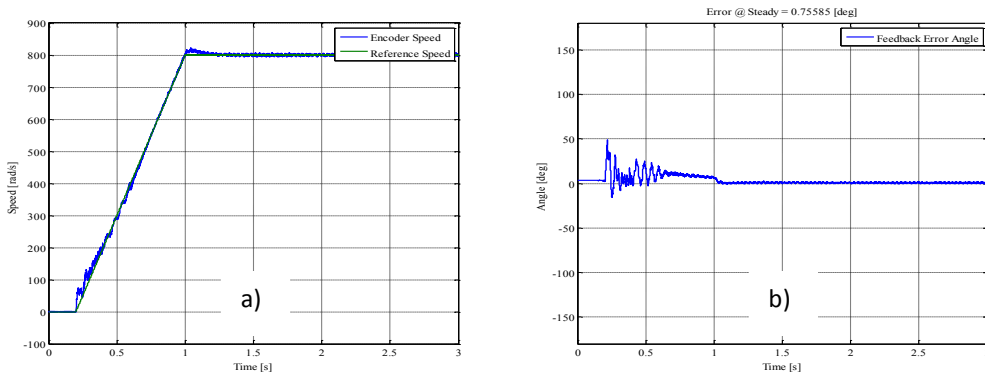fig. 133: HF control (torque ripple equal to 0.5%): a) speed; b) position error / Lqnomi+20%
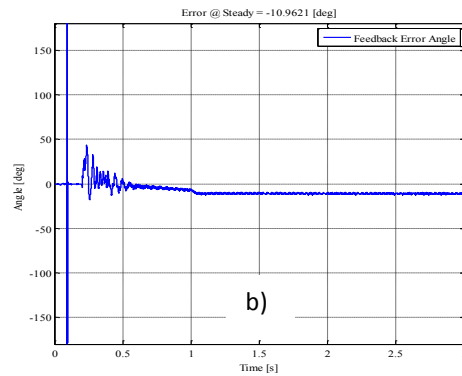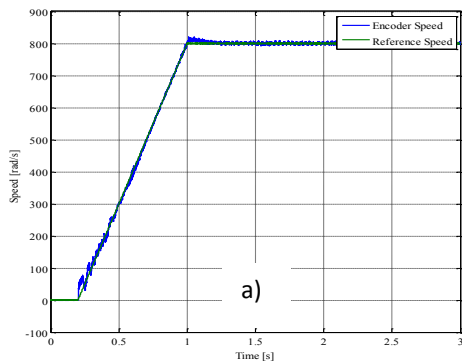
fig. 134: HF control (torque ripple equal to 3.2%): a) speed; b) position error / Lqnomi-20%
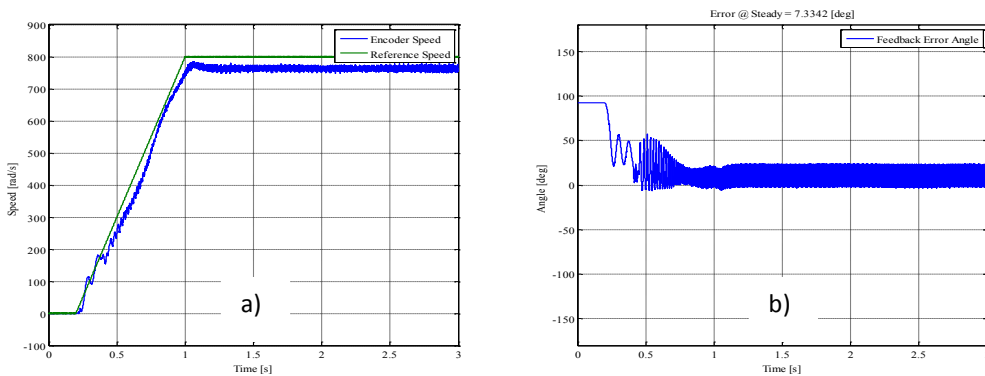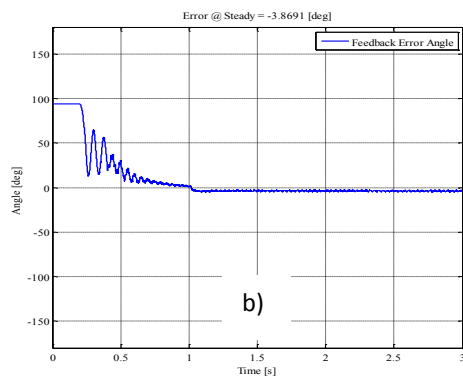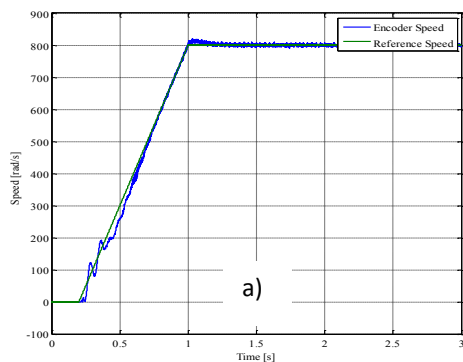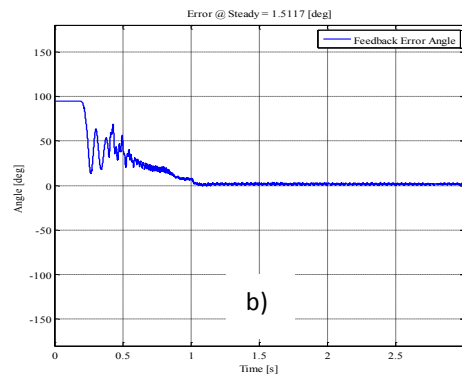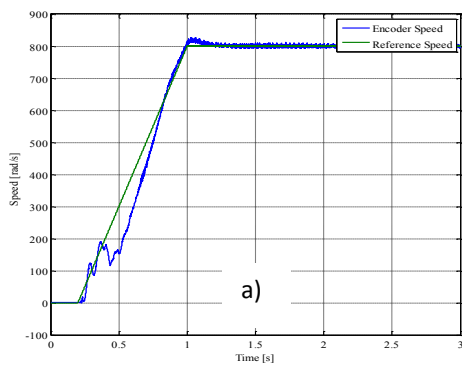

fig. 135: IF control (torque ripple equal to 0.61%): a) speed; b) position error / Lqnomi+20%

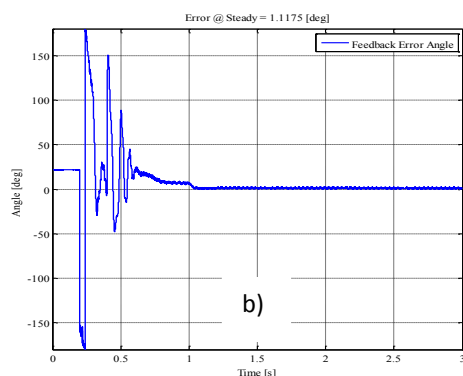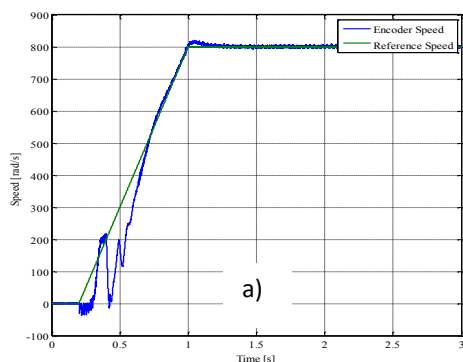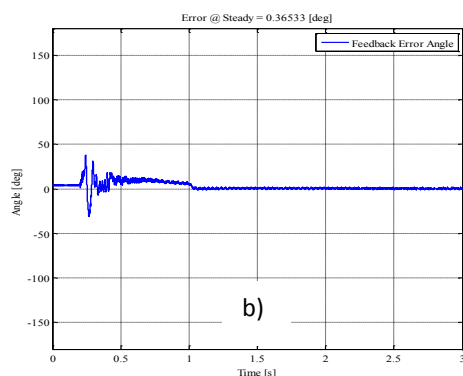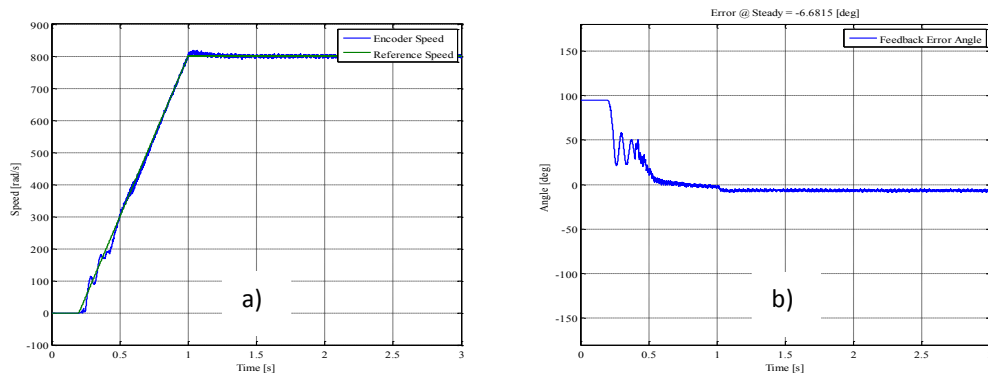fig. 136: IF control (torque ripple equal to 0.45%): a) speed; b) position error / Lqnomi-20%

Ability to read a starting failure:

fig. 137 reports the estimation of the PM flux in output from the MB observer, when the HF control is used for the starting; the test is pursued under load. Till the motor is still, the estimated flux is zero. At steady-state its value is equal to 0.003 Vs/rad. Such value indicates that the starting has happened successfully; if the machine does not start, the reason is in the phase currents; consequently, the estimated rotor flux will be equal to zero, as in the first part of the experiment in fig. 137.
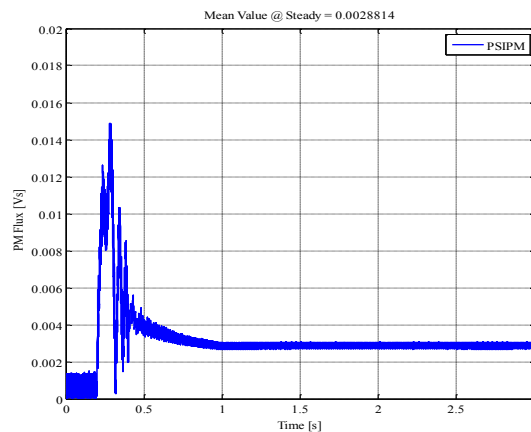
fig. 137: Rotor flux in output from the model-based observer

Concluding, the developed sensorless control algorithm is able to drive the electrical machine until the speed set-point in all situations, also when there is a mismatch between the real electromagnetic parameters and estimated ones and these are used inside the MB observer. Regarding the requirement about the torque ripple, it can be stated that it is lower than 5%; so, the electrical machine is not a source of noise and vibrations. Finally, the requirement about the current (max. 45 [A]) is not satisfied only in the case the HF control is used.

3.9. Particularities on the MB observer

In this paragraph, a deeper analysis of the MB observer is presented, in order to analyse viable solutions to improve its performances. In particular, for this analysis, the parameters used for the motor model will be modified to verify the performances of the position observer when the model and motor parameters have significant differences. On the basis of the analysis described in 3.8.1.1 about the *Robustness of the MB control against the parameters variations*, it is evident how the resistance value is harmful, when it increases; on the other side, the starting performances are poor, when the inductance values are higher than nominal ones. In this paragraph the behaviour of the MB observer is investigated, in two cases:

➢ The resistance value is lower than nominal one;

➢ The inductance values are lower than nominal ones.

The main goal of this analysis is to verify the possibility, respectively:

➢ To improve the rotor position estimation at steady-state;

➢ To decrease the switching speed.

For the first case, in order to highlight a benefit obtained using a lower resistance value, the error angle (difference between the estimated angle and measured one) at steady-state is shown, when the following conditions occur:

➢ Absence and presence of the delay on the $v_{\alpha\beta}$ voltages in input to model-based observer;

➢ Phase resistance value variation in the range $10m\Omega \div 38m\Omega$;

➢ Absence and presence of the phase delay compensation of the low-pass filter, used as integrator inside the MB observer.

In particular, the tests have been performed at 1000 [rpm] (because the lower is the speed, the worse is the estimation).

From fig. 138 and fig. 139, it is evident that the estimation quality is worse when there is not the compensation of the displacement given by the low-pass filter used as integrator in the MB observer; in addition, when a delay is used for the voltages in input to MB observer, the estimation improves. In general, no benefit is present when the resistance value is lower than nominal one.
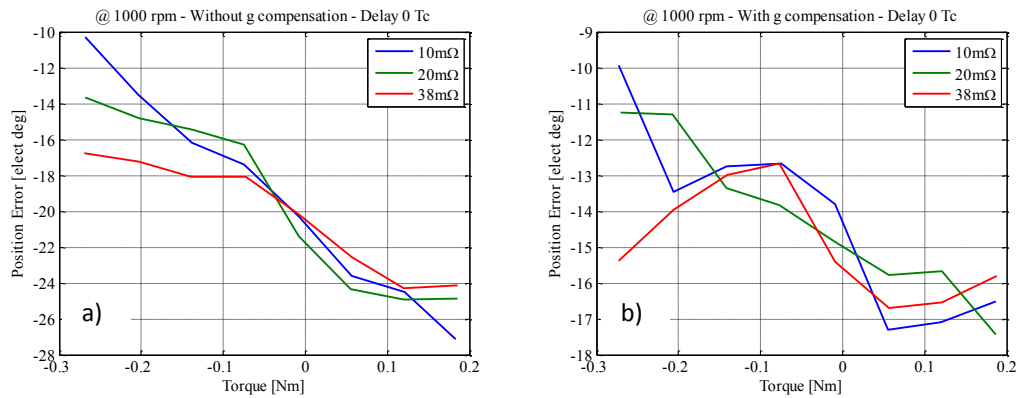
fig. 138: Error angle at 1000 [rpm], no delay: a) without g compensation; b) with g compensation
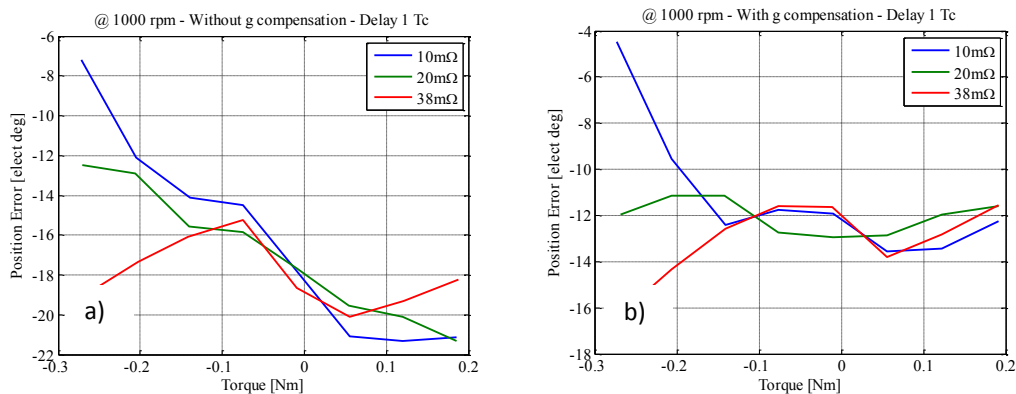
fig. 139: Error angle at 1000 [rpm], 1 T$_c$ delay: a) without g compensation; b) with g compensation

The other investigation is focused on the inductance values.

The used switching speeds are:

- 24 [rpm] equal to 10 [rade/s];
- 48 [rpm] equal to 20 [rad$_e$/s].

In particular, the IF control has been used for the starting; in addition, the following settings have been used:

- Delay equal to 1 T$_c$ for voltages used in the MB observer;
- Phase resistance equal to 38 [mΩ];
- Compensation of the low-pass filter used as integrator in the MB observer;
- Test under load (load according to fig. 108).

The fig. 140 is used as comparison; it is possible to observe that using the nominal inductance values, the switching to MB is successful, even if there could be some difficulties at starting.
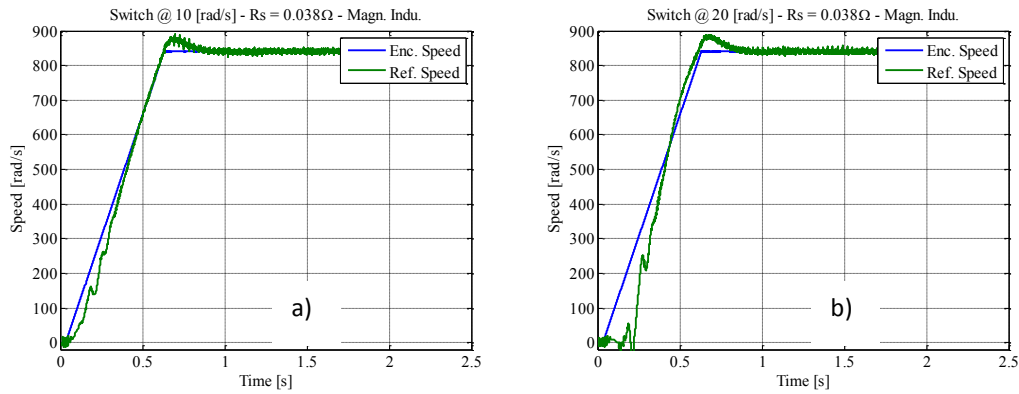
fig. 140: Starting performance at: a) 24 [rpm] (10 [rad$_e$/s]) b) 48 [rpm] (20 [rad$_e$/s]), using the nominal inductances

The following figures (fig. 141 and fig. 142) show the results of the analysis, when the machine is treated as if it was isotropic (i.e. $L_d=L_q$).
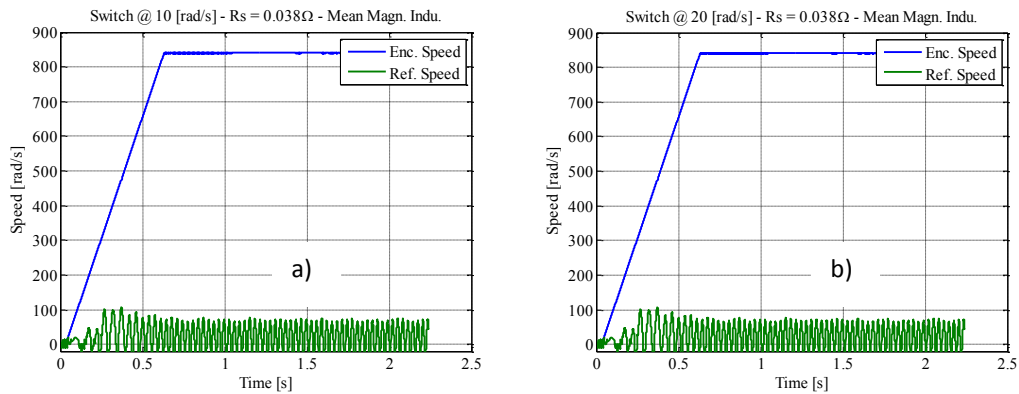
fig. 141: Starting performance at: a) 24 [rpm] (10 [rad$_e$/s]) b) 48 [rpm] (20 [rad$_e$/s]), if $L_d=L_q=67$ [μH]
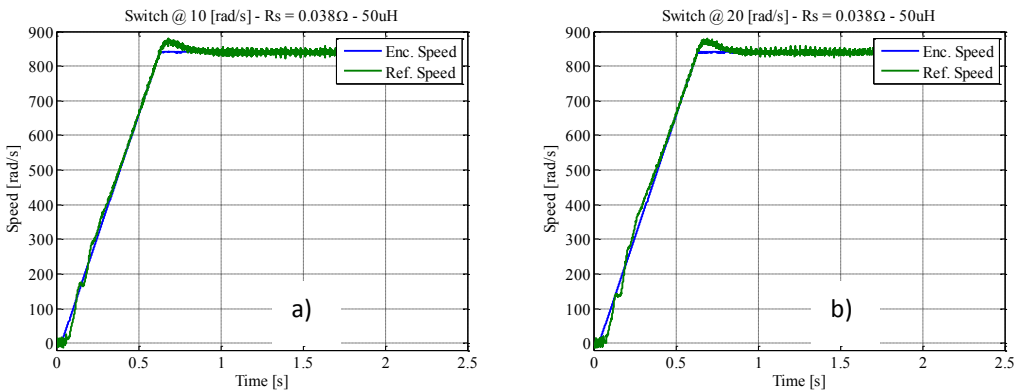
fig. 142: Starting performance at: a) 24 [rpm] (10 [rad$_e$/s]) b) 48 [rpm] (20 [rad$_e$/s]), if $L_d=L_q=50$ [μH]

Concluding, the switching speed can be decreased, also using inductance values lower than nominal ones. To solve the difficulties at the starting, a way could be in using a different speed reference profile, in order to permit MB observer to get the convergence, before the switching happens.

3.10. Pump characterization

The sensorless control algorithms analyzed and implemented in DSpace have been tested on the real test-bench, which reproduces a small part of the diesel injection system. On the high pressure pump, the outlet connections have been short-circuited. Between the high pressure pump and the low pressure one, there is a diesel filter, used to slow down the pressure decrease at the pump output. The test bench configuration is shown in fig. 143:
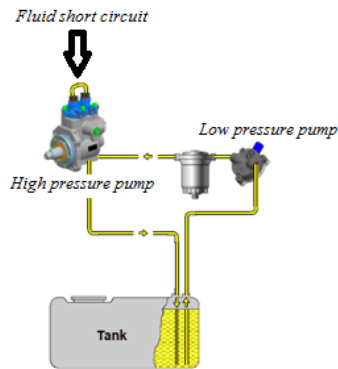
fig. 143: Test bench with the real load for testing the sensorless control

The characterization of the pump has been the first step. The characterization consists of testing the mechanical pump for different pressures and flowrates; to accomplish that, only the reference speed has to be tuned, in order to obtain (for a given delta pressure) the reference flowrate. In addition, in order to analyze a particular operating condition, the fuel has been heated to 40 [°C] and 80 [°C].

The different flowrates and delta pressures considered are:

➢ Δp = 2 bar – 4 bar – 6 bar – 8 bar (Input of the characterization procedure);

➢ Flowrates = 100 l/h – 200 l/h – 300 l/h – 400 l/h (Output of the characterization procedure);

The speed is not measured, because it is not possible to use an encoder inside the test-bench; the only available speed information comes from the MB control; so, it is possible to have only an estimation of the rotor speed. The results of the pump characterization are shown in fig. 144 and fig. 145:
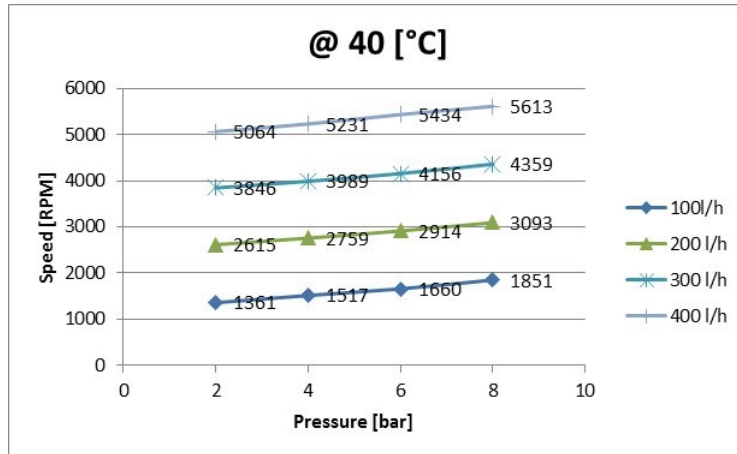
fig. 144: Pump characterization at 40 [°C]
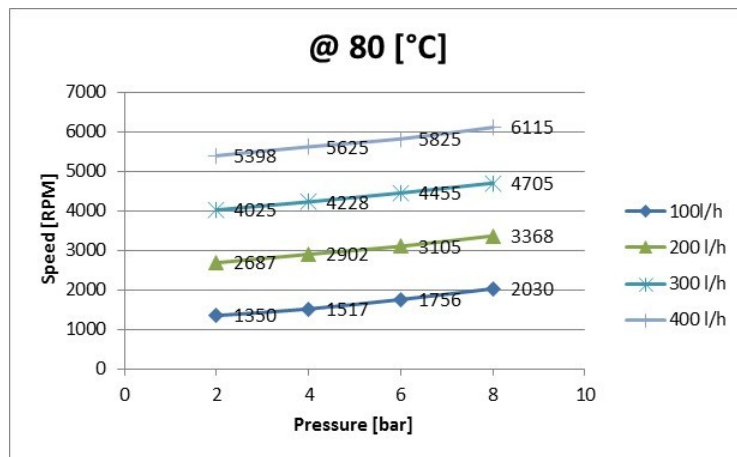
fig. 145: Pump characterization at 80 [°C]

During the test, also the A-phase current has been measured by an oscilloscope for the different pressure values. In fig. 146, the root mean square value of the A-phase current is reported when the temperature is equal to 40 [°C]. The same thing has been done in fig. 147, but in this case the diesel temperature is equal to 80 [°C]. From fig. 146 and fig. 147 it is possible to estimate the peak current value (it is equal to 40 [A], which is suitable for the electronic installed on the vehicle).
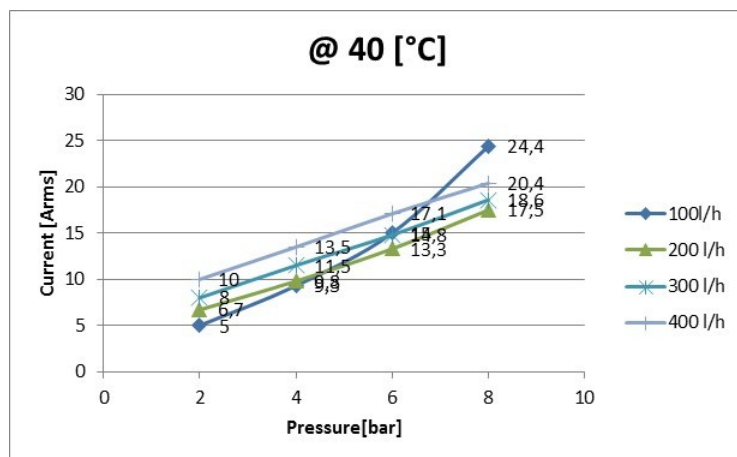
fig. 146: Current vs. pressure for different flowrates at 40 [°C]
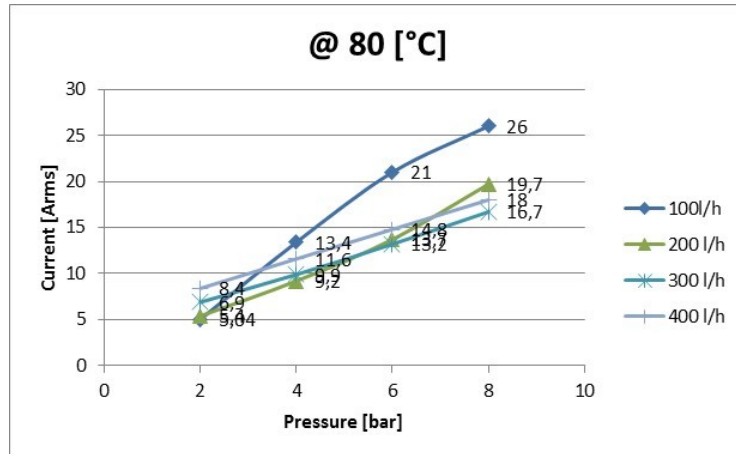
fig. 147: Current vs. pressure for different flowrates at 80 [°C]

Finally, at steady-state, when the MB control is on, also the currents i_d and i_q have been recorded, using the software ControlDesk.
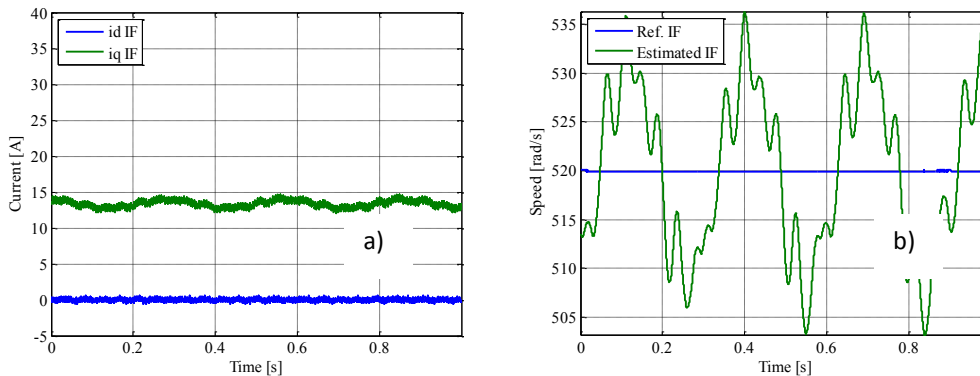
fig. 148: a) estimated i_{sd} and i_{sq} currents and b) estimated speed / IF starting - @ T = 40 [°C] – Δp = 4 [bar]
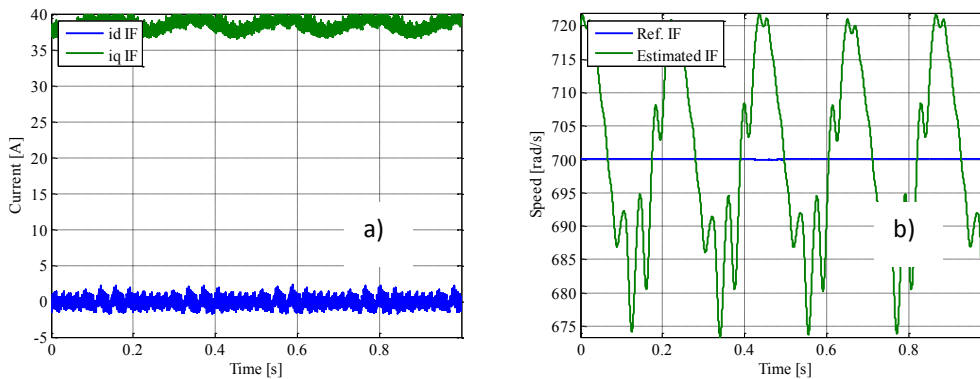
fig. 149: a) estimated i_{sd} and i_{sq} currents and b) estimated speed / IF starting - @ T = 40 [°C] – Δp = 8 [bar]

In fig. 148 and fig. 149 the IF acronym is used to indicate that the machine is moved using the IF control; then, there is the switching to MB control. From fig. 149, it is evident that the speed and the current i_{sq} have some oscillations in the neighbourhood of their references. The reason is on the pressure value, which was constant only for short periods during the test sessions. Concluding, the

experimental data obtained are equal to those obtained from other operators (such data are not reported for industrial reasons). This confirms the suitability of the MB control.

Now, it is important to test the performance during the starting. To do that, an inlet pressure different from zero must be set. The acceleration value used for carrying out the tests is:

➤ Acceleration: 2400 [rpm/s], that is 1005.3 [rad_e/s^2].

The tests have been performed in presence and in absence of a delta pressure (in particular, the delta pressure considered are Δp=0.35 [bar] and Δp=7.62 [bar]), in order to compare the performance of the developed sensorless control when two extreme operating points are analyzed.
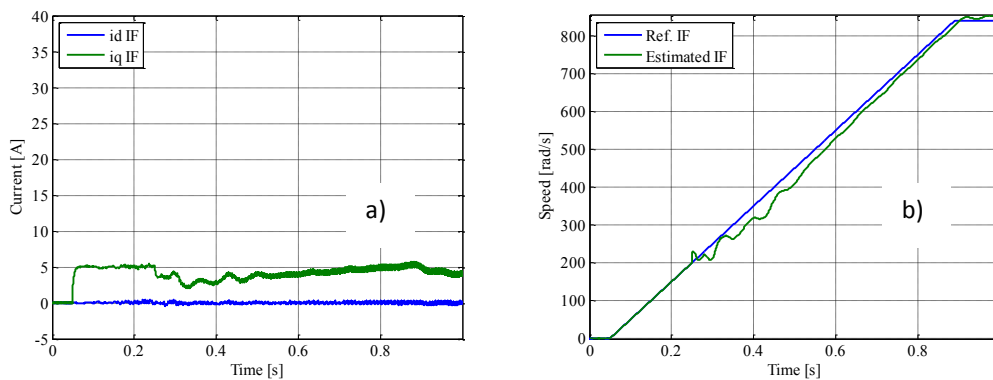
fig. 150: a) estimated i_{sd} and i_{sq} currents and b) estimated speed / IF starting - @ T = 40 [°C] – Δp = 0.35 [bar]
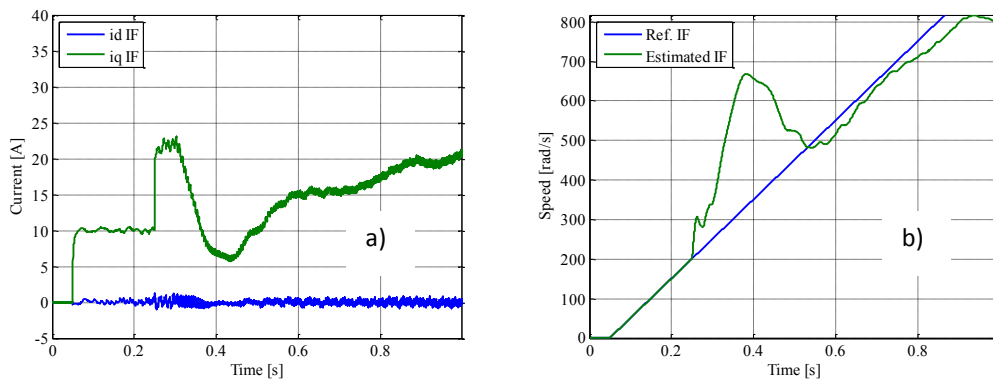
fig. 151: a) estimated i_{sd} and i_{sq} currents and b) estimated speed / IF starting - @ T = 40 [°C] – Δp = 7.62 [bar]

The starting current in the IF control has been imposed equal to 5 [A] and 10 [A], for Δp=0.35 [bar] and Δp=7.62 [bar], respectively, to highlight a particular behaviour of the test bench in simulating a pump output pressure level. Observing fig. 150 and fig. 151, it is possible to notice that the requested delta pressure is not respected at the starting time; in other words, at the starting time, the delta pressure is too low; then, it slowly increases with the pump speed. This is due to the difficulty of the tank valve to set an inlet pressure different from zero at the starting, when the flowrate is equal to zero. It is possible to set a reliable delta pressure value only when the flowrate is different from zero; that is, only at steady state. This consideration arises also by observing the fig. 149, where the i_{sq}

current is 40 [A] for a delta pressure equal to 8 [bar] ($\Delta p = 8[bar]$). In fig. 151 the i_{sq} does not reach the value 40 [A] although the requested delta pressure is set to about 8 [bar]; in fact, after the switching to MB control, the current increases, accelerating the pump quite easily but remaining well below the 40 [A] value. In fig. 152 and fig. 153, the performances of the HF control are shown.
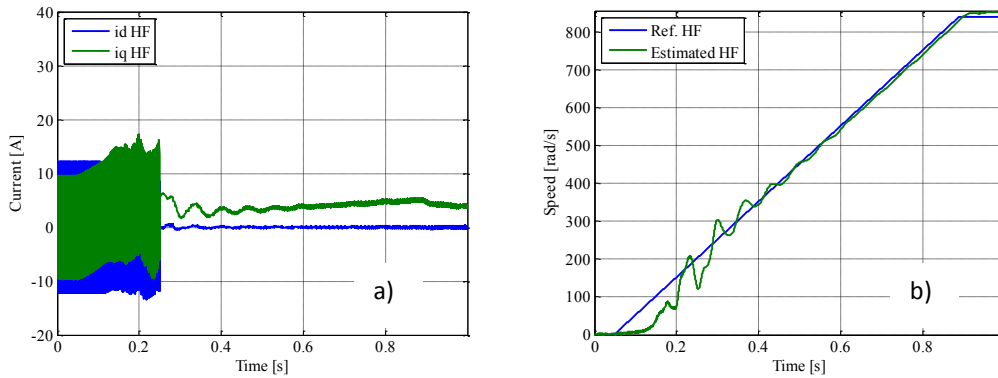
fig. 152: a) estimated i_{sd} and i_{sq} currents and b) estimated speed / HF starting - @ T = 40 [°C] – Δp = 0.35 [bar]
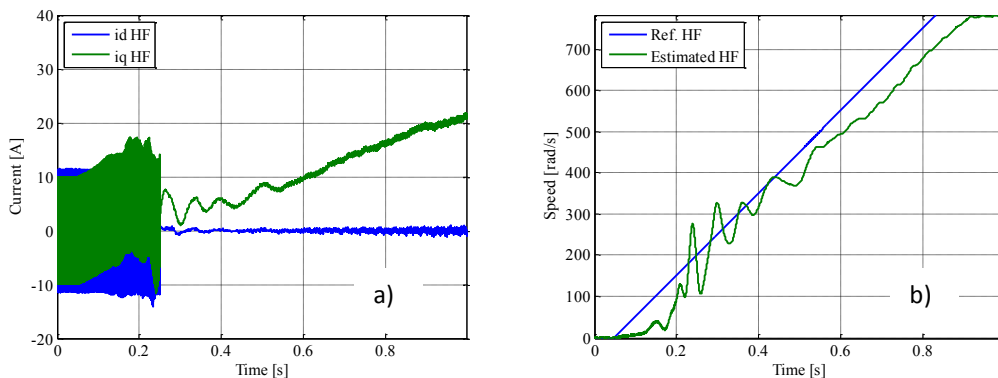
fig. 153: a) estimated i_{sd} and i_{sq} currents and b) estimated speed / HF starting - @ T = 40 [°C] – Δp = 7.62 [bar]

Here, the HF acronym is used to indicate that the switching is between the HF control and MB control; in other words, the hybrid control is used.

fig. 152 and fig. 153 show the same behaviour highlighted for the IF control; in the case the delta pressure is imposed to be 7.62 [bar], the speed transient takes much more time with respect to the speed transient recorded for the IF control. Concluding, the condition with a delta pressure different from zero at the starting must be simulated in another way; in addition, the IF control is preferable to HF control, because of the speed oscillations triggered by the HF control.

3.11. Starting test: delta pressure different from zero
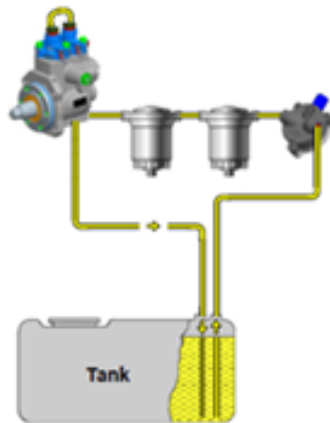
fig. 154: Test bench used to simulate an inlet pressure different from zero at the starting

From fig. 154, one can notice how the test bench has been modified in order to perform the tests with a delta pressure different from zero at the starting. The idea is to accelerate the mechanical pump until a certain delta pressure is reached; then, the sensorless control is turned off for a short period. After the off period is over, the sensorless control is turned on and the mechanical pump is accelerated again, until the previous value of reference speed. It must be noticed that only one more filter is necessary for the simulating a residual pressure at the starting. This kind of test has been called start-stop test and only the IF control has been used for the starting of the electrical machine. In addition, the tests have been carried out varying the turning off period of the sensorless control (IF control with switching to MB control).

Looking at fig. 155, when the sensorless control is turned off, both the reference voltages and the reference speed are set to zero; this is dead-time period in fig. 155. When the trigger signal becomes high, the control restarts and it has to be able to accelerate the pump until the earlier speed value is reached again, using the reference speed profile shown in fig. 155 (the speed profile is indicated with the name Reference speed in fig. 155), although the initial pressure is different from zero.
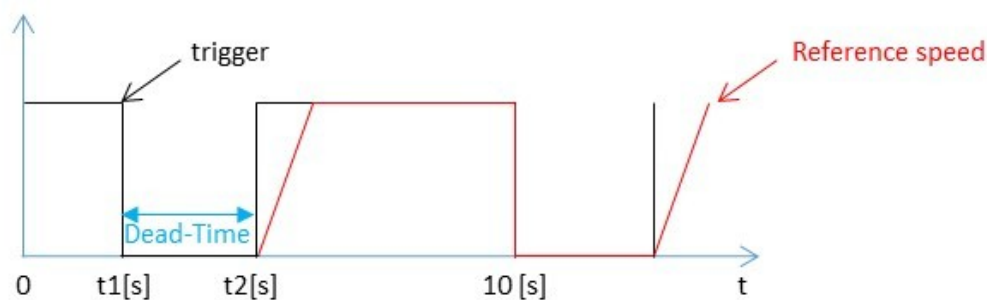
fig. 155: Speed profile used to simulate an inlet pressure different from zero at the starting (start-stop test)

Using an oscilloscope, the following measurements have been carried out:

- ➤ Delta pressure;
- ➤ Flowrate;
- ➤ Phase currents.

The experimental tests have been carried out for a fuel temperature equal to 20 [°C]. The acceleration rate has been imposed equal to 3200 [rpm/s], that is 1340 [rad_e/s^2].

The results are:

➤ Dead-Time equal to 0.1 [s]:
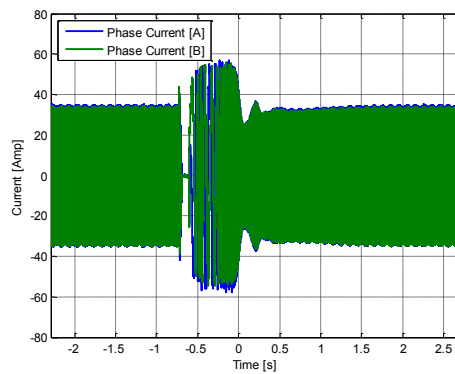
fig. 156: Phase currents during start-stop test for dead-time equal to 0.1 [s]
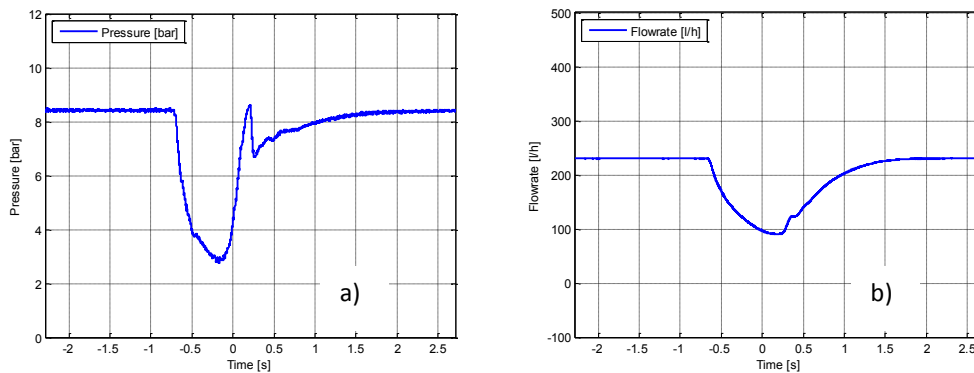
fig. 157: a) delta pressure and b) fuel flowrate during start-stop test for dead-time equal to 0.1 [s]

➢   Dead-Time equal to 0.2 [s]:
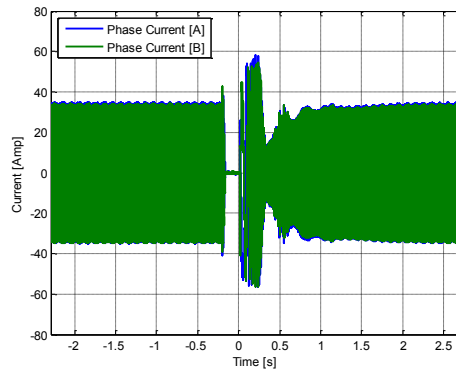
fig. 158: Phase currents during start-stop test for dead-time equal to 0.2 [s]
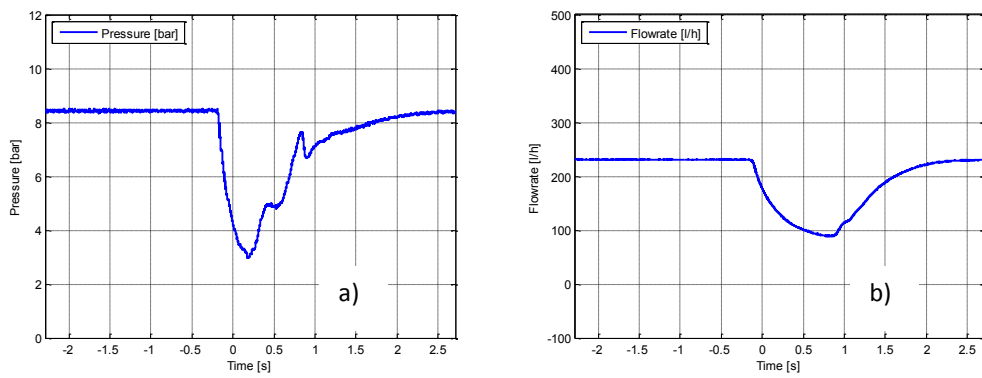
fig. 159: a) delta pressure and b) fuel flowrate during start-stop test for dead-time equal to 0.2 [s]

➢   Dead-Time equal to 0.3 [s]:
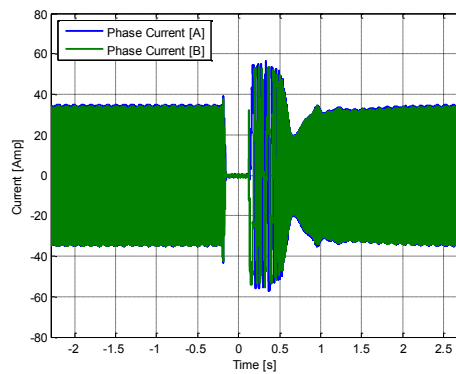
fig. 160: Phase currents during start-stop test for dead-time equal to 0.3 [s]
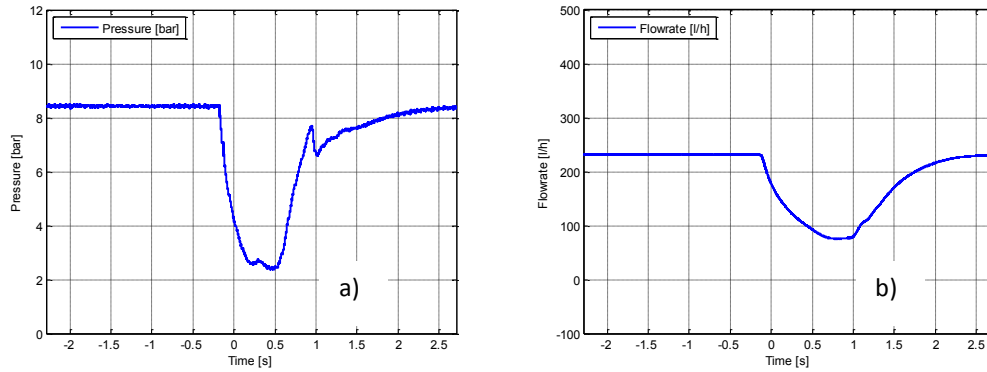
fig. 161: a) delta pressure and b) fuel flowrate during start-stop test for dead-time equal to 0.3 [s]

Considering the load torque reported in fig. 108 and remembering the torque constant, it is possible to predict the current level at starting as a function of the expected load level. This value should be equal to 17 [A] when the load torque equals 0.25 [Nm]. It is known that for a delta pressure equal to 8 [bar], the expected i_{sq} current is equal to 40 [A]. Consequently, making a ratio between currents and multiplying this ratio by the delta pressure 8 [bar], it is possible to calculate the delta pressure at the starting when the load torque equals to 0.25 [Nm]: this value is equal to about 3 [bar]. So, the load torque profile shown in fig. 108 corresponds to a delta pressure at the starting equal to 3 [bar]. In the experimental tests performed, this delta pressure 3 [bar] is present at the starting only when the dead-time is equal to 0.1 [s] and 0.2 [s].When the dead time is equal to 0.3 [s] the pressure decreases too much becoming well below 3 [bar].

Having created an operating condition in which a residual pressure is present at the starting, it is possible to conclude that the sensorless control (IF control with switching to MB control) is able to start the machine, although a delta pressure is present at the starting. The requirement about the maximum peak value of the current is not respected; in fact, the peak current value is higher than 40 [A], during the transition from the standstill to steady-state; then it becomes less than 40 [A]. This is due to the load torque and acceleration rate used during the experimental tests. One way to reduce the peak value is using an acceleration rate lower than 3200 [rpm/s].

CHAPTER IV

4. Development kit introduction

The IF control algorithm is used in the industry for its simplicity and effectiveness. In fact, thanks to IF control algorithm the machine can start in any operating condition, as proved in chapter III; moreover, it is less expensive in terms of computing time.

The IF control developed in chapter III has been translated in C, in order to implement it inside a microcontroller. The microcontroller will be inside a powerbox, which will be used to test the control algorithm, deleting the necessity of using DSpace. The main components inside the powerbox are the inverter and the microcontroller itself. Regarding the inverter, it is mandatory to remember its supplying limitations. In fact, most commercial inverters have power switches, which are not sized to dispose of large quantities of heat; that is a limiting factor for the phase current value. If the output power from the inverter increases, a suitable cooling system must be used. From the physical limitations for the inverter dimensions, it can be concluded that the high frequency injection cannot be used on the considered prototype due to the low saliency induced by saturation. This is an additional reason to use the IF control.

The implementation of the IF control code has been performed on the Texas Instruments development kit (fig. 162), because it represents a good tool to test the control algorithm in a safe way.

fig. 162: High voltage motor control

The development kit has the following features:

➢ 3-Phase inverter stage capable of sensorless and sensored field-oriented control (FOC) of high voltage PMSM motor and 1 [kW] maximum load in the default configuration;

➢ Power Factor Correction stage rated for 750 [W]. It takes rectified AC input (85-132 [V_{ac}] / 170-25 [V_{ac}]);

➢ AC Rectifier stage rated for 750 [W] power;

- ➢ eQEP input for encoder readings;
- ➢ Four PWM DAC to observe the system variables on an oscilloscope.
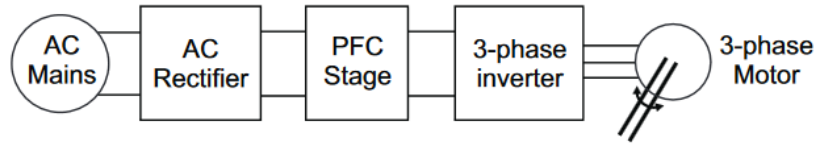
fig. 163: Block diagram for a typical motor drive system using power factor correction

The DSP is the TMS320F28335 (fig. 164), which has the following features:

- ➢ CPU frequency: 150 [MHz];
- ➢ 32 bit representation, single precision floating point;
- ➢ MAC operations (a = a + (b · c)): 32 x 32 MAC;
- ➢ Six ePWM channels;
- ➢ 12 bit ADC converter with sampling period equal to 80 [ns];
- ➢ JTAG module.

fig. 164: DSP TMS320F28335

Last, the equipped inverter is the Mitsubishi PS21765 (fig. 165). The inverter has the following features:

- ➢ Max. supply voltage (V_{cc}): 450 [V];
- ➢ IGBT collector current (I_c): 20 [A];
- ➢ Module case operation temperature: -20÷100 [°C].
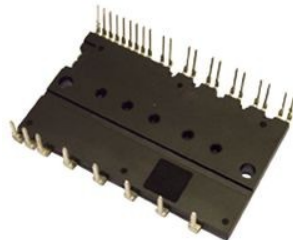
fig. 165: Inverter used in the development kit

The functional areas of the development kit are highlighted in fig. 166, where it is possible to see the position of the supply cables of the motor.
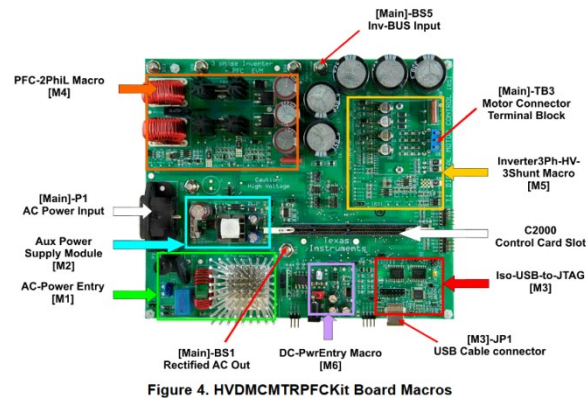
fig. 166: HVDMCMTRPFC Kit Board Macros

The inverter is present at the bottom side of the board, and it is attached directly to a blower, which is used only when the power transmitted is greater than 700 [W]. Because of the limitation of the development kit, Texas Instruments suggests using only certain types of motors, which are reported in fig. 167 [24]:

fig. 167: Motors sponsored by Texas Instruments

In particular, the motor chosen to carry out the experimental tests is the EMJ-04 Series Servo Motor, which is a surface permanent magnet motor. The main features of the motor are exposed in Table 33 [24]

Table 33: EMJ-04 PARAMETERS

Rated torque [Nm]	Rated Current [A_{rms}]	Rated Speed [rpm]	Number of poles	Momentum of inertia [kgm^2]	Phase resistance R_s [Ω] and inductance L_s [H]
1	8.1	3000	8	3e-5	R_s=2.23 L_s = 0.0066

The example code, developed by Texas Instruments, uses the resistance and the inductance values, which are in the datasheet of EMJ-04 (Table 33). In particular, those values are used for the sliding mode observer and for tuning the current and speed PIs.

4.1. DSP software flowrate
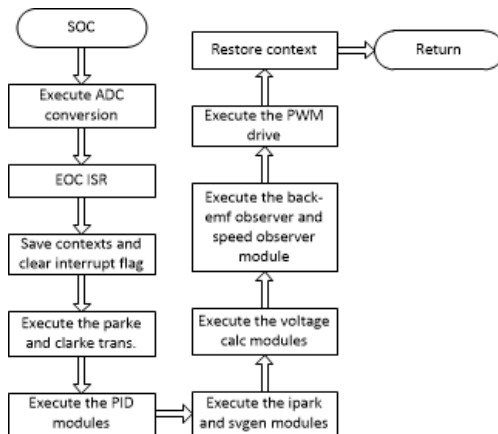
fig. 168: System software flowchart

Before starting the description of the control algorithm, it is necessary to describe the execution flow of the DSP.

As one can notice from fig. 168, the SOC (Start Of Conversion) signal enables the calculation routine and allows the last phase currents samples to get to the control. Once the ADC (Analog to Digital Converter) has done the conversion, the EOC (End Of Conversion) signal is generated. From here, the control algorithm is enabled, and it can calculate the reference voltages. From the reference voltages, the duty-cycle values are generated; consequently, the PWM module of the DSP is enabled [24]. It is mandatory to discern the SOC and EOC signal; the first is generated by the PWM module; while, the second is generated by the ADC, as one can see from fig. 169.
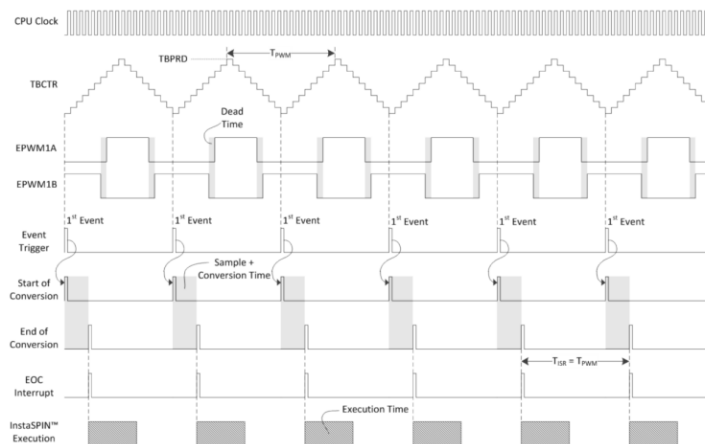
fig. 169: PWM Module

In particular from fig. 169, one can notice that the SOC signal is generated every time the counter reaches the zero value (TBCTR=0). In addition, in order to generate voltages with a low harmonic content, the counting method used is the up-down (fig. 169). The up-down counting method generates a triangular wave, which is symmetric to half PWM period (T_{PWM}) [25] [26]; so that, the three phase voltages will be centred each other.

In the end, in fig. 169 is highlighted how it is possible to avoid the overflow condition; to do that, the computing time must be in a single PWM period (shown in figure with the acronym T_{PWM}). When the overflow happens, the switching frequency is not constant and in the worst case the phase voltages will be equal to zero. Once the control has calculated the reference voltages, the duty-cycle values are generated. The logic used to generate the duty cycle values is shown in fig. 170, presented using the Simulink notation.
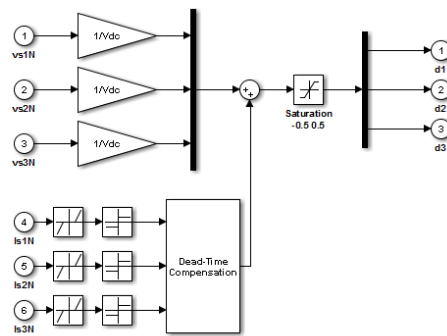
fig. 170: Duty-cycle generation

The duty-cycle values are stored inside the CMPA register. In this way the CA value (which is used for comparison purposes) shown in fig. 171 is automatically set. When the counter matches the CA value, the state of the power switches changes (e.g. from open to closed for the top A-switch and vice-versa for the bottom A-switch).
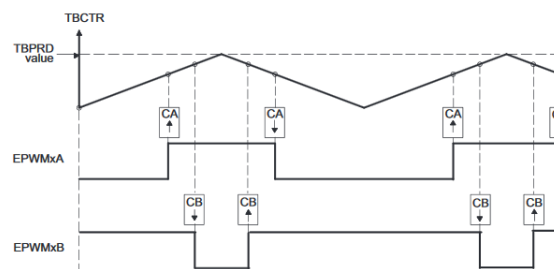
fig. 171: Up-Down count, Dual Edge Symmetric Waveform, with independent Modulation on EPWMxA and EPWMxB
- Complementary

Inside the PWM module, the term $0.5T_s$ is added (corresponding to the half PWM period value), in order to complete the duty-cycle for an entire PWM period. The C code, which summarizes all the things said, is:

```
EPwm1Regs.CMPA.half.CMPA = _IQmpy(v.d1,v.HalfPeriod)+v.HalfPeriod;
EPwm2Regs.CMPA.half.CMPA = _IQmpy(v.d2,v.HalfPeriod)+v.HalfPeriod;
EPwm3Regs.CMPA.half.CMPA = _IQmpy(v.d3,v.HalfPeriod)+v.HalfPeriod;
```

The duty-cycle generation takes into account the dead-time effect. In particular, the compensation takes place for phase current values higher than 0.1 [A] (Dead Zone block in fig. 170 regulates the compensation of the dead-time) and using the values of T_d (dead-time) and T_s (sampling period). To conclude the paragraph, the used sampling frequency and the dead-time value are reported:

➤ f_s (sampling frequency $1/T_s$) = 10 [kHz];

➤ Dead-time = 0.2 [μs];

4.2. Parameters identification

In order to verify that the machine in use has the resistance and inductance values equal to the values in the datasheet, an identification procedure has been launched; meanwhile, no inertia momentum identification procedure has been taken into account.

The resistance value will be calculated thanks to the eq. 123:

$$R_s = \frac{V_{dTesting} - U_{error}}{I_{DCph}}$$

eq. 123

Where $V_{dTesting}$ is the DC voltage applied to the motor along the d-axis (in fact, SpeedRef is set to zero; so that, the frequency will be zero); while I_{DCph} is the current corresponding to $V_{dTesting}$ voltage. The U_{error} is the voltage drop due to the dead-time; but, in the duty-cycle generation, there is the compensation of the dead-time itself (fig. 170). The used control scheme is reported in fig. 172:
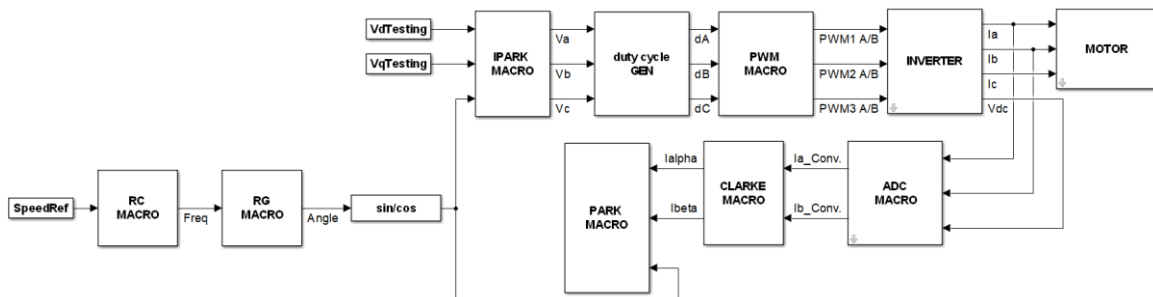
fig. 172: Block diagram of the control used for resistance measurement
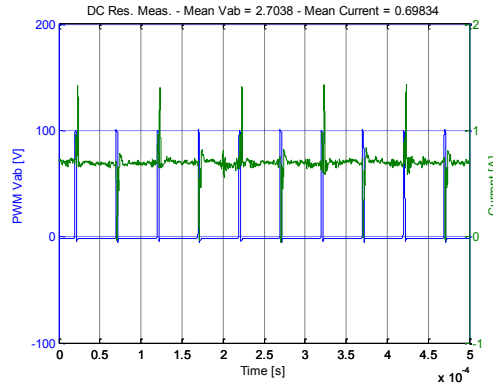
fig. 173: Voltage and current measured during the resistance measurement

From the identification process, the resistance value obtained is 2.23 [Ω], which is almost equal to the resistance reported in the datasheet. In addition, the resistance value measured has not been reported at the reference temperature (20 [°C]), because the identification process lasted only few seconds; consequently, no temperature rise may be appreciated in those conditions. The line voltage and the line current are shown in fig. 173 [27].

The inductance measurements took place without using the development kit; in fact, the nominal current of the motor is equal to 8 [A_{rms}] and in order to avoid interferences (which could damage the JTAG connection between the host and the development kit), it was preferred to measure the inductance using a DC power supply. In fact, all the electrical machines have a first order dynamic due to the resistance and inductance presence. For the case in analysis, the electrical time constant is equal to 3 [ms] and this allows to use a DC power supply, without asking to it any particular requirements (in particular, an high rise-time for the applied voltage).
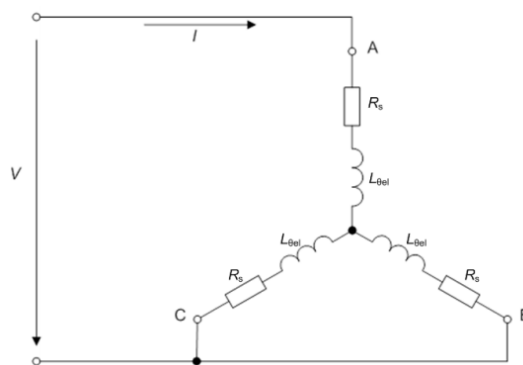
fig. 174: Inductance measurement setup

To conduct the experiment, the motor must be connected as shown in fig. 174; that is, the B and C phases must be short-circuited each other, and the DC voltage must be applied between the A-phase and the B and C terminals. The synchronous inductances of surface mounted permanent magnet motor (SMPM) are almost equal, because the permanent magnets are surface mounted and reluctance

is the same in every position, that is $\mu_{PM} \approx \mu_{AIR} \rightarrow L_d \approx L_q$, where μ_{PM} is the relative permeability of the permanent magnet, and μ_{AIR} is the relative permeability of the air. In practice, magnetic circuits are subjected to saturation as the current increases. If the machine was anisotropic, the L_q would decrease, resulting in higher I_q values. Meanwhile, the saturation along the d-axis rarely occurs, since the I_d current value is maintained to zero or negative value (demagnetizing); consequently, the decreasing of L_d is neglected [27]. On the basis of fig. 174, when the rotor is aligned with A-phase and locked, then the current response follows a first order dynamic, similar to that a RL circuit:

$$i_d = \frac{V}{R}(1 - e^{-\frac{t}{\tau}})$$

eq. 124

where τ is the time constant of a RL:

$$\tau = \frac{L}{R}$$

eq. 125

In particular, R is equal to $(3/2)R_s$. After measuring τ, the inductance L_d can be calculated (eq. 126):

$$L_d = \frac{2}{3}\tau R_s$$

eq. 126
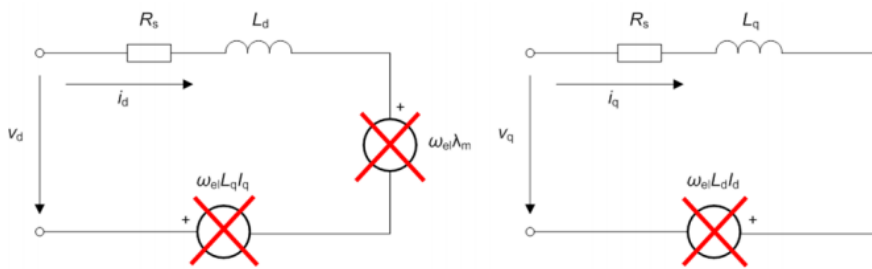
fig. 175: Equivalent phase model of PMSM in d/q axis for a locked rotor shaft

If the machine was anisotropic, the same method could also be applied to L_q, but the rotor must be locked at 90° electrical [27]. The DC voltage and the current response measured during the L_d measurement are (fig. 176):
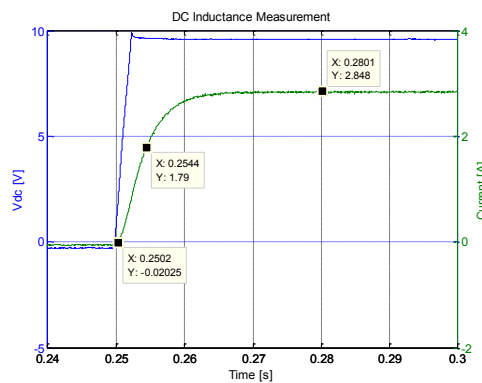
fig. 176: Current response to a DC voltage applied between A phase and BC phases short-circuited

The value of τ is 0.0042 [ms]; so, the L_d inductance is equal to 6.4 [mH]. The same value is reported in the datasheet of the motor.

4.3. PI tuning

The PI structure of Texas Instruments has been used during the test, both for the current regulation loop and speed regulation loop. The PI Texas Instruments has the structure (fig. 177):
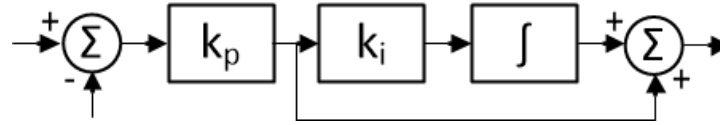
fig. 177: Texas Instruments PI structure

The rules to be used, in order to tune the current PI coefficients, are:

$$k_{i\_current} = \frac{R}{L} \cdot T_s \qquad \text{eq. 127}$$

$$k_{p\_current} = L \cdot Bandwidth \qquad \text{eq. 128}$$

So, in the current regulation loop, the $k_{i\_current}$ value creates a zero, that cancels the pole of the motor's stator and can easily be calculated. The $k_{p\_current}$ gain adjusts the bandwidth of the current controller-motor system.

For the speed loop regulation, the loop gain has the transfer function stated in eq. 129:

$$GH(s) = \frac{k \cdot k_{p_{speed}} \cdot k_{i_{speed}}(1 + \frac{s}{k_{i\_speed}})}{s^2(1 + \tau s)} \qquad \text{eq. 129}$$

where k is equal to (eq. 130):

$$k = \frac{k_T}{J} \qquad \text{eq. 130}$$

k_T is the torque constant, J is the inertia momentum and τ is the time constant of the velocity low pass filter. Last, it is supposed that the current control loop has a unitary closed-loop transfer function; so, it is not present in the expression of eq. 129.

In order to tune the speed PI parameters, it is needed to assume that the zero dB frequency occurs somewhere between the zero at s = k_{i_speed} and the two nonzero poles in the denominator of the expression; the Bode plot should look something like this:
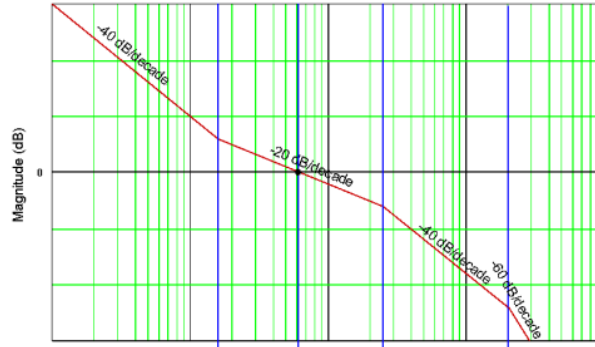
fig. 178: Ideal Bode plot of speed loop

So, for stability reasons, the system Bode diagram must pass the 0 dB axis, having a slope equal to -20 dB/decade. In order to achieve that, the following assumptions are necessary (eq. 131 and eq. 132):

$$\omega_{unity\_gain} = \delta \cdot k_{i\_speed} \qquad \text{eq. 131}$$

$$\frac{1}{\tau} = \delta \cdot \omega_{unity\_gain} \qquad \text{eq. 132}$$

Solving for k_{i_speed}, the eq. 133 is obtained:

$$k_{i\_speed} = \frac{1}{\delta^2 \tau} \cdot T_s \qquad \text{eq. 133}$$

The δ value must be greater than 1 (optimum values are between 2.5 and 4). In the end, forcing a unitary module at ω_{unity_gain}, one can obtain the k_{p_speed} expression (eq. 134):

$$k_{p\_speed} = \frac{1}{\delta \cdot k \cdot \tau} \qquad \text{eq. 134}$$

So, it is necessary to define two meaningful system parameters: the bandwidth of the current controller and the damping coefficient of the speed loop. Once these are selected, the four PI coefficients are calculated automatically [25].

To be noticed that it is necessary to use a low-pass filter for the estimated speed, because the inertia momentum is low, and the torque ripple (which causes the speed oscillations), can be dangerous for the control.

4.4. Description of the control and experimental results

The test bench used to test the C code of the IF control algorithm is shown in fig. 179. The test bench is composed of two Texas Instruments development kits and two ESTUN EMJ-04 servomotors. One motor is vector speed controlled; while, the other one is vector current controlled. In order to avoid the triggering of limit cycles during the test sessions, the DC voltage has been set equal to 250 [V].

fig. 179: Test bench for testing C code of sensorless control

To evaluate the sensorless control performances, the following quantities have been recorded:

➢ Speed Reference;

➢ Speed measured by the encoder;

➢ Estimated Angle;

➢ Angle measured by the encoder.

It is mandatory to remember that the DACs (which are in the board) can show only two quantities for a single experiment (e.g., the estimated angle and the angle measured by the encoder).

The Simulink control scheme is shown in fig. 180. The main blocks are:

➢ SPEED OBS. MACRO;

➢ BACK-EMF OBS. MACRO;

➢ SWITCH MACRO.
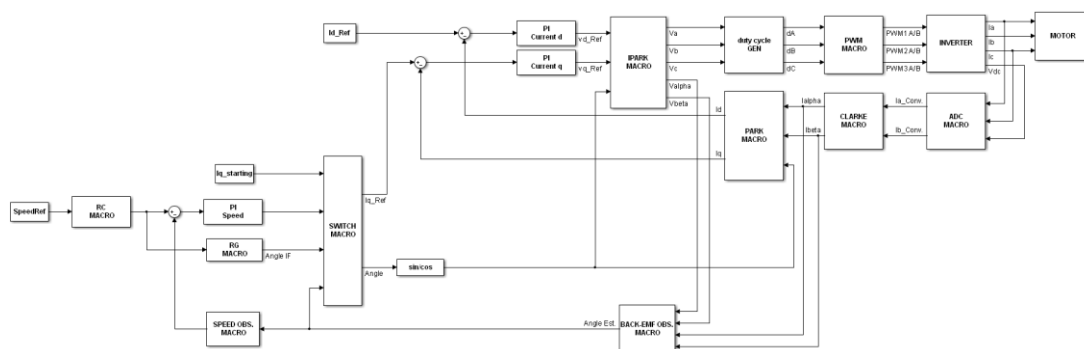
fig. 180: Scheme of the control implemented in the DSP TMS320F28335

For these macros, the Simulink scheme is defined; then, the appropriate C code is written. For the discretization process, it has been used the backward Euler method; that is, the conversion from the continuous time domain to the discrete time domain is expressed by eq. 135:

$$s = \frac{1 - z^{-1}}{T_s}$$

eq. 135

➢ SPEED OBS. MACRO:
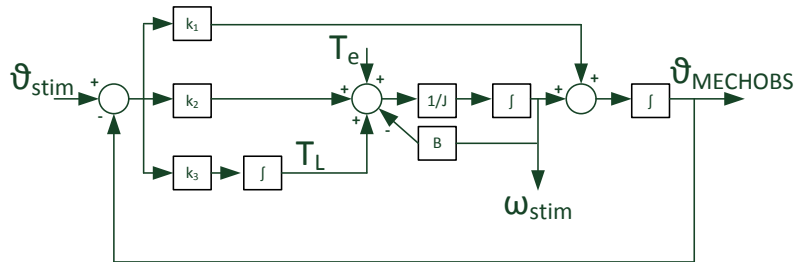
fig. 181: Speed observer implemented in the DSP TMS320F28335

The mechanical observer has been introduced in chapter III, with the main relations used to tune it. The bandwidth has been set to 40 [rad/s]. In order to make the control robust, the speed in output from the speed observer has been filtered by a low pass-filter. The C code of the speed observer is:

SPEED OBS. MACRO - C CODE

```
// Parameters
typedef struct { _iq ThetaIN; // Input: Angle from back-emf observer
         _iq ThetaEst;       // Angle estimated from the speed observer
         _iq ThetaErr;            // Difference between the angle estimated by the back-emf observer and speed
observer
         _iq ThetaErrD;     // Derivative action
         _iq ThetaErrP;     // Proportional action
         _iq ThetaErrI;     // Integral action
         _iq Tor;           // Difference between the load torque and electromagnetic torque
         _iq Speed1;        // Output from the first integrator
         _iq Speed2;        // Output from the second integrator
         _iq Ts;            // Sample time
         _iq k1;            // Derivative coeff.
         _iq k2;           // Proportional coeff.
         _iq k3;           // Integral coeff.
         _iq J;            // Inertia
         _iq isq;          // Current isq
         _iq kT;           // Torque constant
         _iq np;           // number of pole pairs
                        }SPEEDOBS;
// Initialization structure
#define SPEEDOBS_DEFAULTS  {0,0,0,0,0,0,0,0,0,0,0,0,0,0,0,0,0}
// Macro SPEED OBSERVER
#define SPEEDOBS_MACRO(v)
   v.ThetaErr=v.ThetaIN-v.ThetaEst;
   v.ThetaErrI=v.ThetaErrI+_IQmpy(_IQmpy(v.k3,v.Ts),v.ThetaErr);
   v.ThetaErrP=_IQmpy(v.k2,v.ThetaErr);
   v.ThetaErrD=_IQmpy(v.k1,v.ThetaErr);
   v.Tor=v.ThetaErrP+v.ThetaErrI+_IQmpy(v.kT,v.isq);
   v.Speed1=v.Speed1+_IQmpy(v.Tor,_IQdiv(v.Ts,_IQmpy(v.np,v.J)));
   v.Speed2=v.Speed1+v.ThetaErrD;
   v.ThetaEst=_IQmpy(v.Ts,v.Speed2)+v.ThetaEst;
```

The discrete equation of the used low-pass filter is (eq. 136):

$$\omega_f(k) = K2 \cdot \omega_f(k-1) + K3 \cdot \omega(k)$$

eq. 136

where the filter coefficients have the expressions stated in eq. 137:

$$K2 = \frac{1}{1+T_s \cdot 2\pi \cdot 5}$$

$$K3 = 1 - K2$$

eq. 137

Knowing the fundamental parameters of the low pass filter (eq. 136 and eq. 137), the filter bandwidth has been set to 5 [Hz].

➢ BACK-EMF OBS. MACRO:
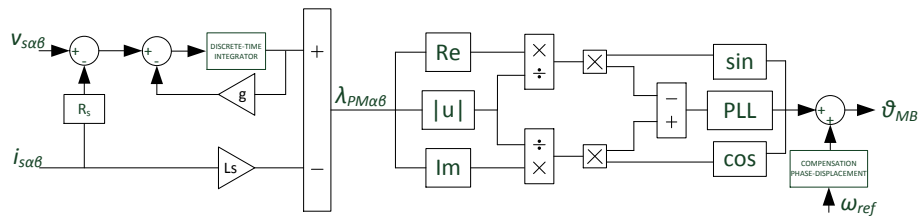
fig. 182: BACK-EMF observer implemented inside DSP

The back-EMF observer has been introduced in chapter III. Also in this case the *g* value has been set to 20 [rad/s]. The compensation of the phase displacement due to low-pass filter, used as integrator, is accomplished directly on the estimated angle.

BACK-EMF MACRO - C CODE

```c
// Parameters
typedef struct { _iq VAlpha;            // Input: Alpha Voltage
                 _iq VBeta;             // Input: Beta Voltage
                 _iq PreFluxAlpha;      // Difference Valpha - RIalpha
                 _iq PreFluxBeta;       // Difference Vbeta - RIbeta
                 _iq R;                 // Input: Resistance
                 _iq IAlpha;            // Input: Alpha Current
                 _iq IBeta;             // Input: Beta Current
                 _iq FluxTotAlpha;      // Stator flux Alpha
                 _iq FluxTotBeta;       // Stator flux Beta
                 _iq g;                 // Input: g value
                 _iq L;                 // Input: Inductance value
                 _iq PsiPMAlpha;        // Rotor flux Alpha
                 _iq PsiPMBeta;         // Rotor flux Beta
                 _iq PsiPM;             // Magnitude of rotor flux
                 _iq cosTheta;          // cosTheta
                 _iq sinTheta;          // sinTheta
                 _iq Err;               // Input PLL
                 _iq ErrI;              // Integrator Action
                 _iq Speed;             // Electrical Speed from PLL
                 _iq kp;                // kp coeff. in PLL
                 _iq ki;                // ki coeff. in PLL
                 _iq Ts;                // Sample time
                 _iq Theta;             // Absolute angle
                 _iq ThetaPU;           // PU angle
                 _iq Out;               // Output: PU angle
                 _iq ThetaComp;         // Angle compensation due to g
                 _iq OmegaRif;          // Input: Reference speed
                 _iq CompYes;           // Input: Compensation g on/off
                                       } BACKEMFOBS;
// Initialization structure
#define BACKEMFOBS_DEFAULTS {0,0,0,0,0,0,0,0,0,0,0,0,0,0,0,0,0,0,0,0,0,0,0,0,0,0,0,0}
// Macro BACK-EMF OBSERVER
#define BACKEMFOBS_MACRO(v)

v.PreFluxAlpha=v.VAlpha-_IQmpy(v.R,v.IAlpha);
v.PreFluxBeta=v.VBeta-_IQmpy(v.R,v.IBeta);
v.FluxTotAlpha=_IQdiv((_IQmpy(v.PreFluxAlpha,v.Ts)+v.FluxTotAlpha),(1+_IQmpy(v.g,v.Ts)));
v.FluxTotBeta=_IQdiv((_IQmpy(v.PreFluxBeta,v.Ts)+v.FluxTotBeta),(1+_IQmpy(v.g,v.Ts)));
v.ThetaComp=_IQ(0.25)-_IQatan2PU(v.OmegaRif,v.g);
v.PsiPMAlpha = v.FluxTotAlpha - _IQmpy(v.L,v.IAlpha);

v.PsiPMBeta = v.FluxTotBeta - _IQmpy(v.L,v.IBeta);
            v.PsiPM=_IQmag(v.PsiPMAlpha,v.PsiPMBeta);
v.cosTheta=_IQdiv(v.PsiPMAlpha,v.PsiPM);
v.sinTheta=_IQdiv(v.PsiPMBeta,v.PsiPM);
v.Err=_IQmpy(v.sinTheta,_IQcosPU(v.ThetaPU))-_IQmpy(v.cosTheta,_IQsinPU(v.ThetaPU));
v.ErrI=v.ErrI+_IQmpy(_IQmpy(v.Err,v.Ts),v.ki);
v.Speed=_IQmpy(v.Err,v.kp) + v.ErrI;
 v.Theta=v.Theta+_IQmpy(v.Speed,v.Ts);
v.ThetaPU=_IQatan2PU(_IQsin(v.Theta),_IQcos(v.Theta));
if (v.CompYes != 0)
   {
     v.Out=v.ThetaPU+_IQmpy(v.ThetaComp,v.CompYes)
     if (v.Out>_IQ(1))
         {
             v.Out-=_IQ(1);
         }
     else if (v.Out<_IQ(0))
          {
              v.Out+=_IQ(1);
          }
   }
else
    {
      v.Out=v.ThetaPU;
    }
v.Out=_IQsat(v.Out,1,0);
```
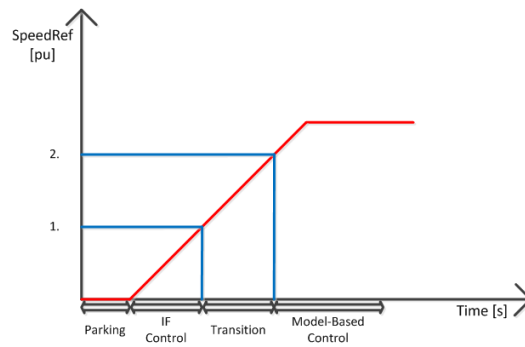
fig. 183: Switching logic dynamic

From fig. 183, it is possible to see the first step performed by the control algorithm; that is, the parking phase. During this phase, the control tries to align the d-axis along the A-phase axis of the machine. Once this is achieved (it is not possible to know if the parking has happened successfully), this information is used by the back-EMF observer for a better estimation of the rotor angle. It is mandatory to say that the parking phase is not necessary, because of the switching logic used inside the control algorithm. In fact, the transition from the IF control to model-based control is realized using a first order lag compensator, which has the expression (in the continuous time domain) stated in eq. 138:

$$First \ order \ lag \ compensator = \frac{1}{1 + T_f} \qquad \text{eq. 138}$$

where T_f is the filter time constant, which is equal to 0.04 [s]. In order to carry out the switching to the model based control in the best way, the filter input must be equal to zero, while the initial value must be equal to the difference between ϑ_{IF} and ϑ_{MB}; such difference must be calculated when the switching happens (that is, when SpeedRef is equal to the value reported by 1 in fig. 183). During the transition from IF control to model-based control, the speed regulator is activated and the I_q reference value switches slowly from $I_{qstarting}$ (value used by the IF control) to the value demanded by the speed regulator, according to the dynamic of the first order lag compensator. When SpeedRef is higher than the value reported by 2 in fig. 183, the control is totally model-based, and the initial condition of the filter is set to zero. For sake of simplicity, the switching logic is activated only for positive speed slope; if the reference speed is set to zero, the control disables the PI regulators (current and speed), and also the angle used for the transformations is set to zero. Concerning the mechanical dynamic of the machine and considering the phase current values, it is possible to make the switching from IF control to MB control directly, without using a lag compensator.

SWITCH MACRO - C CODE

```c
// Parameters
typedef struct {
    _iq ThetaObs;           // Input: Observer Angle
    _iq ThetaIF;            // Input: IF Angle
    _iq Speed;              // Input: Speed Reference (pu)
    _iq Ts;                 // Input Sampling Time
    Uint32 count;           // Generic variable
    _iq SpeedSwitchPN;      // Input: Positive/Negative speed slope
    _iq CLSwitch;           // Output: Closed switch for speed regulator
    _iq SpeedLow;           // Input: Low limit of speed
    _iq SpeedHigh;          // Input: High limit of speed
    _iq Theta;              // Output: Angle
    _iq ThetaComp;          // Initial Condition filter for Theta Transition
    _iq Tc;                 // Input: Time constant lag filter
    _iq IqComp;             // Initial Condition filter for Current q Transition
    _iq IqIF;               // Input: Current starting
    _iq IqSpd;              // Input: Current demanded by the speed regulator
    _iq IqRef;              // Input: Reference Current Iq
    } SWITCH_IF;
// Initialization structure
#define SWITCH_IF_DEFAULTS   { 0,0,0,0,0,0,0,0,0,0,0,0,0,0,0,0}
// Macro SWITCH
#define SWITCH_IF_MACRO(v)
if (v.SpeedSwitchPN>_IQ(0))
    {
        if (v.Speed<=v.SpeedLow)
            {
                v.Theta=v.ThetaIF;
                v.CLSwitch=_IQ(0);
                v.count=_IQ(0);
                v.IqRef=v.IqIF;
            v.ThetaComp=0;
            v.IqComp=0;
            }
        else if (v.Speed>v.SpeedHigh)
            {
                v.Theta=v.ThetaObs;
                v.CLSwitch= _IQ(2);
                v.count= _IQ(0);
                v.IqRef=v.IqSpd;
            v.ThetaComp=0;
            v.IqComp=0;
            }
            else
                {
                    if (v.count == _IQ(0))
                        {
                            v.count=_IQ(1);
                            v.ThetaComp = v.ThetaIF - v.ThetaObs;
                            v.IqComp = v.IqIF - v.IqSpd;
                            v.CLSwitch = _IQ(1);
                        }
                    v.Theta=v.ThetaObs+v.ThetaComp;
                    v.IqRef=_IQsat(v.IqSpd+v.IqComp,0.8,-0.8);
                    v.ThetaComp=_IQdiv(v.ThetaComp,(1+_IQdiv(v.Ts,v.Tc)));
                v.IqComp=_IQdiv(v.IqComp,(1+_IQdiv(v.Ts,v.Tc)));
                    if (v.Theta>_IQ(1))
                        {
                            v.Theta-=_IQ(1);
                        }
                    else if (v.Theta<_IQ(0))
                        {
                            v.Theta+=_IQ(1);
                        }
                }
        }
else
    {
        v.Theta=0;
        v.IqRef=0;
        v.CLSwitch=0;
        v.count=0;
    }
```

In order to test the effectiveness of the control algorithm used, a starting test under load has been performed. The load torque has been set to 0.5 [Nm]. In fig. 184 are reported the waveforms of:

➢ Reference speed and speed measured by the encoder; both have been recorded using the DAC inside the Texas Instruments board;

➢ A-phase current, measured by a current probe. At the starting, the current value has been set equal to 3 [A].
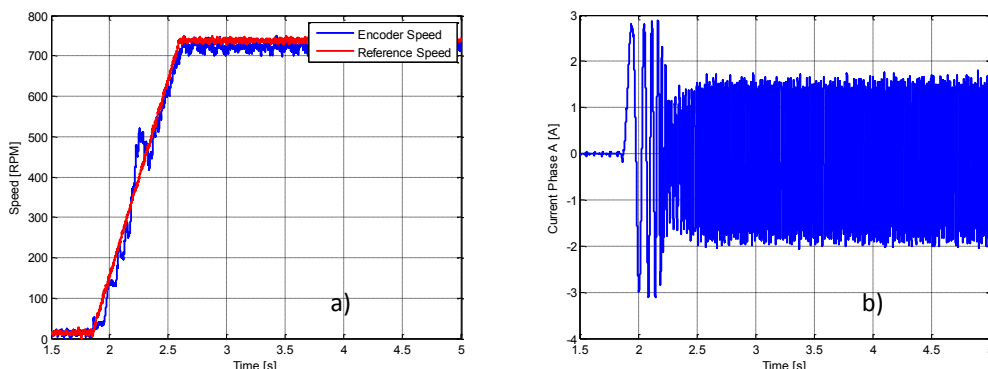
fig. 184: a) Speed and b) A-phase current of the motor, recorded during the test session

4.5. Side effects due to the current sampling: possible solutions

The delay due to the current sampling process may generate a bad estimation of the rotor position, above all, when the ratio between the sampling frequency and electrical frequency is low.

During the test sessions, two different compensation methods are used, in order to investigate which is the best to use inside the DSP:

1. Inserting a delay on the reference voltages, used by the back-EMF observer:
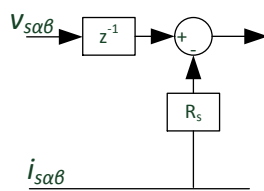
fig. 185: First method used to compensate the error estimation due to the current sampling process

2. Modifying the reference voltages in output from current PIs:
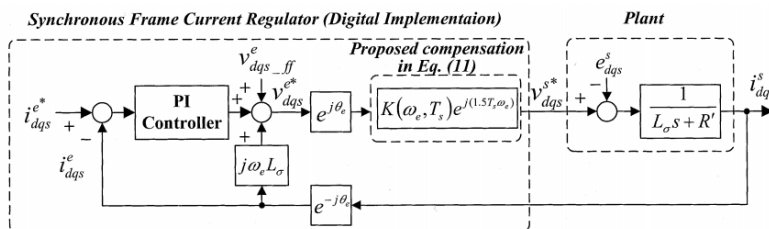
fig. 186: Second method used to compensate the error estimation due to the current sampling process

The effectiveness of the first method has been proved in chapter III. The second method can be explained, seeing the fig. 187.
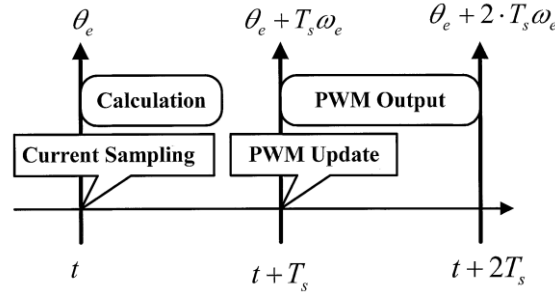
fig. 187: Time sequence of current sampling, calculation and PWM output

As shown in fig. 187, one sampling time is delayed during the execution of the control algorithm. In addition, the PWM output is refreshed after one sampling time at $(t + T_s)$ and the PWM output is activated during the next period from $(t + T_s)$ to $(t + 2T_s)$. With the time sequence of fig. 187, the synchronous reference frame rotates and the trace of a voltage output moves, as shown in fig. 188. Under the assumption that the synchronous frequency ω_e is constant during the time delay, the stator referred voltage reference for the PWM generation can be derived by averaging the dotted trace of voltage vector shown in fig. 188 [28].
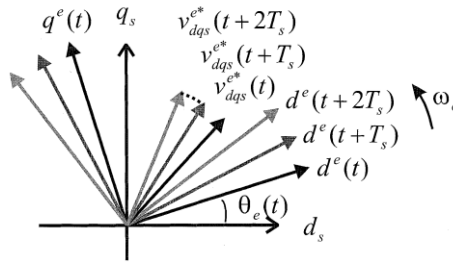
fig. 188: Rotation of the synchronous reference frame corresponding to the time sequence

So that, in the ideal case the voltage is (eq. 139):

$$v_{dqs}^{s*} = v_{dqs}^{e*} e^{j\vartheta_e}$$ eq. 139

while, in the time-delayed case the voltage is (eq. 140):

$$v_{dqs\_digital}^{s*} = \frac{2}{\omega_e T_s} \sin\left(\frac{\omega_e T_s}{2}\right) v_{dqs}^{e*} e^{j(1.5T_s\omega_e + \vartheta_e)} = K e^{j(1.5T_s\omega_e + \vartheta_e)} v_{dqs}^{e*}$$ eq. 140

Finally the error is (eq. 141):

$$f_{error} = \frac{e^{j(-1.5T_s\omega_e)}}{K}$$ eq. 141

So, the error in the voltage output caused by the frame rotation can be summarized as follows:

1. The magnitude of the voltage vector is changed by a scalar value 1/K which is larger than a single unit;

2. The phase of the voltage vector is delayed by the rotating angle of the reference frame during one-and-a-half sampling period.

From the error equation, a compensation method for the time delay in the full-digital synchronous current regulator can be derived using the inverse function of the error (eq. 142) [28]:

$$f_c = \frac{1}{f_{error}}$$

eq. 142

The advantages of these compensation methods have been tested at steady-state, in the case the rotor speed is equal to 900 [rpm] when the load torque variation is in the range -1 [Nm] ÷ 1 [Nm]. So, for a speed value equal to 900 [rpm], the error angle should be about 3 [deg.], according to eq. 141.
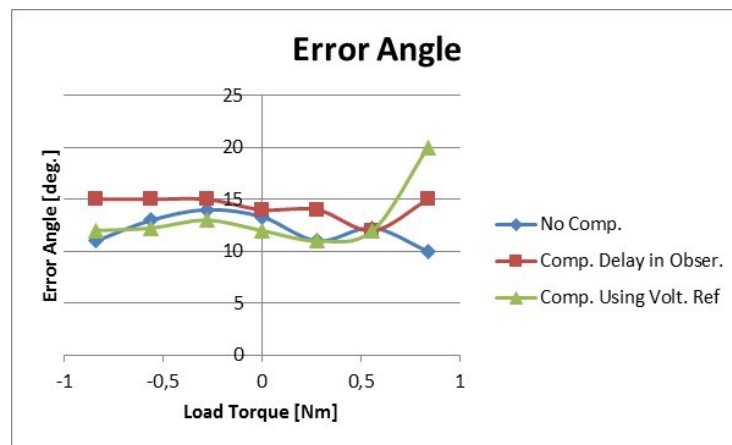
fig. 189: Error angle using: No compensation (blue line); compensation in observer (red line); compensation using reference voltages modified (green line).

From fig. 189, it is possible to see the waveforms of the estimation error in all the cases. Attention must be paid to the values themselves; in fact, they are close each other. Considering the magnitude of the errors shown in fig. 189, they are higher than 3 [deg.]. An analysis of the estimation error of the MB observer at steady-state in chapter III has demonstrated the limiting nature of the MB observer itself; in fact, the estimation error was higher (considering only the magnitude and neglecting the sign) than 10 [deg.] in some cases, although the action of the compensation inside the observer structure. In addition, another negative factor must be mentioned about the error angle shown in fig. 189; that is, during the tests, the DAC were affected by the high DC supply voltage, which was not almost stable; so, it is possible that the noise had affected the measurements, although an analog low pass filter had been used in input to eQEP module. So, the error angle shown in fig. 189 could be affected by noise.

Concluding, although the error angle is not negligible (as it has been verified during the experimental tests performed for the analysis described), the speed response is almost acceptable; also, the control is stable. So, the compensation algorithms are not so important when the ratio between the sampling frequency and the electrical frequency is higher than 10. Considering the maximum mechanical speed (2700 [rpm]), the C code, developed for compensating the delay related to the current sampling process, is unnecessary. This leads to a saving in the computation time.

CONCLUSIONS

In this work it was faced a feasibility study on the possibility to use an electric machine into a diesel injection system in order to move a mechanical pump.

At first, several electrical machines typologies have been considered. In particular surface permanent magnet motors and reluctance motors. It has been shown that, for the type of application, reluctance machines are an expensive alternative; for this reason, the only solution is to use a surface permanent magnet motor. In addition, the reluctance machines have an excessive weight. A great task reached in the chapter I was the realization of the analytic design tool. In particular, during the realization of the analytic design tool, it has been proved that the IPM appearance of the prototype, designed by Bosch, does not create a magnetic anisotropy, except for the cases where the phase current values are high (so, the prototype acts more like an SPM motor). The realization of a test bench has permitted to test the electrical machines realized, in order to evaluate the efficiency in all operating points of interest. In addition, using the test bench, it has been possible to measure the electrical and mechanical parameters. Then, the sensorless control has been developed, using a DSpace system. In particular two starting algorithms have been developed; that is, the IF control (current-frequency control) and the HF control (high-frequency control). Both the starting algorithms have been tested. In particular, from the experimental data given by the real test bench (which is composed of the gear pump, fuel filter and high pressure pump), it has been possible to conclude that for this purpose, the IF starting control algorithm is sufficient. The HF control suffers because of high phase current values used to exploit the anisotropy of the machine. As last step, the sensorless control has been implemented inside a DSP, in order to realize a powerbox. The powerbox will be used in the real test bench, deleting the necessity of using the DSpace system.

Concluding, the layout of the machine seems not be further improvable from a point of view of cost and weight; an improvement could be to use a solution to exasperate the anisotropy. Concerning the sensorless control algorithm, it could be improved using a different electronics, which permits to use high current values. In fact, in this way, it would be possible to use the HF control algorithm. On the basis of the two last observations, if the machine was anisotropic, it would be possible to use the HF control. In this way would be also possible to keep the control of the electromagnetic torque from the standstill until the steady-state, avoiding the mechanical oscillations, which are present when the switching from IF control to model-based control happens.

APPENDIX

1. SPM optimization MatLab Code

In this paragraph is shown the MatLab code for the optimization of SPM motors. The data in input are:

- ➤ Remanence of PMs;
- ➤ Stator tooth width and height;
- ➤ Span and height of PMs;
- ➤ x.

In particular, the MatLab function, which does the evaluation work, is called SPM.

So, SPM will give the performance of the machine (torque, efficiency) and the values of the costs (weight in kg and cost in euro).

```matlab
function [geo,SOL] = SPM(geo,per)

% SPM DESIGN
% Main data (same for all machines)
geo.mu0 = 4e-7*pi;                              % air permeability [H/m]
geo.Q = geo.q*3*2*geo.p;                        % number of slots
geo.Rri = geo.Ar;                               % rotor inner radius [mm]
rocu = 17.8*(234.5+per.tempcu)/(234.5+20)*1e-9; % resistivity of copper [Ohm*m]
geo.kw = 1;                                     % winding factor
if strcmp(geo.TypeWind,'SingleLayer')
    f = 1;
else
    f = 2;
end
geo.Nc = geo.q*f;                  % conductors in series per pole and per phase
geo.Ns = geo.Nc*geo.p;             % number of turns in series per phase
a = pi*(geo.r)/geo.p;              % pole pitch
Pcu = geo.x*per.loss;

%% Carter coefficient
ssp = (geo.r + geo.g)*pi/(3*geo.p*geo.q);       % stator slot pitch in mm
sso = ssp*geo.acs;                              % stator slot opening in mm
k = (sso/geo.g)/(5 + sso/geo.g);                % First Carter coefficient adim.
be = k*sso;                                     % Second Carter coefficient in mm
kc = ssp/(ssp - be);                            % Carter coefficient adim. (Formula
from "Design of Rotating electric machines")

%% Calculation of Bgap at no load from Boazzo - Pellegrino
kb = 4/pi*sin(geo.km*pi/2);
Bgap = kb*geo.Br/(1 + kc*geo.g/geo.lm);
b = geo.wt*geo.q*2*3*geo.p/(2*pi*(geo.r + geo.g + geo.lt/2) -
geo.wt*geo.q*2*3*geo.p);

% Stator Outer Radius
geo.ly = pi*geo.r*b/(geo.p*pi);
geo.R = geo.r + geo.g + geo.lt + geo.ly;                        % stator outer radius

%% Draw stator
[geo,~] = STATmatr(geo);

% Evaluation of end turn length (Formula from Pellegrino and Bianchi)
[lend] = EndTurnLength(geo);
```

```matlab
geo.lend = lend;                                                      % in [mm]


%% Calculation of Iq
kend = (geo.l + geo.lend)/geo.l;
bkt = geo.wt*3*geo.q/a;
kj = (Pcu)/(2*pi*(geo.R/1000)*(geo.l/1000));
Aq = sqrt(kj*geo.kcu*(1 - bkt)*geo.kw^2*(geo.lt/1000)/(2*rocu*kend));
geo.iq = 2*a*Aq/(3*geo.Nc*geo.kw)*1e-3;


% Draw rotor
geo.phi = geo.km*180;
geo.dx = 1;
[geo,~] = nodes_rotor_SPM(geo);


% Saturation
[Bgap_real,counter] = Saturation(geo,kc,kb);
geo.Bgap = Bgap_real;


%% Calculation of Torque
T = (geo.Bgap*Aq)*2*pi*(geo.r/1000)^2*(geo.l/1000);


%% Inductance evaluations
if rem(geo.q,1) == 0
    Lgpu = pi^2/(6*geo.kw^2)*1/(1/(kc + geo.lm/geo.g))*a/geo.g;
    Lslotpu = pi^2/(2*geo.kw^2)*(geo.lt/geo.g)/(1 - bkt)*(a/geo.g)^-1;
else
    Q0 = (6*geo.p*geo.q)/gcd(6*geo.p*geo.q,2*geo.p);
    Lgpu = 1/f*pi^2/(12*geo.q*geo.kw)*(1/(kc + geo.lm/geo.g))*a/geo.g;
    Lslotpu = pi^2/(2*geo.kw^2)*(geo.lt/geo.g)/(1 - bkt)*(1 - 3*(f -1)/(4*Q0))*(a/geo.g)^-
1;
end
Lpolepu = Lgpu + Lslotpu;
Lbase = geo.mu0*geo.l/2*(2/pi*geo.kw*geo.Nc)^2*1e-3;
b1 = (geo.r + geo.g)*pi/(3*geo.p*geo.q)*geo.acs;
if geo.q > 1
    t = 1 - geo.kracc;
else
    t = 1 - geo.p/geo.Qs;
end
Ltip = 5*((geo.g + geo.lm/geo.mur)/b1)/(5 + 4*(geo.g +
geo.lm/geo.mur)/b1)*3*4/(6*geo.p*geo.q)*geo.mu0*geo.l*(geo.Ns)^2*(1-3/4*t)*1e-3;  % [H]
Juha Pyrhonen 'Design of rotating electrical machines'
Lpole = Lpolepu*Lbase + Ltip;


% Pcu Copper
J = 2*3*geo.Ns*geo.iq/(sqrt(2))/(geo.kcu*geo.Aslot*geo.Q)*1e6;
R = rocu*(geo.l + geo.lend)*geo.q*2*geo.p/(geo.kcu*geo.Aslot)*1e3;
geo.Pcu = rocu*J^2*(geo.kcu*geo.Aslot)*(geo.l + geo.lend)*1e-9*geo.Q;    % Copper losses


%% Calculation of stator iron losses
Stei.Stat.kh = 0.011;                                                % per W/kg
Stei.Stat.ke = 8e-5;                                                 % per W/kg
Stei.Stat.alfa = 1.234;
Stei.Stat.beta = 1.7753;
geo.b = pi*geo.wt/a;
geo.Bfe = Bgap/geo.b;
[Stat_Los] = Calc_StatLosses(geo,geo.Bfe,Stei);           % Losses W/kg for the stator
geo.Pfe_Sta = Stat_Los;                                   % Stator Losses in W


% Volume
Rotor_Volume = (geo.r^2 - geo.Ar^2)*pi*geo.l;
% volume in mm3
Winding_Volume = geo.Aslot*geo.kcu*(geo.l + geo.lend)*geo.q*3*2*geo.p;
% volume in mm3
Stator_Volume = (geo.R^2 - (geo.r + geo.g)^2)*pi*geo.l;
% volume in mm3
```

```matlab
PM_Volume = geo.km*a*geo.l*geo.lm*2*geo.p;
% volume in mm3


% Weigth
PM_Weight = PM_Volume*geo.rho_PM*1e-9;
% weight in kg
Rotor_Weight = Rotor_Volume*geo.rho_Rotor*1e-9;
% weight in kg
Winding_Weight = Winding_Volume*geo.rho_Cu*1e-9;
% weight in kg
Stator_Weight = Stator_Volume*geo.rho_Stator*1e-9;
% weight in kg
Weigth_Tot = Rotor_Weight + Winding_Weight + Stator_Weight;
% total weight in kg


% Power factor
Aq = 3/2*geo.iq*(geo.kw*geo.Nc/a)*1e3;
PF = cos(atan(4*geo.mu0/(3*pi)*Lpolepu*Aq/geo.Bgap));


% Efficiency
Pout = (geo.nmax/60*2*pi)*T;
Plost = geo.Pcu + geo.Pfe_Sta;
eta = Pout/(Pout + Plost);


%% Cost
Cost_PM = PM_Weight*geo.Cost_PM;
Cost_Iron = Rotor_Weight*geo.Cost_Rotor + Stator_Weight*geo.Cost_Stator;
Cost_Cu = Winding_Weight*geo.Cost_Cu;
Cost_Tot = Cost_PM + Cost_Iron + Cost_Cu;


SOL.T = T;
SOL.PF = PF;
SOL.Bgap_sat = Bgap_real;
SOL.Ns = geo.Ns;
SOL.Pcu = geo.Pcu;
SOL.Pfe = geo.Pfe_Sta;
SOL.Weigth_Tot = Weigth_Tot;
SOL.Cost_Tot = Cost_Tot;
SOL.iq = geo.iq;
SOL.L = Lpole;
SOL.Bfe = geo.Bfe;
SOL.eta = eta;
```

When the evaluation of the performance of the machine is finished, the optimization process comes back to the fitness function, which completes its job, giving the penalty factors to the solutions, if they are not satisfying.

```matlab
function [cost,geo] = Optimizationfitness(RQ,geo,per)
[geo] = interpretRQ(RQ,geo);
[geo,SOL] = SPM(geo,per);

%% Costs ==========================================================
cost1 = SOL.Cost_Tot;
cost2 = SOL.Weigth_Tot;
cost  = [cost1 cost2];
%% Weigth for optimization (through PF, Torque) =========
if SOL.eta < per.min_exp_eff && SOL.eta >= 0.4
    pf1 = -99/per.min_exp_eff*SOL.eta + 100;
elseif SOL.eta >= per.min_exp_eff && SOL.eta <= 1
    pf1 = 1;
else
    pf1 = 100;
```

```
    end

if SOL.T < per.min_exp_torque && SOL.T >= 0
    pf2 = -99/per.min_exp_torque*SOL.T + 100;
elseif SOL.T >= per.min_exp_torque
    pf2 = 1;
else
    pf2 = 100;
end
pf = pf1*pf2;
cost(1) = cost(1)*pf;
cost(2) = cost(2)*pf;
```

BIBLIOGRAPHY

[1] A. V. B. B. G. Pellegrino, "Multipolar SPM Machines for direct drive application: a comprehensive design approach," *IEEE International Energy Conference and Exhibition (ENERGYCON),* pp. 98-105, 2012.

[2] B. B. P. G. G. P. Alfredo Vagati, "Design of Ferrite-Assisted Synchronous Reluctance Machines Robust Toward Demagnetizion," *IEEE Transactions on Industry Applications,* vol. 50, no. 3, pp. 1768-1779, 2014.

[3] J. H. &. T. Miller, Design of Brushless Permanent-Magnet Machines, Oxford: Magna Physics Publishing and Clarendon Press, 1994.

[4] N. Bianchi, *Theory and design of fractional slot PM machines,* Padova: Cleup, 2007.

[5] *Tutorial Course Notes - Design, Analysis and Control of Interior PM Synchronous Machines,* Seattle, USA: IEEE Industry Applications Society Annual Meeting, 2004.

[6] *Tutorial Course Notes - Synchronous Reluctance Motors and Drives. A New Alternative,* Denver: IEEE Industry Applications Society, 1994.

[7] G. P. E. A. P. G. B. B. Alfredo Vagati, "Multipolar Ferrite-Assisted Synchronous Reluctance Machines: A General Design Approach," *IEEE Transactions on Industry Electronics,* vol. 62, no. 2, pp. 832-845, 2015.

[8] B. B. P. G. G. P. Alfredo Vagati, "Ferrite Assisted Synchronous Reluctance Machines: A General Approach," *XXth International Conference on Electrical Machines,* pp. 1315-1321, 2012.

[9] G. F. I. M. G. T. A. Vagati, "Design Criteria of High Performance Synchronous Reluctance Motors," *IEEE Industry Applications Society Annual Meeting ,* vol. 1, pp. 66-73, 1992.

[10] W. L. S. G. S. L. N. E. T. M. J. Chun Tang, "Analysis of Stator Iron Losses in Interior PM machines under Open and Short-Circuit Condition," *IEEE Energy Conversion Congress and Exposition,* pp. 1227-1234, 2013.

[11] T. M. J. W. L. S. Seok-Hee Han, "Torque Ripple Reduction in Interior Permanent Magnet Synchronous Machines Using the Principle of Mutual Harmonic Exclusion," *IEEE Industry Applications Annual Meeting,* pp. 558-565, 2007.

[12] P. G. A. V. F. V. Gianmario Pellegrino, "Core Losses and Torque Ripple in IPM Machines: Dedicated Modeling and Design Tradeoff," *IEEE Transactions on Industry Applications ,* vol. 46, no. 6, pp. 2381-2391, 2010.

[13] IEEE, *Trial-Use Guide for Testing Permanent Magnet Machines,* IEEE, 2014.

[14] DIN, *DIN 30910-4: Sintered metal materials - Part 4: Materials for structural parts,* DIN, 2010.

[15] A. G. V. M. F. C. P. Caldori, "Inductance Measurement Methods for Position Estimation in Permanent Magnet Synchronous Motors," *XXII International Conference on Electrical Machines (ICEM),* pp. 1078-1084, 2016.

[16] R. I. B. P. G. G. P. M. P. Eric Armando, "Experimental Identification of the Magnetic Model of Synchronous Machines," *IEEE Transactions on Industry Applications,* vol. 49, no. 5, pp. 2116-2125, 2013.

[17] S.-K. Sul, Control of Electric Machine Drive System, New Jersey: John Wiley and Sons, 2010.

[18] P. Giangrande, *Position Sensorless Control of Linear Permanent Magnet Motor Using High Frequency Injection Strategies,* 2014.

[19] T. R. Liserre, Grid Converters for Photovoltaic and Wind Power Systems, New Jersey: John Wiley and Sons, 2011.

[20] R. Y. Y. W. Y. Y. D. X. Gaolin Wang, "Initial Rotor Position estimation for sensorless interior PMSM with signal injection," *International Power Electronics Conference-ECCE ASIA,* pp. 2748-2752, 2010.

[21] R. D. L. T. M. J. S.-K. S. Yu-seok Jeong, "Initial Rotor Position Estimation of an Interior Permanent Magnet Synchronous Machine using Carrier Frequency Injection Methods," *IEEE Transactions on Industry Applications,* vol. 41, no. 1, pp. 38-45, 2005.

[22] R. T. I. B. G.-D. A. F. B. Marius Fatu, "IF Starting Method with Smooth Transition to EMF Based Motion-Sensorless Vector Control of PM Synchronous Motor/Generator," *IEEE Power Electronics Specialists Conference,* pp. 1481-1487, 2008.

[23] E. A. G. P. S. R. I.R. Bojoi, "Self-Commissioning of inverter nonlinear effects in AC drives," *IEEE International Energy Conference and Exhibition (ENERGYCON),* pp. 213-218, 2012.

[24] T. Instruments, "Sensorless Field Oriented Control of 3-Phase Permanent Magnet Synchronous Motors," Texas Instruments.

[25] T. Instruments, "InstaSPIN Projects and Labs User's Guide".

[26] T. Instruments, "InstaSPIN-FOC and InstaSPIN-MOTION," Texas Instruments.

[27] NXP, "PMSM Electrical Parameters Measurement," NXP.

[28] S.-K. S. Bon-Ho Bae, "A Compensation Method for Time Delay of Full-Digital Synchronous Frame Current Regulator of PWM AC Drives," *IEEE Transactions on Industry Applications,* vol. 39, no. 3, pp. 802-810, 2003.